Master thesis and internship[BR]- Master's thesis : Geometric Adjustment of Complete Dental Prostheses[BR]- Internship

Auteur : Lacanne, Laura
Promoteur(s) : Béchet, Eric
Faculté : Faculté des Sciences appliquées
Diplôme : Master en ingénieur civil en aérospatiale, à finalité spécialisée en "aerospace engineering"
Année académique : 2023-2024
URI/URL : http://hdl.handle.net/2268.2/20374

Master in Aerospace Engineering

University of Liege - School of Engineering

Master's Thesis

Geometric Adjustment of Complete Dental Prostheses

Master's thesis carried out to obtain the degree of Master of Science in Aerospace Engineering by Laura Lacanne

Author:	Laura Lacanne
Advisor:	Pr. Eric Béchet
Committee's members:	Pr. Olivier Bruls
	Pr. Davide Ruffoni
	Nathalie Robert
Submission Date:	June 10th, 2024

Academic year 2023-2024

Acknowledgements

First, I would like to thank my advisor, Professor Béchet, for his advice, his time, his patience and his support during the realisation of this thesis.

I would also like to thank Nathalie Robert for her trust, support, and explanations, as well as her presence, kindness and availability.

I am grateful to my office colleagues: Alex, Cédric, Maxime, and Yassine. They have created a friendly and dynamic work environment.

I would also like to sincerely thank my high school teachers, especially Mr. Nyssen and Mr. Lesoinne, and Mrs. Guyot and Mrs. Brune. I would not have pursued this master's degree without them. They made me grow and they thought me rigour.

I would like to express my gratitude to the administrative, educational, and support personnel of the Faculty of Applied Sciences, especially Denis, and of the CRMT.

I would like to thank my friends, the members of the CdC, especially Mike, Laurent, Axel, Romain, Adrien, Matteo, Léo and Pierre, and of the BdGC for the good moments, the joy and the support.

I would like to thank my brother and sister for their support and their presence.

Additionally, I would like to thank my grandfather for his patience, explanations and passion for my studies. It gave me motivation and strength throughout these five years. I would also like to express my gratitude to my grandmother for always believing in me and loving me. She is my definition of what courage is.

In addition, I would sincerely like to thank Guillaume Bottin, Simon Durieux, Boris Martin and Laura Purpura for the time they took to read this thesis and give me advice.

Finally, I'd especially like to thank my mother. Without her endless love and encouragement, I would not be who I am today. I am forever grateful for the sacrifices she made to raise me.

I dedicate this thesis to the memory of my friend Guillaume Crahay, who left us far too soon, before completing his studies. I would also like to thank his mother for her kindness and express my admiration for her courage.

"I'd rather take coffee than compliments just now."

"I want to do something splendid... something heroic or wonderful that won't be forgotten after I'm dead. I don't know what, but I'm on the watch for it and mean to astonish you all someday."

- Louisa May Alcott, Little Women.

Abstract

This thesis provides an analysis on the impact of misfit in implant-supported fixed dental prosthesis, specifically focusing on the challenges and advancements in managing edentulous patients through these prosthetic solutions. The context highlights the historical issues with traditional removable dentures, which often fail to provide satisfactory outcomes due to discomfort, poor retention, instability, and difficulty in mastication. Implant-supported prostheses have emerged over the past two decades as a reliable solution, offering numerous advantages such as decreased bone resorption, enhanced aesthetics, improved tooth position, and increased occlusion function.

The study emphasizes the criticality of achieving a passive fit between the prosthesis and the implant components to prevent mechanical complications such as screw loosening, framework fractures, and bone damage. Various impression techniques, including plaster impressions, intraoral cameras, and photogrammetry, are evaluated for their accuracy and suitability.

Finite Element Analysis (FEA) is employed to predict the biomechanical behaviour of dental implants under different conditions. This thesis details the process of creating geometric models from 3D scans of prostheses, including post-treatment of the scans and construction of computer-aided models. Mesh accuracy is assessed to ensure reliable simulation results, with discussions on the types of elements used and the convergence of the mesh.

The analysis includes different configurations of prostheses (All-on-8, All-on-6 and All-on-4) and materials (titanium and zirconia). The study identifies the most detrimental directions of misfit and their effects on the stress distribution within the prostheses. It is found that the tangent direction is generally the most detrimental, followed by the normal and binormal directions. Stress concentrations are primarily located in the region between access holes.

Recommendations are made to minimize errors and improve the fit and performance of implant-supported prostheses. This includes optimizing the design and placement of the implants, utilizing advanced impression techniques, and ensuring proper tightening of screws. This thesis concludes with a discussion on the importance of balancing the stiffness of the prosthesis with that of the bone and the implants to prevent adverse effects on bone health and the overall outcomes of the restoration.

Keywords: Implantology, prostheses, Finite Element Analysis, 3D scan, geometric modelling, geometric reverse engineering, stiffness, stress, misfit

Résumé

Ce travail de fin d'étude fournit une analyse de l'impact des défauts d'ajustement dans les prothèses dentaires supportées par des implants, en se concentrant sur les défis et les avancées dans la gestion des patients édentés grâce à ces prothèses. Le contexte met en évidence les problèmes historiques des dentiers amovibles traditionnels, qui échouent souvent à fournir des résultats satisfaisants en raison de l'inconfort, de la mauvaise rétention, de l'instabilité et de la difficulté à mastiquer. Les prothèses sur implants ont émergé au cours des deux dernières décennies comme une solution fiable, offrant de nombreux avantages tels que la diminution de la résorption osseuse, l'amélioration de l'esthétique, la meilleure position des dents et l'augmentation de la fonction occlusale.

L'étude met l'accent sur l'importance d'obtenir un ajustement passif entre la prothèse et les composants de l'implant pour éviter les complications mécaniques telles que le desserrage des vis, les fractures de la prothèse et les dommages osseux. Diverses techniques d'empreinte, y compris les empreintes en plâtre, les caméras intraorales et la photogrammétrie, sont évaluées pour leur précision et leur adéquation.

L'analyse par éléments finis (FEA) est utilisée pour prédire le comportement biomécanique des implants dentaires dans différentes configurations. Ce travail détaille le processus de création des modèles géométriques à partir de scans 3D des prothèses, y compris le post-traitement des scans et la construction de modèles assistés par ordinateur. La précision du maillage est évaluée pour garantir des résultats de simulation fiables, avec des discussions sur les types d'éléments utilisés et la convergence du maillage.

L'analyse inclut différentes configurations de prothèses (All-on-4, All-on-6 et All-on-8) et de matériaux (titane et zirconium). L'étude identifie les directions de défaut les plus préjudiciables et leurs effets sur la distribution des contraintes au sein de la prothèse. Il est constaté que la direction tangentielle est généralement la plus préjudiciable, suivie des directions normale et binormale. Les concentrations de contraintes sont principalement situées dans les régions entre les trous d'accès.

Des recommandations sont faites pour minimiser les erreurs et améliorer l'ajustement et les performances des prothèses sur implants. Cela inclut l'optimisation de la conception et du placement des implants, l'utilisation de techniques d'empreinte avancées et l'assurance du serrage correct des vis. Le document conclut par une discussion sur l'importance de l'équilibre entre la rigidité de la prothèse et celle de l'os et des implants pour prévenir les effets néfastes sur la santé osseuse et le résultat global de la restauration.

Mots-clés: Implantologie, prothèses, analyse par éléments finis, scan 3D, modélisation géométrique, rétro-ingénierie géométrique, rigidité, contrainte, inadaptation.

Contents

List of Figures

1. Introduction

1.1. Context

In recent years, dentistry has seen remarkable advancements, particularly in the field of dental prosthetics. Managing edentulous patients with prostheses has historically posed significant challenges. Traditional approaches, such as complete maxillary and mandibular removable prostheses, often fail in providing satisfactory outcomes. Most of the patients report problems adapting to their mandibular denture. They struggle with discomfort, poor retention, instability, and inability to masticate. Over the past two decades, implant-supported overdentures have been a common treatment for edentulous patients and predictably achieve good clinical results.

Implant-supported dentures offer numerous advantages over conventional complete dentures and removable partial dentures. They decrease bone resorption, minimize prosthesis movement, enhance aesthetics, improve tooth position, improve occlusion, increase occlusal function and maintenance of the occlusal vertical dimension [6].

Figure 1.1 shows a schematic of an implant-supported overdenture. One can observe implants within the bone. They are then screwed into the implants with abutment screws. In Figure 1.2, this pieces positioned in the mouth are shown. The screws are devices that are used to secure the abutment to the implants. They feature threading and are typically tightened until they reach their final seating position, which can be precisely ensured using mechanical or electronic torque measuring devices indicating the torque magnitude applied to the abutment screw. Neglecting proper tightening of the screw can lead to significant challenges and complications, the most prevalent being the undesired rotation of the abutment screw. Improper usage of the abutment screw can also lead to adverse effects on bone health, integrity of implant components, and the overall outcome of the restoration. Finally, the prosthesis is screwed onto the abutments, with prosthetic screws. There may be misfits between the different parts of the system, which may cause problems that will are later discussed.

It is common for implant-supported prostheses to require between 4 and 8 implants to support the structure. The precise number of implants depends on several factors. Firstly, the patient's bone plays a crucial role. The amount of available bone and its density influences the number of implants. If bone loss was experienced, fewer implants are put. It is common to place 8 implants if the patient's oral condition permits. It is preferred to put more implants, because if one is lost, there are more remaining implants. For instance, in an all-on-8 case, there are 7 implants remaining. Moreover, for a maxilla prosthesis, the number of implants also depends on the patient's sinuses, which is a constraint that must be considered. This information is determined through CBCT scan. It is also common to consider if the patient already has implants in the mandible. If there are 4 implants on the lower jaw, it may not be appropriate to place 8 implants on the upper jaw. Finally, their placement and distribution must also ensure proper load distribution to avoid overloading any single piece, which may lead to failure. The sinuses are shown in Figure 1.3. It is evident that they are close to the maxillary bone, and must be considered when placing the prosthesis.

Figure 1.1.: Schematic of an implant-supported overdenture.

Figure 1.2.: Abutments placed into the maxillary.

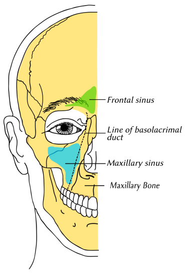

Figure 1.3.: Schematic of the sinuses of the face [1].

The process of placing an implant-supported prosthesis involves several steps.

Firstly, 4 to 8 implants are placed into the bone. Then, immediately after, abutments are placed. They allow the gum to heal, and they subsequently serve as protective halos. These pieces are placed on the same day of the implants to allow the gingiva to heal properly by creating a gingival attachment on this implant abutment, that acts as a protective barrier. This also allows the implant to remain in more sterile conditions. Right after the surgery, the dental impression is done around the abutments. An explanation on the existing impression techniques is given in Section 1.1.1. Once the impression is done, a virtual model is created and used to design the framework. It is then milled either in titanium or zirconia. There are also 3D printing techniques available, but they are much less precise than milling. Therefore, they are only used for temporary resin prostheses.
As said earlier, there are two materials for prostheses: titanium or zirconia. In Figure 1.4, the two types of prosthesis are shown. The choice of material depends on the patient's aesthetic preferences and whether there are remaining natural teeth.

1.1.1. Different Types of Dental Impressions

At the CHU of Liège, dentists work with three types of dental impressions. First, the impression with plaster is discussed. Then, the use of intraoral cameras is analysed. Finally, a discussion on photogrammetry is introduced.

Impression with Plaster

This is the only option that is validated in dentistry. The impression is taken around the abutments. Impression transfers are gently screwed onto the abutments. These tools are used to capture the positions and axes of the abutments. They come with the impression tray. An analogue is then

(a) Titanium.

(b) Zirconia.

Figure 1.4.: Different materials for the prostheses.

positioned and attached to the transfer left inside the impression. This is an exact replica of the implant's connector in the mouth [7]. The whole assembly is then scanned by a lab scanner, and a virtual model is generated. The framework is then designed based on this model. The issue with this method is that many human errors are possible.
The impression transfers can be seen in Figure 1.5c and in Figures 1.5a and 1.5b, the analogues placed on the impression are shown.

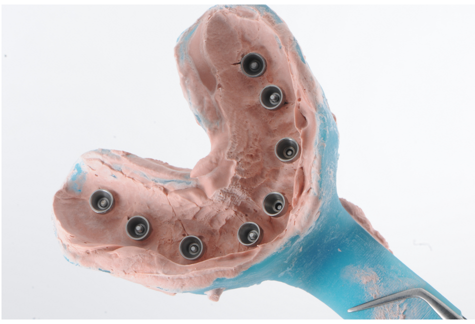

(a) Bottom view of the negative with the analogues.

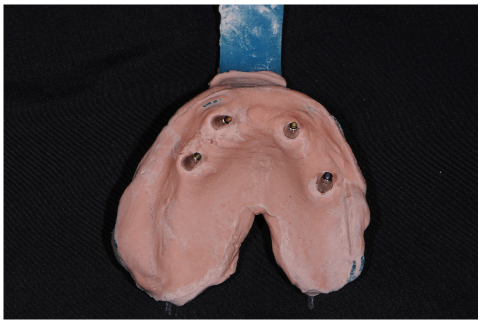

(b) Top view of the negative with the analogues.

(c) Impression transfers on abutments.

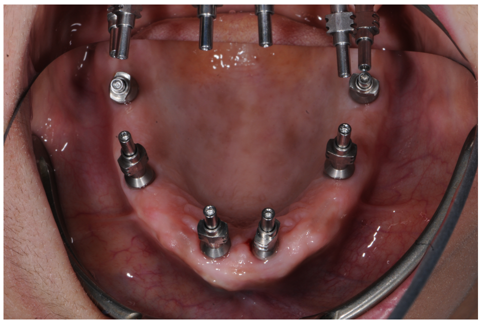

(d) Impression transfers on abutments. Other view.

Figure 1.5.: Impression with plaster.

Use of Intraoral Cameras

This type of impression relies on the use of an intraoral scanner that can be seen in Figure 1.6a. It involves a reconstruction system with point acquisition. The point cloud is then transformed into a mesh, resulting in an STL or PLY file. The main problem with this type of impression is that the

measurements are distorted due to the lack of teeth and, therefore, reference points. Currently, the software associated with this type of impression is not able to reconstruct the patient's mouth accurately. The deviations related to the measurements are more random than with plaster. Therefore, when used alone, this type of impression is not a reliable method employed in dentistry. Furthermore, since the camera lacks reference points, there is an accumulation of errors.
This method requires the use of scan bodies. They are small devices placed onto the abutments. The scanner scans their as well as the surrounding oral structures. The position and the orientation of the dental implants are given by these small pieces, that can be seen in Figure 1.6b.

(a) Picture of an intraoral scanner.

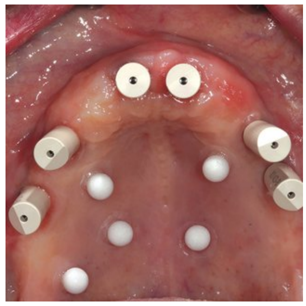

(b) Picture of scan bodies fixed to the abutments in a patient's mouth.

Figure 1.6.: Intraoral system.

Use of Photogrammetry

The last type of impression involves the use of photogrammetry. This method requires using a hand held "camera unit" consisting of four cameras and one projector. This technology combines photogrammetric and structured light scanning techniques to capture 3D data. The position and orientation of implants is known because scan bodies are then again placed on the abutments. Once the measurements are done, a software does a reconstruction by triangulation. The output is an XML file with the direction and positions of the implants.
The camera used for this technique at the CHU of Liège is the *ICam4D*. It is shown in Figure 1.7a. This device comes with a calibration plate, and must be calibrated before each measurement. The small white points on the *ICamBodies*, the scan bodies, are used for increasing the number of reference points. These tools are shown in Figure 1.7b. This technology comes along with a software that can detect if some scan bodies are too close to each other, and it automatically removes them [8]. Since the output of this system is only an XML file with only the positions and the orientations of the abutments, it must be combined with an STL file of the gingiva in order to reconstruct a digital model.
Thus, this must be used in combination with a plaster impression or an intraoral scanner.

Dental implant surgeries are subject to varying degrees of human error. In this study, the impact of misfit between the prosthesis and the transgingival abutment will be analysed. Three misfits will be tested: 50, 100, and 150 microns in every direction in space. It will then be possible to determine in which direction this misfit is most detrimental.

(a) Picture of the *ICam4D* camera.

(b) Picture of the *ICamBodies*.

Figure 1.7.: Photogrammetric system.

1.2. Motivation

Determining the acceptable misfit for an implant-supported prosthesis is essential. It is imperative to ascertain the degree of error that can be tolerated before it becomes problematic for the patient. While the fracture of a prosthesis, abutment, screw or implant is inconvenient, it is manageable. However, the considerable concern arises if the misfit leads to the fracture of one or more implants and subsequent bone damage. Damaging the bone renders the affected site unsuitable for future implantation, posing significant limitations for the patient. As is later studied in this thesis, human errors may occur at every stage of the process, ranging from impression-taking to prosthetic placement. Hence, it is crucial to establish the permissible misfit without adverse effects on the prosthesis, implants and bones. Moreover, minimizing human error is imperative, necessitating a comprehensive examination of various impression and scanning techniques. Identifying the sources of error enables corrective measures and the development of new methodologies. By pinpointing the origins of inaccuracies, adjustments can be made to mitigate potential issues and enhance overall procedural efficacy. Additionally, the exploration of alternative methods becomes feasible, facilitating the discovery of innovative approaches to minimize error and optimize outcomes.

1.3. Goal and Structure of this Thesis

The main work of this thesis is the study of the influence of misfitting titanium or zirconia framework on the implants. A key aspect of this investigation involves identifying the most detrimental direction of misfit. Three types of prostheses are analysed: All-On-8, All-On-6 and All-On-4.

Within this thesis, some technical concepts are simplified to reach a broader audience. This approach aims to enhance comprehension while upholding scientific rigour and accuracy. By making these elements more accessible, the goal is to facilitate the dissemination of knowledge, ultimately enriching professional practices and promoting advancements in the field.

In the second chapter of this thesis, a literature review is presented. It begins by examining the effect of the number of implants, followed by an exploration of the impact of misfit on the system. Then, the bone structure is detailed. Afterwards, the impacts of a dynamic loading and bone material properties are explained. Impression errors are also assessed. In a sixth section, explanations on Finite Element Analysis (FEA) are given. Geometric Reverse Engineering is then developed. Finally, a brief explanation of Continuity is given.

In the following chapter, the procedure for creating geometric models of prostheses is outlined, starting from a 3D scan of the framework. Firstly, an explanation on why and how to conduct the scan-to-CAD process is provided. Next, the post-processing of the 3D scan is described. Following this, the construction of the computer-aided model is reviewed. Finally, the three different prostheses are analysed in this thesis.

The fourth chapter describes the Finite Element Analysis of the overdentures. It begins with a mesh accuracy assessment with a focus on the element type, the mesh generation and a convergence analysis. Then, the two materials used for implant-supported overdentures are reviewed. Afterwards, the different load cases are developed. Finally, a static linear analysis is conducted for the two materials in every possible configuration. The impact of the number of implants is also studied. The stiffness of the different components of the system are determined. Thanks to this, the total displacement tolerable is found for every configuration.

Finally, some perspectives are discussed, and this thesis is concluded.

2. Literature Review

In a preliminary step, it is important to synthesize all the information useful and necessary for the analysis of the deformation of a complete dental prosthesis when a misfit is applied between the screw and the prosthesis.

Achieving precision in the fit between implant-supported prostheses and their components has been a central focus in modern prosthodontics. As developed below, various studies have delved into the biomechanics of internal connections, emphasizing the criticality of achieving a passive fit to mitigate undue stress on the implant system and surrounding tissues. To comprehensively understand and predict the behaviour of these systems under various conditions, Finite Element Analysis (FEA) has emerged as a powerful tool. This chapter reviews the literature on the biomechanics of dental prostheses, particularly focusing on the impact of misfits, and explains how Finite Element Analysis is employed to simulate and analyse the effects of a misfit.

2.1. Impact of the Number of Implants

One notable investigation evaluated the impact of reducing the number of implants on prosthesis outcomes [9]. While the traditional six-implant option has historically been reliable, recent clinical studies [10, 11] have highlighted the viability of using four implants. This approach not only boasts a high cumulative survival rate but also offers advantages in terms of cost-effectiveness, reduced invasiveness, and shorter treatment intervals. However, concerns linger regarding prosthetic survival rates, with some studies[12, 13, 14] reporting technical complications such as prosthetic fractures, abutment loosening, prosthetic screw loosening and factors that lead to prosthesis overloading, possibly stemming from reduced implant numbers.

2.2. Influence of a Misfit on the System

To prevent technical complications in screw-retained constructions, it was stated that achieving a passive fit between components is essential [15]. A perfect fit entails simultaneous contact of all fitting surfaces with no strain before load application, although this ideal condition is challenging, and nearly impossible, to reproduce clinically. Misfits between components are inevitable during prosthetic procedures, from impression to construction delivery. Various techniques including computer-aided design/computer-aided manufacturing (CAD/CAM) technology have been proposed [16, 17, 18] to minimize inaccuracies in framework production.
Inadequate fit leads to uneven stresses and strains at the interface between the framework and implant, contributing to mechanical complications such as screw/abutment loosening or fractures, framework fracture, and, in severe cases, implant fracture or loss. The impact of a misfit up to 200 microns on the system remains unclear. Some authors deem it clinical unacceptable [2], while others suggest that misfit exceeding 200 microns have minimal influence on clinical outcomes [19, 20].

A compromised fit between the contact surfaces of screw-retained implant-support fixed dentures (IFDs) is known to induce uncontrolled strains in the components and peri-implant tissues, leading to biological and technical complications such as bone loss, screw loosening, and component fractures, with the worst-case scenario being the loss of implants, the prosthesis, or both [2]. In full-arch reconstructions, screw fracture and chipping or fracture of the veneering material are the most common technical complications. Early opinion leaders in osseointegrated oral implants [21, 22] suggested that marginal discrepancies of 10 to 150 $[\mu m]$ would be clinically acceptable in the long term, while from a biological standpoint, gap sizes should be smaller than those permitting harmful bacteria (less than 2 $[\mu m]$).

Before the commercial availability of CAD/CAM technology, the lost-wax technique for metal alloy frameworks was considered the gold standard. The accuracy of the conventional workflow, presented in Figure 2.1, depended largely on physical material properties (impression, master model, casting) and human-related factors (timing, manual handling), making it susceptible to unpredictable distortion. Digital workflows, on the other hand, are less influenced by manual errors and involve fewer steps, though minor imprecisions may arise during scanning, transfer, and milling. Casting, however, is known for its technique sensitivity and physical distortion, particularly evident in longer-span IFDs, which may result in poor prosthesis fit. Therefore, short-span IFDs were often preferred. Perfect passive fit occurs when opposing surfaces of implants and framework intaglio exhibit maximal spatial congruency, without inducing strains in the components after tightening all screws, provided that implant and framework surfaces are perfectly planar. A misfit classification was proposed against the background of the fabrication feasibility based on various studies [23, 24, 25], which is summarized in Table 2.1.

Fit/misfit	**Before screw tightening: Gap size at the interface (vertical and horizontal)**	**During screw tightening or loosening: Rotation (°) to final load (+ screw torque monitoring)**	**After screw tightening: Strains in the pontic**	**Fabrication feasibility and clinical acceptance**
Perfect	0 µm	Small final rotation (Screw torque initial: low, final: steep increase)	0 µm/m	Theoretical
(Very good)	< 25 µm	$< 45°$ final rot.	< 25 µm/m	3-unit IFD
Good	< 50 µm	$< 45°$ final rot.	< 50 µm/m	4-9-unit IFD
Fair	50–100 µm	$< 45°$ final rot.	50–100 µm/m	Complete IFD
Moderate	100–150 µm	$< 90°$ final rot.	100–150 µm/m	Not acceptable
Poor	> 150 µm	$< 90°$ final rot.	> 150 µm/m	Not acceptable
(Very poor)	> 200 µm	Great final rotation (Screw torque initial to final: constantly high and increasing)	> 200 µm/m	Not acceptable

Table 2.1.: Proposed fit and misfit classification according to reported assessment techniques [2].

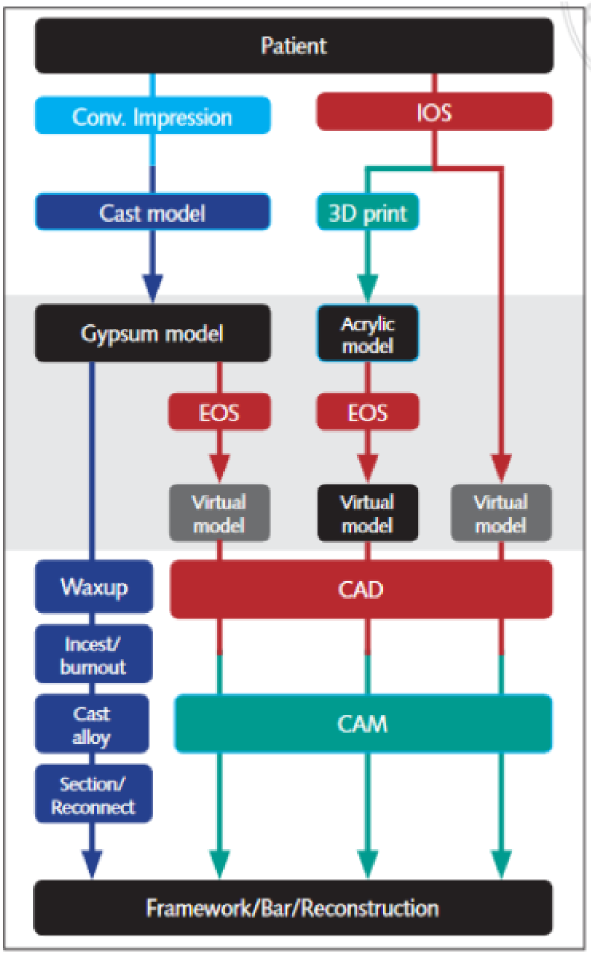

Figure 2.1.: Conventional and digital workflows for the fabrication of the working model (grey box) and the final implant reconstruction. Each box corresponds to a working step (blue: manual, red: digital, green: CNC machine) with potential dimensional errors. (EOS: Extra-oral scanner (laboratory scanner); IOS: Intra-oral scanner) [2].

The absence of passive fit within the prosthesis-implant-retaining screw system is a crucial aspect explored in research [26]. Achieving passivity is imperative to avoid generating inappropriate stress that could compromise the stability of the superstructure, implant components, and surrounding bone. The presence of a misfit between prostheses and implants during the screw preload process, attributable to the differing stiffness characteristic of typical prostheses and retaining screws, may give rise to asymmetric contact patterns among the various components within the system. In many instances, this misfit remains undetectable through visual inspection. Studies [27, 28, 29, 30, 31, 32, 33, 34] have highlighted the challenges in achieving true passive fit due to inherent discrepancies in material stiffness and fabrication techniques. Long term misfit can lead to mechanical issues such as loosening and failure of the abutment screw, defects and mobility of the superstructure, failure, or loss of the implant osseointegration, highlighting the importance of meticulous fit assessment and adjustment.
Despite the substantial strains and stresses induced in the bone due to misfit, there appears to be a notable biological tolerance to this static force.

It was also stated that true passivity is impossible to attain [35]. Distortions in the framework can occur at any stage from impression making, investing, casting of the framework, to the delivery of the prosthesis. Many studies suggest a correlation between the different complications stated before and after prosthesis fit, although the precise relationship remains poorly understood. In a 5-year follow-up study [32], it was observed that a significant number of patients experienced partially unstable or loose screws and prothesis misfit, yet without major clinical consequences.

In the pursuit of optimal fit, advancements in manufacturing methods have been scrutinized [36]. This comparative study has assessed the accuracy of frameworks fabricated using conventional lost-wax casting against those produced through CAD/CAM techniques. While CAD/CAM offers promising results, concerns persists regarding misfit, with implications for stress distribution within the prosthesis and surrounding structures. Notably, the choice of framework material, whether titanium or zirconia, influences stress patterns, with zirconia frameworks exhibiting higher stress levels under misfit conditions.

Furthermore, the influence of vertical misfit on strain within screw-retained implant framework has been studied [37]. Studies [38, 39] have highlighted the mechanical consequences of poor fit, emphasizing the importance of minimizing misfit to mitigate strain-induced complications. Both titanium and zirconia frameworks are susceptible to deformation under misfit conditions, albeit with varying degrees of stress generation.

In clinical practice, assessing fit at the implant-prosthodontics interface remains paramount [40]. Various measurement techniques, from stylus-based methods to photogrammetry, offer insights into the precision of fit in three-dimensional space. However, achieving a perfect fit remains elusive, with studies [30, 41, 42, 43] acknowledging the inevitability of minor discrepancies and advocating for a combination of assessment methods to ensure comprehensive evaluation.

2.3. Bone structure

The bone structure of the skull is illustrated in Figure 2.2. The bones that are in contact with the prostheses are the maxilla and the mandible.
Applying force to a bone structure creates stress, potentially causing its structural arrangement to deform, a phenomenon otherwise called strain. It is important to note that alterations in bone mass, resorption, or remodelling are more closely linked to strain rather than to stress alone. According to

some authors [44, 45], bone cells react to localized deformation caused by mechanical stress. This continuous process is crucial for preserving the mechanical strength of bones, including those surrounding dental implants [9].

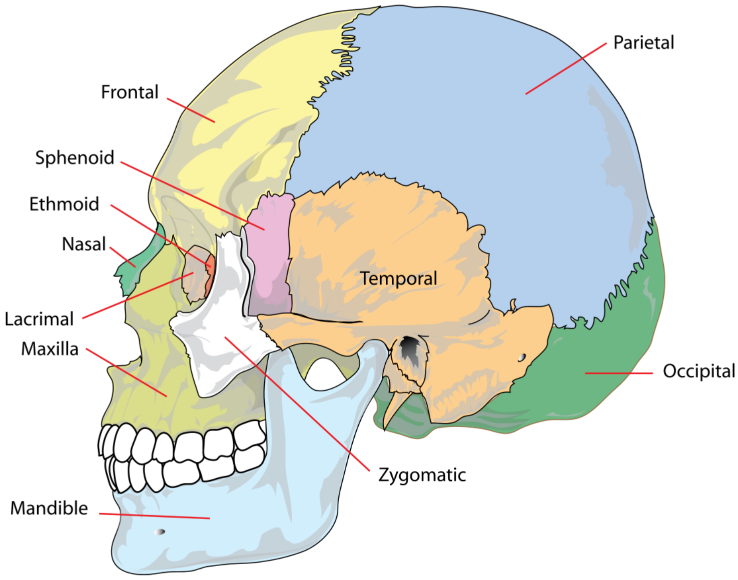

Figure 2.2.: Bone structure of the skull.

One interesting thing to know is the stiffness of the mandible and maxilla. Unfortunately, there is a lack of information concerning these values. However, the dimensions of those bones are given in [46].

2.4. Dynamic Loading and Bone Material Properties

The success rate of dental implants significantly depends on efficient stress transfer from the implant to the supporting bone, influenced by loading conditions, implant thread design, and bone material properties [47]. Most studies [48, 49, 50, 51, 52, 53, 54, 55, 56] simplify bone as isotropic, homogeneous, and linearly elastic, despite its inhomogeneous and anisotropic characteristics, leading to lower stress predictions than observed in practice. The simplification reduces the clinical applicability of simulation results.

Dynamic loading, compared to static loading, increases stresses by 30 to 60 %, significantly impacting stress distribution. Dynamic loading can damage dental implants' surface morphology and chemistry, allowing microorganism penetration and increasing cyclic stress by 10 to 20 %. The stress induced in the implant and surrounding bone varies with the applied load type and implant thread design.

When testing models with different implant thread shapes, it was shown that stress increases significantly under dynamic loading, emphasizing the need to monitor cyclic loading rates to prevent implant and bone fatigue and fracture [47].

Bone material properties, particularly anisotropy, significantly affect biomechanical behaviour. Anisotropic modelling shows increased stress and strain levels, better reflecting clinical conditions [47].

2.5. Accuracy of Impressions

In a study aiming to compare the accuracy of two digital impression techniques, Intraoral Optical Scanning (IOS) and Stereophotogrammetry (SPG), for complete-arch dental implants [57], it is stated that the mean Euclidean distance for the IOS is 137.2 [μm], and 87.6 [μm] for the SPG. For the plaster impression [58], it is found that the deviation is 24.6 ± 17.7 [μm]. It is the most accurate impression technique, but is very uncomfortable for the patient.

2.6. Finite Element Analysis

Finite Element Analysis is the process of predicting an object's behaviour based on calculations made with the Finite Element Method (FEM). FEM is used to break complex systems into smaller elements, and then applies differential equations to each element individually [59]. It is used to predict how a structure responds to external forces, deformation, heat, and other physical effects.
To do so, the structure is divided into a finite number of elements. Each element connects at points called nodes, forming a mesh. Then, mathematical equations representing physics laws are applied to each element. Finally, the system of equations is solved to find approximations of the unknowns at the node.
Finite Element Analysis (FEA) is used in dentistry, and more specifically in implantology and prosthodontics. It is used to predict the biomechanical behaviour of various dental implant designs, as well as the effect of clinical factors for predicting the clinical success. Thanks to FEA, the stress patterns in implant components and surrounding bone are studied. FEA gives an in-depth idea about the patterns of stress in the implant and in the peri-implant bone. This helps in betterment of the implant design and insertion techniques [60].
As mentioned above, ensuring a proper fit is crucial for patient comfort and functionality. FEA can be used to simulate misfits and their impacts. It can also be used to predict the behaviour of the different materials used in dental prostheses under operational conditions.
There are different steps to follow in order to conduct a Finite Element Analysis. The first step is the modelling of the object that one wants to analyse. The sophisticated geometrical features should be omitted and the basic structure of the object should be represented. After that, the material is defined. In the case of a prosthesis, it is either titanium or zirconia. Then, the geometry of the structure is divided into smaller shapes, the finite elements. This step is called meshing. Finally, the loads and boundary conditions have to be applied.
One important aspect is the quality of the mesh. The more regular the shape is, the easier it is to solve the system of equations.

2.7. Geometric Reverse Engineering

One precious tool used for this thesis is Reverse Engineering (RE). In mechanical engineering, geometric reverse engineering can be defined as the redesign of an existing product based on various information such as its geometrical shape, involved manufacturing processes and assemblies, functionality or documentation [61]. In other words, the redesign involves reconstructing a Computer-Aided Design (CAD) model from the product, aiming to be as close as possible to the original design of the object [62]. RE seeks to infer a model and its parameters from experimental data. The geometric RE process is divided into four basic steps, as shown in Figure 2.3. The first step, the data capture, consists in scanning the body to convert its geometry into a numerical form. The preprocessing step prepares the raw data for the next steps by cleaning the model from some specific defects. The segmentation and surface fitting step is the most critical one because it requires a great deal of reflection. Finally, the CAD model is generated by connecting surfaces and applying properties.

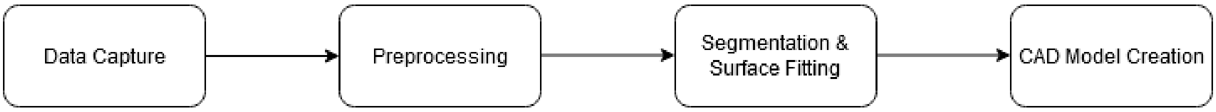

Figure 2.3.: Geometric Reverse Engineering Steps [3].

2.8. Continuity

The continuity of a surface or a curve refers to its smoothness and quality of shape. The continuity is determined by the degree of matching between the position, direction, curvature and curvature change rate of the adjacent segments or surfaces.

2.8.1. Curve Continuity

There exists four levels of curve continuity: G0, G1, G2 and, G3, where G stands for "Geometry". G0 corresponds to the case where the two curves are connected, but only their positions match at the connection point. For G1, the two curves are connected, and their positions and directions match at the connection point. In the third case, G2, the two curves are connected, and their positions, directions and curvatures match at the connection point. The last case is the same as the third one, with a matching curvature change rate [5]. The different curve continuities are illustrated in Figure 2.4.

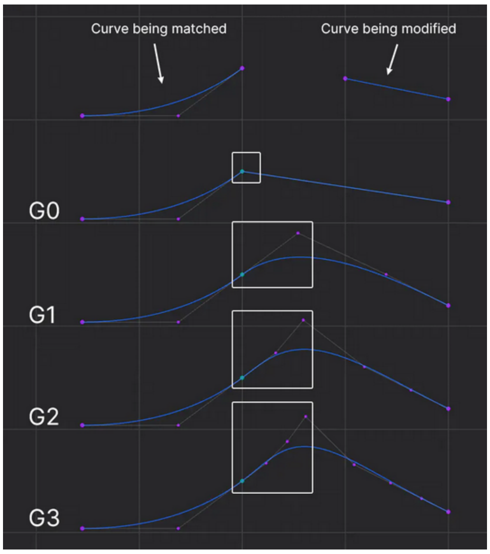

Figure 2.4.: Different cases of curve continuity [4].

2.8.2. Surface Continuity

For the matching of surface, there exist three types of continuity: G0, G1 and G2. G0 corresponds to the case where the two surfaces are connected, but only their positions match at the connection point. For the G1 case, the two surfaces are connected, and their positions and tangents match at the connection. The G2 is the same as the G1, but with the curvature matching too [5]. The different surface continuities are shown in Figure 2.5.

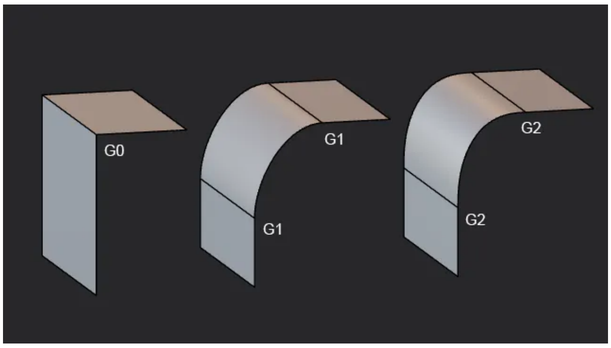

Figure 2.5.: Different cases of surface continuity [5].

3. Geometrical Modelling

Since the Computer-Aided model (CAM) of the prostheses is unavailable, it is necessary to seek an alternative method for generating a numerical model.
To do so, a scan of an All-on-8 prosthesis is performed and saved in STL format. With such files, a Reverse Engineering modelling, also called a scan-to-CAD model, is possible. It is then possible to recover a numerical model suitable for stress analysis.

This chapter outlines the steps taken to create the numerical model based on the 3D scan of the denture [63][61].

3.1. Why and How to Conduct the Scan-to-CAD Process

A scan-to-CAD model is used because the studied prostheses are not available in files compatible with a simulation software. This is much more convenient than having to recreate the model from scratch, since the geometries of the prostheses are intricate. However, as is later explained in Section 4.1.3, there is a slight deviation observed when comparing the Computer Aided model and the 3D scan.

Siemens NX1859 software is used to generate a numerical model and to analyse it. A post-treatment of the 3D scan is necessary. Then, the CAD model is constructed.

3.2. Post-Treatment of the 3D Scan

It is important to clean the 3D scan since it is susceptible to various flaws that mainly come from accessibility and occlusion issues, which require correction. The main problems in the denture scans were holes and defective facets. During this step of the methodology, various irrelevant details were also removed from the digital model.

It is necessary to undergo this cleaning process before proceeding with the reconstruction of the prosthesis. If this step is not correctly executed, its repercussions directly affect the utilization of the geometric reconstruction tools in *Siemens NX1859*.

The different views of the 3D scan can be seen in Figures 3.1 and 3.2.

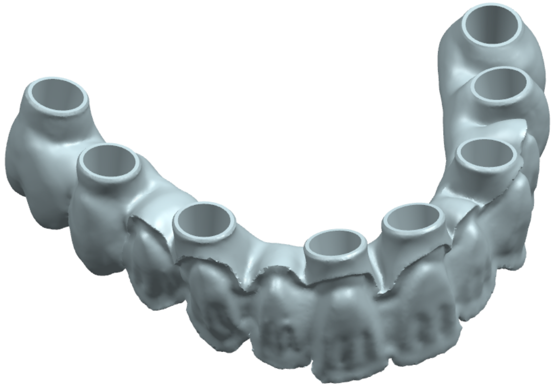

Figure 3.1.: Isometric view of the 3D scan.

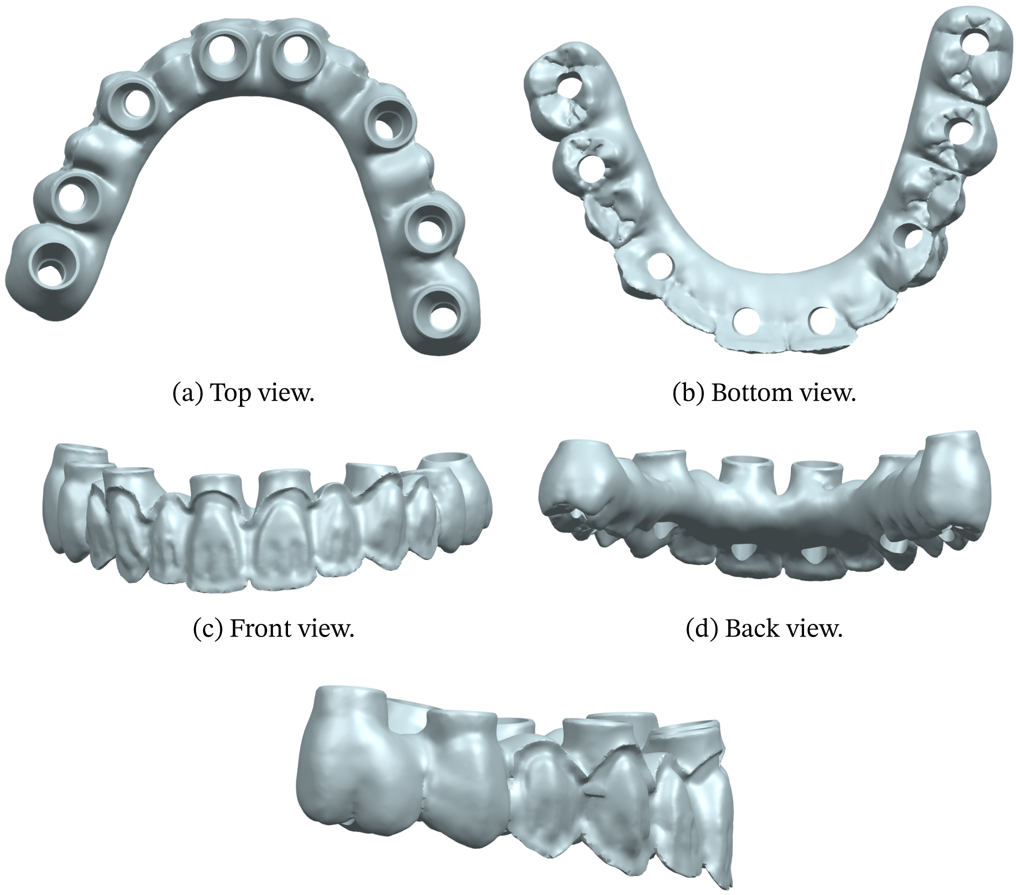

(a) Top view.

(b) Bottom view.

(c) Front view.

(d) Back view.

(e) Left view.

Figure 3.2.: Different views of the 3D scan.

3.2.1. Methodology

This section aims to highlight the various flaws present in the 3D scan, as well as the different methods to eliminate them. It involves the use of tools defined within *Siemens NX1859*.

In order to relieve the strain on the computer's operating system and to work on smaller areas, it is important to divide the overdenture into multiple elements.

Paint Facet Body

This tool is located in the *Reverse Engineering* section of the software. Is it used to delineate the distinct regions of the model. Figure 3.3 shows the use of the *Paint Facet Body* tool.

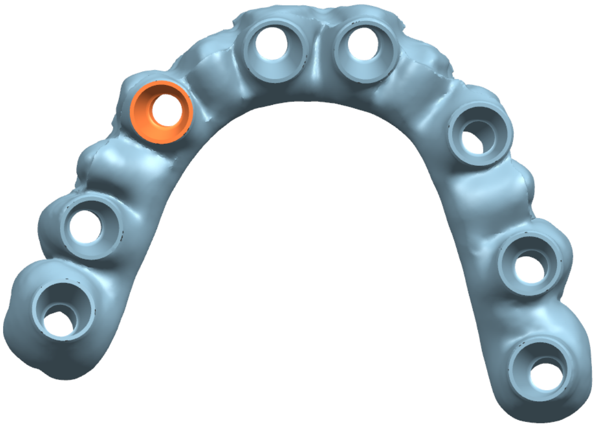

Figure 3.3.: Use of the *Paint Facet Body* tool.

Divide Facet Face

This tool is located in the *Reverse Engineering* section too. It is used to refine the topology of a convergent facet body by dividing its face into multiple faces [64]. The *Color Region* option of the dialogue box is selected. The use of this tool is shown in Figure 3.4.

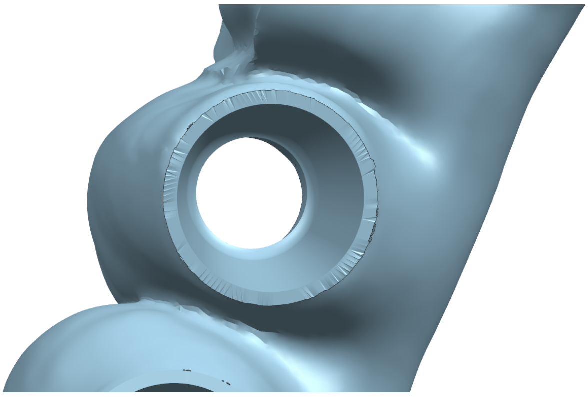

Figure 3.4.: Use of the *Divide Facet Face* tool.

Extract Geometry

This tool is part of the *Surface* section. It is used to create a body by extracting it from existing objects [65]. It allows working with smaller areas. An example of region is presented in Figure 3.5.

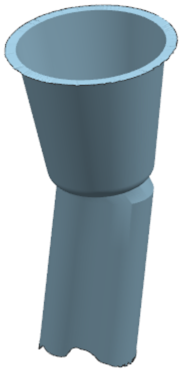

Figure 3.5.: Use of the *Extract Geometry* feature.

Remesh Facet Body

Now that the denture is divided into smaller regions, it is interesting to remesh the different areas. The tool used is *Remesh Facet Body*. It allows working with a smaller and more uniform mesh in some regions in order to increase the precision. As explained in [63], it is possible to select the size of the new mesh. The objective of this operation is to generate a mesh with the maximum desired facet size as a parameter. Figure 3.6 shows the effect of a remesh.

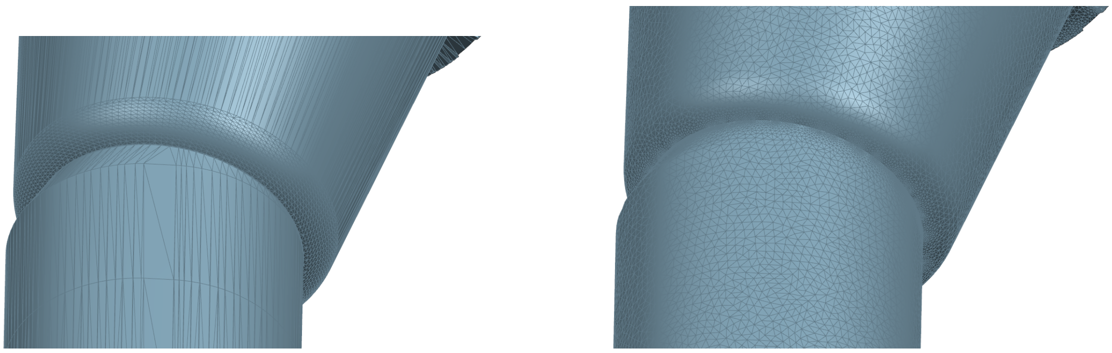

(a) Before the remesh

(b) After the remesh

Figure 3.6.: Effect of a remesh.

3.3. Construction of a Computer-Aided Model

Once the 3D scan is cleaned, it is possible to reconstruct the complete dental prosthesis. This part describes the methodology used to achieve this reconstruction.

The surfaces of the previously defined areas have to be created. There are two options available in *Siemens NX1859*, that are briefly presented.

3.3.1. Rapid Surfacing

This tool is located in the *Reverse Engineering* section. It is the most powerful tool available in the software. This feature reverse engineers a facet body with surface geometry quickly. It may not assure a perfect accuracy, since speed is more important than surface quality. The desired degrees and number of segments must be specified, and the software creates a curve network on the facet body. The curve network is then used to generate a G1 continuous surface model of the facet body. For the denture, this tool is found to be well suited and works in most of the cases. Figure 3.7 shows the use of this feature.

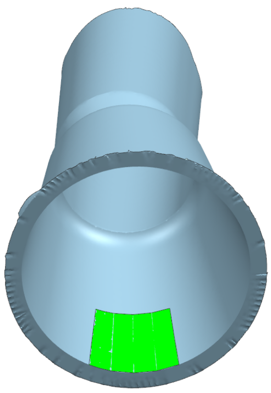

Figure 3.7.: Illustration of the use of *Rapid Surfacing*.

3.3.2. Fill Surface

When it is not possible to use the *Rapid Surfacing* tool, the *Fill Surface* feature is chosen. It is found in the *Surface* section. This feature is used in conjunction with the *Fit Curve* found in the *Reverse Engineering* section. These are mainly used at the extremities of the different zones and when approximating a surface near a hole in the part. In Figure 3.8a, the use of *Fit curves* is illustrated and in Figure 3.8b, *Fill Surface* is applied.

(a) Use of *Fit Curve*

(b) Use of *Fill Surface*.

Figure 3.8.: Recreation of a surface at the extremity of the area.

3.3.3. Swept

Additionally to the above feature, *Swept* is also used in conjunction with *Fit Curve* set to *Circle* when wanting to represent the ring shapes of the denture. This is illustrated in Figure 3.9.

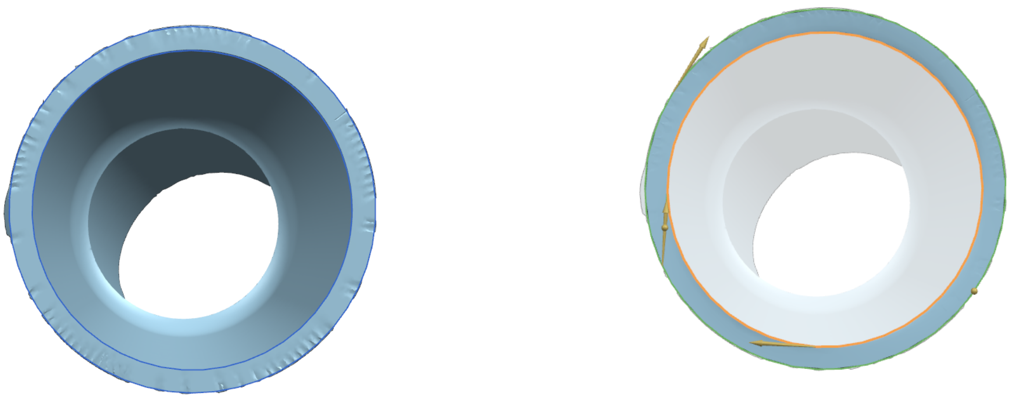

(a) Use of *Fit Curve* set to *Circle*. (b) Use of *Swept*.

Figure 3.9.: Recreation of a ring-shaped surface.

3.3.4. Accuracy Verification

It is important to note that working on small areas of each piece is necessary to reduce operation time, lighten the system load and be more precise.
To verify the accuracy of the surface created, the *Deviation Gauge* tool can be used. This feature displays the deviation between the target object, the reconstructed overdenture, and the reference object, the 3D scan [66].
The accuracy of the denture can be seen in Figure 3.10. The deviation may appear significant in certain areas, but this is due to the impossibility of representing certain irregularities of the denture, thus necessitating a smoothing process.

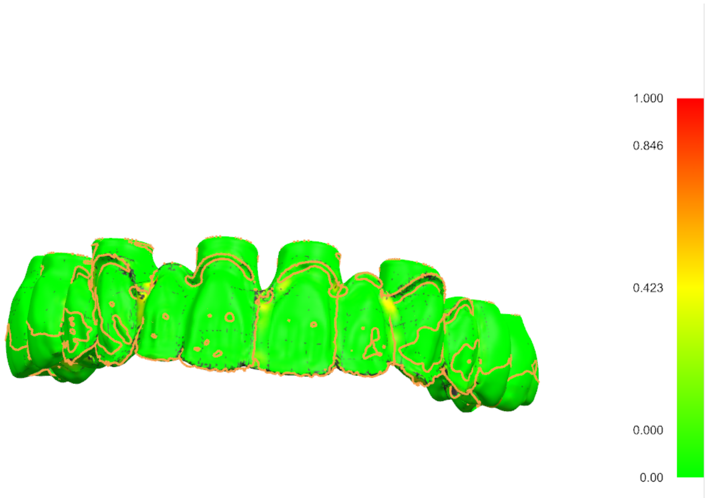

Figure 3.10.: Deviation analysis.

Once the different surfaces are created, it is necessary to connect them all. This is either done by the *Combine* or the *Sew* feature. If the sheet surfaces intersect each other, the *Combine* tool trims and joins them. If the two surfaces are distinct, the *Sew* is chosen. This tool takes a tolerance as input. If the two surfaces are disjointed by a gap smaller than this tolerance, the software joins them. It is possible to verify that the two surfaces are united by using the *Examine Geometry* feature in the *Surface* section. The sheet boundaries are highlighted in red. It is thus easy to see the gaps between surfaces. If there is a gap in the piece, it is necessary either to switch from the *Combine* tool to the *Sew* tool, or adjust the tolerance if the *Sew* tool is already selected. The use of *Examine Geometry* can be seen in Figure 3.11.

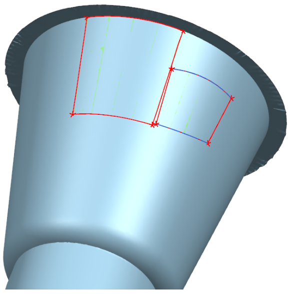

Figure 3.11.: Illustration of *Examine Geometry*.

If all the surfaces are correctly joined, a solid body is generated and can thus be used for the Finite Element Analysis.

3.4. Different Types of Prostheses

As introduced earlier, three types of prostheses are analysed. The first prosthesis analysed is on eight implants. The second type is on six implants and the last one is on four.

The provided scan is for a full prosthesis on eight implants. The model is obtained for the All-on-8 as explained in the above sections. For the two other models, it is necessary to start from the scan of eight implants, fill in the required number of implants, and then proceed with smoothing. The reconstruction of an All-on-8 prosthesis is illustrated in Figure 3.12. The different views are visible in Figure 3.13. The right view is absent since the prosthesis is symmetric.

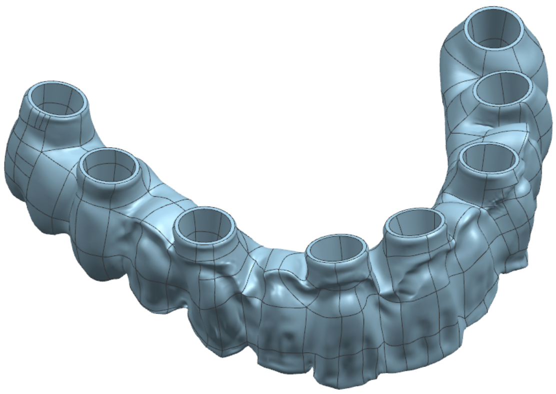

Figure 3.12.: Isometric view of the All-on-8 CAD Model.

As discussed earlier, the All-on-6 is simply an All-on-8 where two implants were filled and smoothed. The isometric view can be seen in Figure 3.14a. The All-on-4 model can be seen in Figure 3.14b.

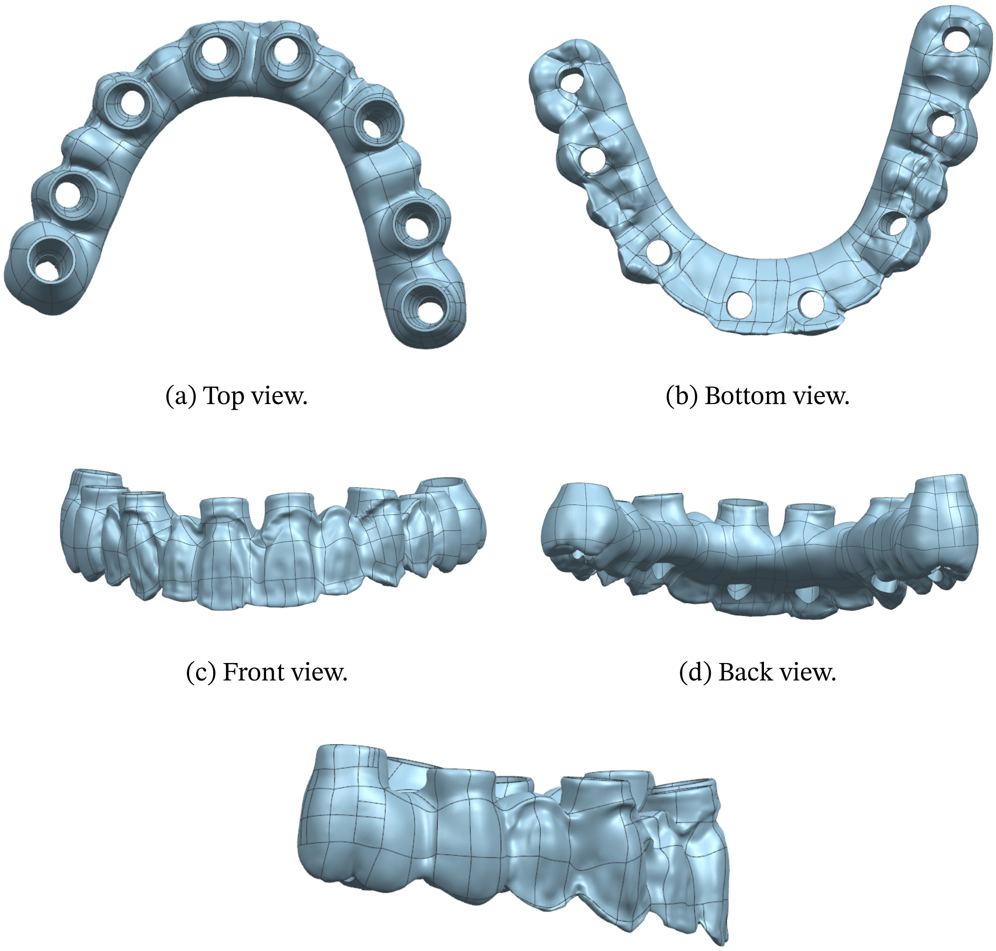

(a) Top view.

(b) Bottom view.

(c) Front view.

(d) Back view.

(e) Left view.

Figure 3.13.: Different views of the All-on-8 prosthesis.

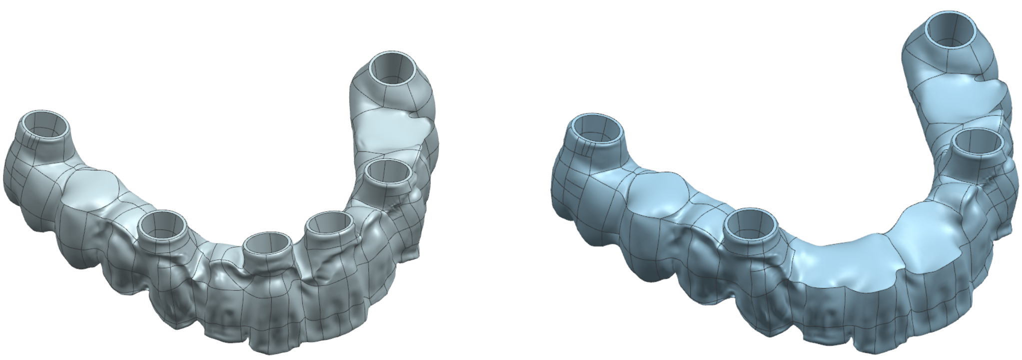

(a) All-on-6.

(b) All-on-4.

Figure 3.14.: Isometric views of the two other models

4. Finite Element Analysis

In the previous chapter, the procedure to reproduce an appropriate numerical model from a 3D scan is described. Now that this model is done, it is possible to generate a mesh. In this chapter, the choice of the mesh size is first discussed. Then, the material attribution is analysed. Finally, the results of the simulations are studied and discussed. The simulations are made in *Siemens Nastran*.

4.1. Mesh Accuracy Assessment

4.1.1. Element Type

The CAD model of an overdenture is not a conventional model. It is a highly irregular body, and it has to be very precise. To mesh the different models, 3D elements are used. To do so, the *3D Tetrahedral Mesh* tool is used. Tetrahedral elements are used and not hexahedrons because it is not possible to generate a hexahedral mesh on the overdenture. The geometry is too irregular and complex. Tetrahedral elements are however more expensive to solve than other types of elements. In other words, to achieve the same precision as with tetrahedra, it takes more elements. It is important to determine which type of elements to choose: tet4 or tet10. Tet4 are of first order, with one node per vertex. Tet10 are of second order, with 10 nodes: one per vertex and one at the centre of each edge. The edges of tet4 elements must remain perfectly straight (because there are no additional nodes), whereas tet10 elements can deform more. Furthermore, to achieve results as good as with tet10 using tet4 elements, many more elements would be required, which would add simulation time. Tet10 elements are thus used.

4.1.2. Mesh Generation

To generate the 3D mesh, the tool *3D Tetrahedral Mesh* of *Siemens NX1859* is used. With this tool, the desired type of tetrahedra must be specified. As mentioned earlier, *CTETRA(10)* is used. The element size must also be defined. This is actually an approximation of the edge length. Indeed, the software takes into account the geometry and potential mesh quality issues, so the length can vary. The other options are left at their default settings. In particular, *Model Cleanup Options* is set to 10%. This means that if a face or hole is present but is smaller than 10% of the chosen size, the software ignores it and does not mesh it.
It is chosen to consider a uniform mesh size in the whole model. Since the geometry is complex, it would take a lot of time to consider meshing it with different element sizes. The mesh size is chosen in such a way that the results converge in the most critical areas of the mesh. It is, however, too refined in less critical regions, and it leads to higher computational time. Defining different mesh sizes would have required constructing the overdenture as an assembly of bodies, which would have taken a lot more time. As is explained in Section 4.1.3, the simulations do not take much time. Therefore, it was a good compromise to consider the prosthesis as a single body, uniformly meshed.

4.1.3. Mesh Convergence Analysis

It is primordial to assess the accuracy of the generated mesh. A good mesh yields a result that converges to a solution and is independent of the mesh element size. Once convergence is achieved,

further refinement of the mesh is not necessary.
To analyse the impact of mesh size on results, a displacement of 50 [μm] is applied to the All-on-4 model on the first access hole, as highlighted in Figure 4.1. An access hole in implant dentistry refers to an opening in the artificial tooth of a screw-retained dental implant. This opening allows access to the abutment or screw that secures the prosthesis.
The computer's characteristics are : 12TH GEN INTEL(R) CORE(TM) I7-12700H 2.30 GHZ processor with a RAM of 16Go. 16 CPUs are used for the simulations.

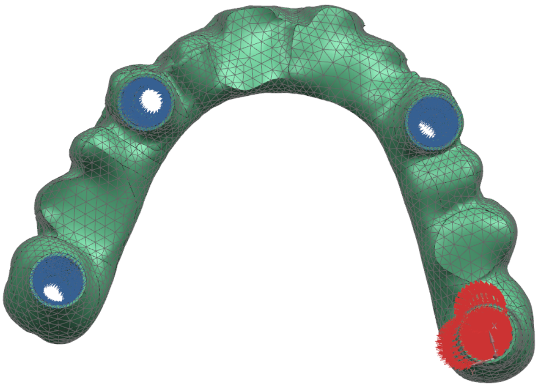

(a) Boundaries conditions applied on the overdenture. The fixed constraints are in blue and the enforced displacement load is in red.

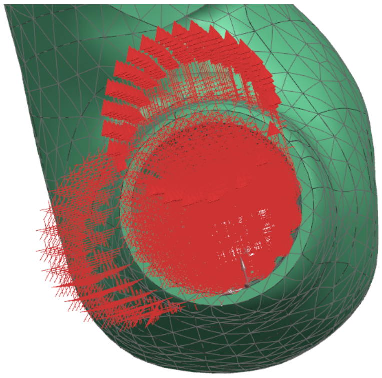

(b) Zoom on the enforced displacement load to see the direction. It is tangential to the overdenture.

Figure 4.1.: Constraints and load applied to the All-on-4 prosthesis.

Figure 4.2 illustrates how the Strain Energy Error evolves with the number of elements. Additionally, the figures depict the computational time corresponding to the number of elements. Figure 4.3 shows how the Relative Error in Steady Stress and the Computational Time evolve with the number of elements.

The goal is to achieve errors as small as possible while keeping computational time relatively low. The smallest simulated mesh has a size of 0.3 [mm]. A good compromise between accuracy and computational time appears to be a mesh size of 0.5 [mm]. It allows having both a Strain Energy Error and a Steady Stress Relative Error smaller than 5 [%].

To summarize, the model is meshed with a 3D tetrahedral mesh with elements of 0.5 [mm] of type *CTETRA(10)* (tet10).

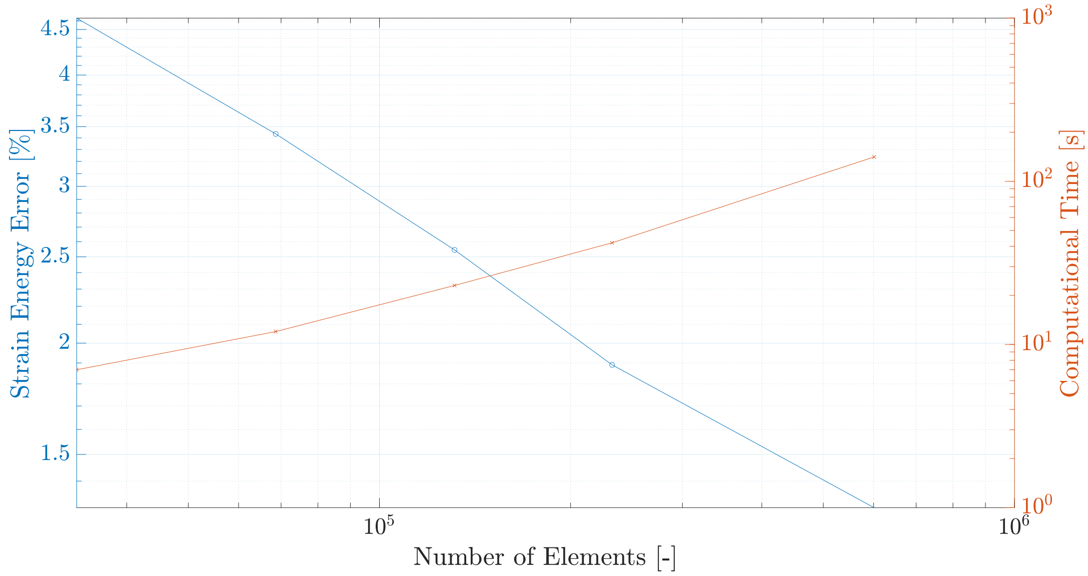

Figure 4.2.: Log-log plot of Strain Energy Error and Computational Time as a function of the number of elements.

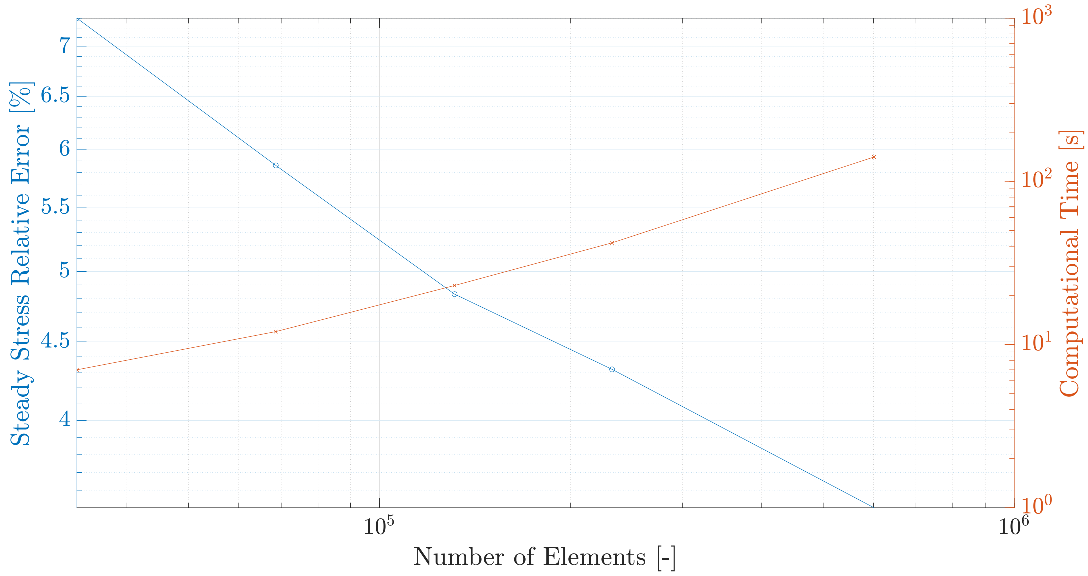

Figure 4.3.: Log-log plot of Steady Stress Relative Error and Computational Time as a function of the number of elements.

4.2. Material Attribution

As mentioned in previous sections, there are two types of materials used for complete dental prostheses. The first one is the Ti-6Al-4V, a titanium alloy. It is the cheapest solution, but it is less aesthetic than the Zirconia solution. This material is available in the material list of *Siemens NX1859*. Its properties are the following: a density of 4430 [kg/m^3], a Young's modulus of 121 [GPa], a Poisson's ratio of 0.34 [-], a yield strength of 805 [MPa] and a tensile strength of 845 [MPa].

The second material is Yttria-Stabilized Tetragonal Zirconia (Y TZP). It has an excellent combination of strength and toughness together with bio-inert properties and low wear rate. Its composition is Zirconia (ZrO_2), stabilized in its tetragonal form by a small addition of yttria, Y_2O_3.The properties of Zirconia Y TZP are the following: a density of 6000 [kg/m^3], a Young's modulus of 210 [GPa], a Poisson's ratio of 0.23 [-] a yield strength and tensile strength of 800 [MPa] [67].

Three models are created for each material: an All-on-8, an All-on-6 and an All-on-4.

4.3. Load Cases

Since dentures can be considered symmetrical, only half of the access holes undergo displacement. This section discusses the enforced displacement load as well as the boundary conditions applied to the different overdentures. For each access hole, three directions are considered: tangent, normal, and binormal to the prosthesis. This allows determining which direction is the most detrimental and the impact that different misfits have on the prosthesis.

Since All-on-4 and All-on-6 prostheses are essentially All-on-8 with fewer implants, the coordinate system for each access hole is shown for the All-on-8 prostheses. Then, the different displacements imposed are discussed. Afterwards, the various boundary conditions are reviewed.

4.3.1. Coordinate Systems of the All-on-8 Prosthesis

One can see 3 axes on the different figures. The x-axis is the tangent direction, the y-axis the binormal direction, and the z-axis is the normal. It is important to note that each access hole has its own coordinate system. The coordinate systems for the different access holes are shown in Figures 4.4, 4.5, 4.6 and 4.7.

(a) Top view.

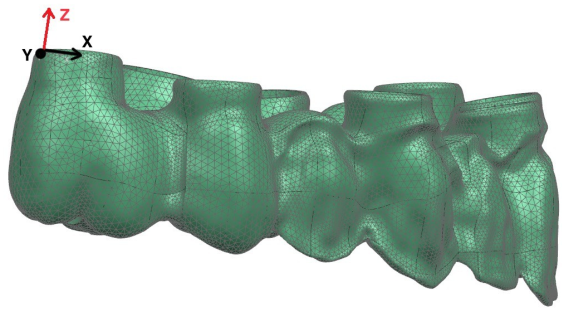

(b) Left view.

Figure 4.4.: Coordinate system of the first access hole of the All-on-8 prosthesis.

(a) Top view.

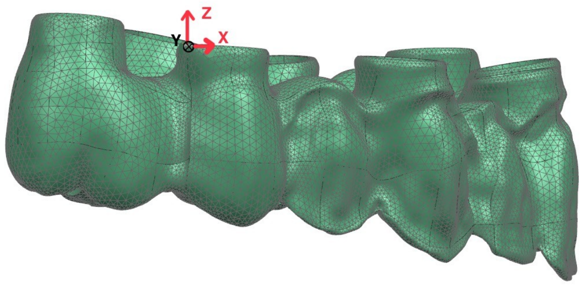

(b) Left view.

Figure 4.5.: Coordinate system of the second access hole of the All-on-8 prosthesis.

(a) Top view.

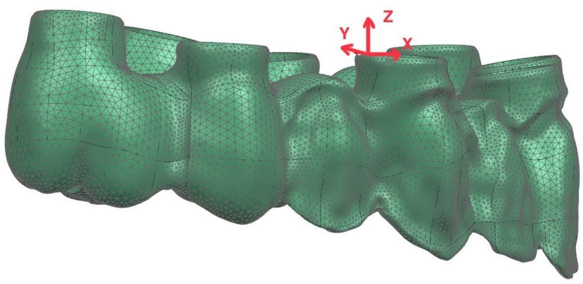

(b) Left view.

Figure 4.6.: Coordinate system of the third access hole of the All-on-8 prosthesis.

(a) Top view.

(b) Left view.

Figure 4.7.: Coordinate system of the fourth implant of the All-on-8 prosthesis.

4.3.2. Imposed Displacements

For each access hole and for each direction, a misfit of 50 [μm] is imposed. As explained in Chapter 2, a misfit is defined as the absence of simultaneous contact of all fitting surfaces. In this thesis, the misfit is applied to the surfaces in contact with the abutment and the prosthetic screw. This is illustrated in Figure 4.8a. A zoom on the surface is shown in Figure 4.8b. The misfit is an axial displacement load. It is imposed using the *Enforced Motion Load* tool located in the *Load Type* menu of *Siemens NX1859*. There is thus 3 load cases for each access hole. As explained in the following sections, the overdenture can be considered as a linear system and can thus be illustrated using the equation for a spring. A displacement is applied which causes a reaction force. The stiffness of the prosthesis is then available. After determining the stiffness of the bone, the implant and the overdenture, it is possible to determine the effect of a misfit on the system.

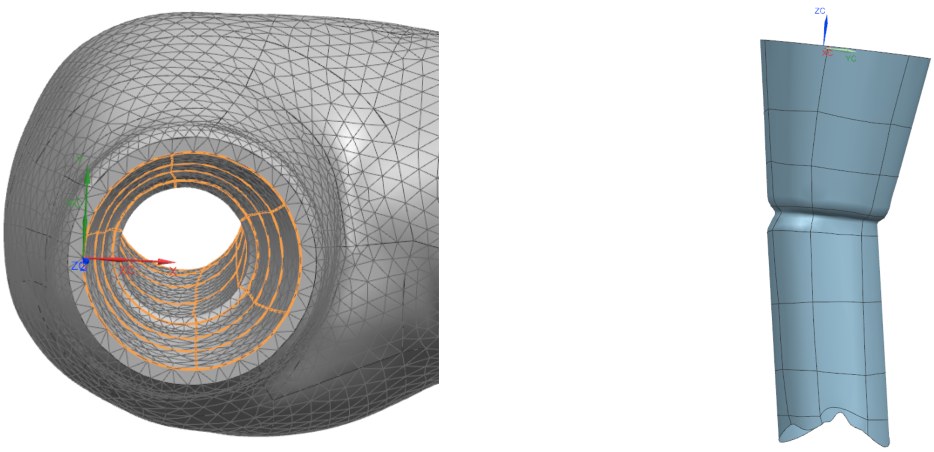

(a) Surfaces (in orange) where the misfit is located.

(b) Zoom on the surfaces.

Figure 4.8.: Location of the applied misfit.

4.3.3. Boundary Conditions

Since it is considered that there is only one misfit in the system, it is necessary to constraint the motion of the seven other access holes.
All motions must be fixed. This is achieved by using the *Fixed Constraint* tool in the *Constraint Type* menu of *Siemens NX1859*.
As for the displacement load, it is also applied to the surfaces in contact with the abutment and prosthetic screw. The different fixed constraints can be seen in Figure 4.9.
Since these access holes are fixed, the displacement at these locations is supposed to be null. If this is not the case, the problem is ill-posed. It can be seen in Figure 4.10 that at the locations where the fixed constraints were imposed, the displacement is equal to 0. This view is obtained when plotting the iso-surfaces of the simulation. In the darkest blue, the displacement is null.

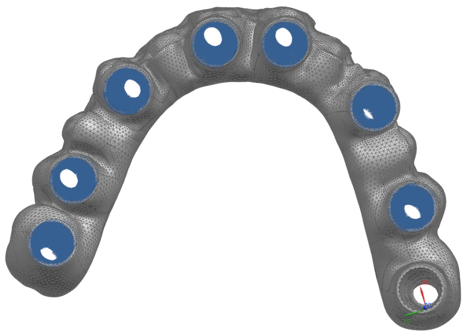

Figure 4.9.: Fixed constraints (in blue).

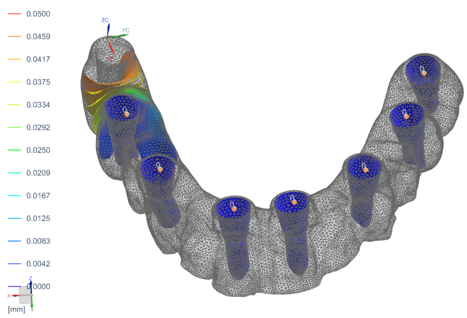

Figure 4.10.: Iso-surfaces of an enforced displacement load of 50 [μm] in the tangent direction of the first access hole. The inside of the constrained access holes have all a zero displacement.

4.4. Static Linear Analysis

Now that the load and boundary conditions are applied, a linear static analysis is conducted, and the results are discussed. In this section, the titanium cases are assessed first, followed by the zirconia ones. Then, the two different materials are compared.
The denture can be considered as a linear system, and it can be illustrated using Hooke's law, stated in Equation 4.1, where F is the force applied to the spring, k is its stiffness, and x is its displacement from its equilibrium position.

$$F = kx. \tag{4.1}$$

When considering a prosthesis, each access hole can be seen as a point of constraint or a point where forces and displacements can be applied. When considering the prosthesis as a spring, the displacement of the loaded access hole can be seen as the displacement of a spring.

In this thesis, different misfits are applied to the prostheses and these misfits induce a displacement of one of the access holes. The displacement induces a reaction force in the prosthesis, that acts like a spring with a certain stiffness, $k_{prosthesis}$. This stiffness varies with different parameters, that are the displacement, the reaction force, the material, the number of implants and the access hole where the misfit is located. In the studied system (prosthesis and bone), there are three stiffnesses that should be compared: $k_{prosthesis}$, $k_{implant}$ and k_{bone}. As mentioned earlier, the main issues occur if the bone is damaged. It is thus favourable that if something was to break, it would be the prosthesis. This means that the stiffness of the prosthesis should be smaller than that of the implant or of the bone. If $k_{prosthesis}$ is greater than $k_{implant}$ or k_{bone}, this means that the prosthesis is stiffer and that the major part of the forces are transmitted to the bone or the implant. The implant and the bone have to absorb these forces. It is not a favourable situation. At the implant level, if not stiff enough, it could be deformed, displaced or fractured, which would compromise its stability and integrity. At the bone level, it could cause a loss of osseointegration around the implant, fracture or bone resorption. It is thus necessary to assure an equilibrium between the prothesis, implants and bone. It is important that the stiffness of the prosthesis is smaller than the stiffnesses of the bone and the implants. It absorbs the major part of the deformations induced by the displacement.

The two materials used for prostheses are Ti-6Al-4V and zirconia Y-TZP. The stiffness of a material is characterized by its Young's modulus. The higher the modulus is, the stiffer the object is. As mentioned above, the used titanium has a Young's modulus of 121 [GPa] and the zirconia has a modulus of 210 [GPa]. The latter is thus stiffer. There is thus a huge difference in the stress distribution. Titanium stiffness compared to zirconia makes it more similar to bone. However, it still is far from the elastic modulus of bone tissue (5 to 30 [GPa]).

For each prosthesis, a misfit of 50 [μm] is applied to half of the access holes. In the context of a linear problem, if the relationship between displacement and reaction force is linear, then the reaction force is proportional to the displacement. This means that if a displacement of 50 [μm] results in a reaction force F, then a displacement of 100 [μm] will result in twice the reaction force. It is explained by Hooke's Law, where the force is proportional to the displacement, since k is a proportionality constant.
There are six directions of space. But in a linear system, a displacement of 50 microns in the +x direction produces a reaction force F, while a displacement of 50 microns in the -x direction produces a reaction force -F, with the forces having the same magnitude but opposite directions. It is thus enough to analyse only the x, y and z directions and only one value of misfit.

4.4.1. Titanium Cases

First, the different misfits are applied to the All-on-8, All-on-6 and All-on-4 frameworks in titanium. Only the cases for 50 [μm] are discussed, since the results for 100 and 150 microns are proportional.

All the stress values presented are Von Mises stresses.

All-on-8 Prosthesis

Each access hole is analysed, starting with the first and ending with the fourth. For each spatial direction, three graphs are shown for a 50 [μm] misfit: displacement, stress, and reaction force. The displacements shown are exaggerated. The model deformation is set to *10% model* in *Siemens NX*. It displays the relative deformation of the model, scaling the maximum deformation to 10% of the model's size [68].

First Access Hole Figure 4.11 illustrates the displacement, stress and reaction forces caused by a 50 [μm] misfit in the tangent direction. In Figure 4.11a, the displacement caused by a 50 [μm] misfit in the tangent direction can be seen. The stress is shown in Figures 4.11b, 4.11c and 4.11d. The reaction forces at the important locations are displayed in Figures 4.11e and 4.11f. In Figures 4.12 and 4.13, the displacement, stress and reaction forces are shown for the binormal and normal directions.

In Figures 4.11b, 4.11c and 4.11d, the stress distribution resulting from a 50 [μm] misfit on the first access hole can be seen. Stress concentration is observed inside the first and second access holes, as well as in the region between them. The maximum stress, approximately 2580 [MPa], occurs in this inter-hole region, while the maximum stress inside the access holes is around 1200 [MPa]. Some nodes exhibit singularities and thus should be excluded from the analysis. In Figures 4.11e and 4.11f, the reaction forces of the two first access holes can be seen. It is in these two regions that the forces are the highest, approximately 85 [N]. These are discussed in Section 4.4.5.

In Figure 4.12a, the displacement caused by a misfit in the binormal direction is seen. The stress distribution can be seen in Figures 4.12b, 4.12c and 4.12d. The maximum stress, approximately 1100 [MPa], is located in the first inter-hole region. Stress concentration is also observed in the two first access holes, and the maximum in these two regions is 800 [MPa]. Once again, as can be seen in Figures 4.12e and 4.12f, the maximum reaction forces are located inside the two first access holes.

In Figure 4.13a, the displacement caused by a misfit in the normal direction is seen. The stress distribution is shown in Figures 4.13b, 4.13c and 4.13d and the same conclusion as for the two other directions can be drawn. The maximum stress in this region is approximately 1620 [MPa].

(a) Exaggerated displacement.

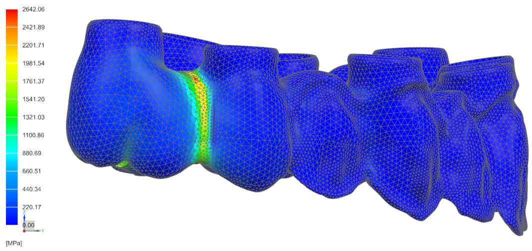

(b) Stress. Left view.

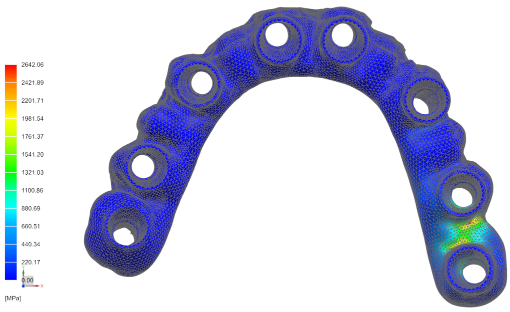

(c) Stress. Top view.

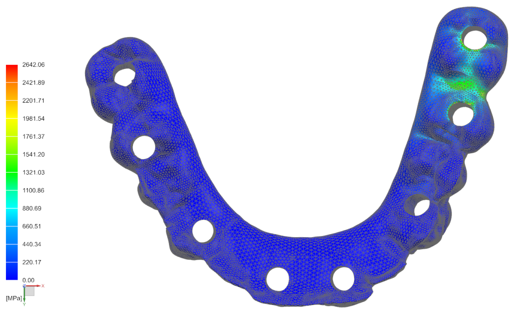

(d) Stress. Bottom view.

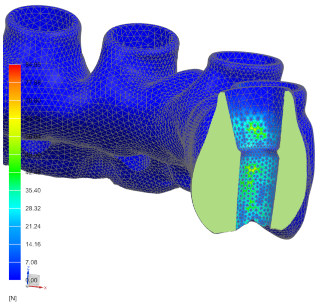

(e) Reaction forces. View inside the first access hole.

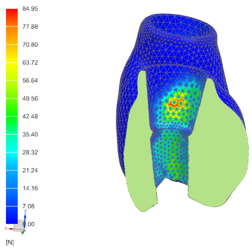

(f) Reaction forces. View inside the second access hole.

Figure 4.11.: 50 [μm] misfit in the tangent direction applied on the first access hole of an All-on-8 prosthesis.

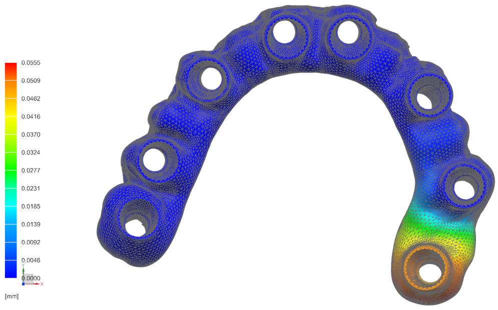

(a) Exaggerated displacement.

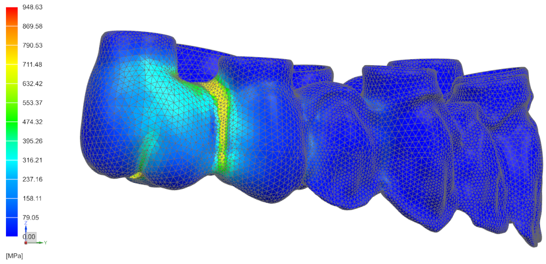

(b) Stress. Left view.

(c) Stress. Top view.

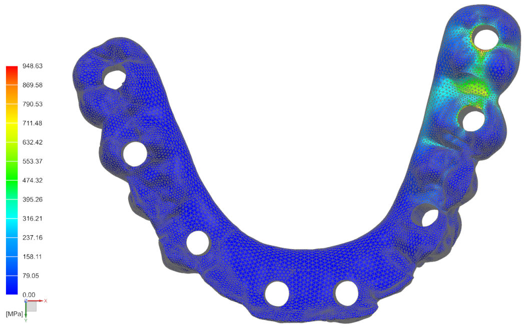

(d) Stress. Bottom view.

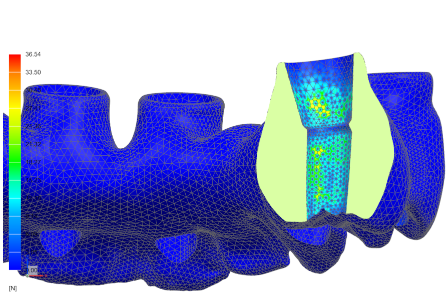

(e) Reactions forces. View inside the first access hole.

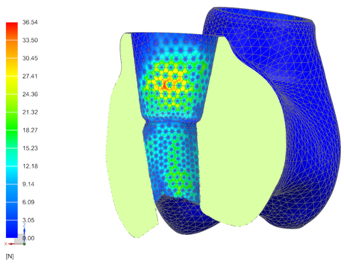

(f) Reactions forces. View inside the second access hole.

Figure 4.12.: 50 [μm] misfit in the binormal direction applied on the first access hole of an All-on-8 prosthesis.

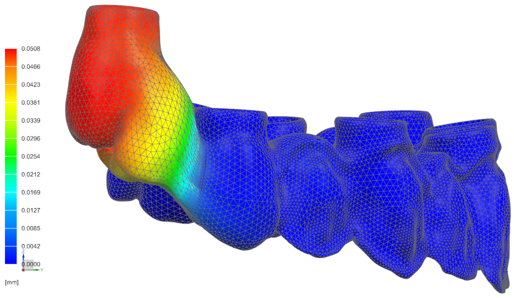

(a) Exaggerated displacement.

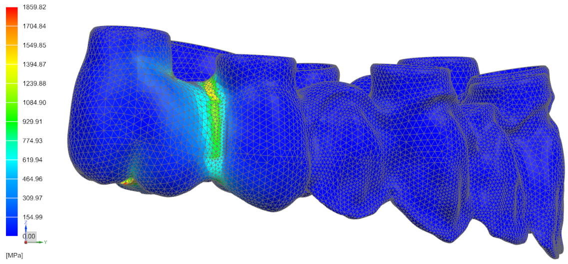

(b) Stress. Left view.

(c) Stress. Top view.

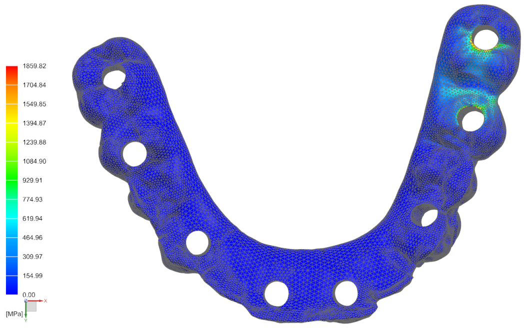

(d) Stress. Bottom view.

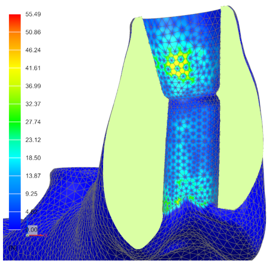

(e) Reactions forces. View inside the first access hole.

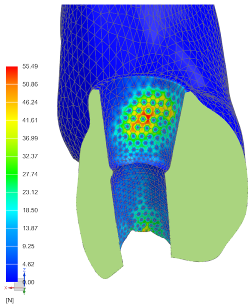

(f) Reactions forces. View inside the second access hole.

Figure 4.13.: 50 $[\mu m]$ misfit in the normal direction applied on the first access hole of an All-on-8 prosthesis.

The most detrimental direction for the first access hole is thus the tangent one, and the least detrimental is the binormal direction.

Second Access Hole In this paragraph, a 50 [μm] is applied to the second access hole of the All-on-8 prosthesis.

For the tangent direction, the displacement and stress concentrations are shown in Figure 4.14 and the reaction forces in Figure 4.16. There is a singularity in the model that can be seen in Figure 4.15. This value has to be removed from the analysis. The stress concentrations are mainly located in the first and second inter-hole regions. The stress in these regions range between 1000 and 2660 [MPa] as can be seen in Figures 4.14b, 4.14c and 4.14d. The reaction forces are higher in the first three access holes, with the maximum value of 87 [N] inside the second one.

In the binormal direction, the same analysis is run and shown in Figures 4.17 and 4.18. The same conclusions can be drawn as for the first access hole concerning the regions of stress concentrations and reaction forces. When the singularities are removed from the analysis, the maximum stress is approximately 1200 [MPa].

The same conclusions can be drawn for the normal direction shown in Figures 4.19 and 4.20. When excluding the singularity, the stress concentration values range between 900 and 1740 [MPa].

The most detrimental direction is again the tangent one, followed by the normal and finally the binormal.

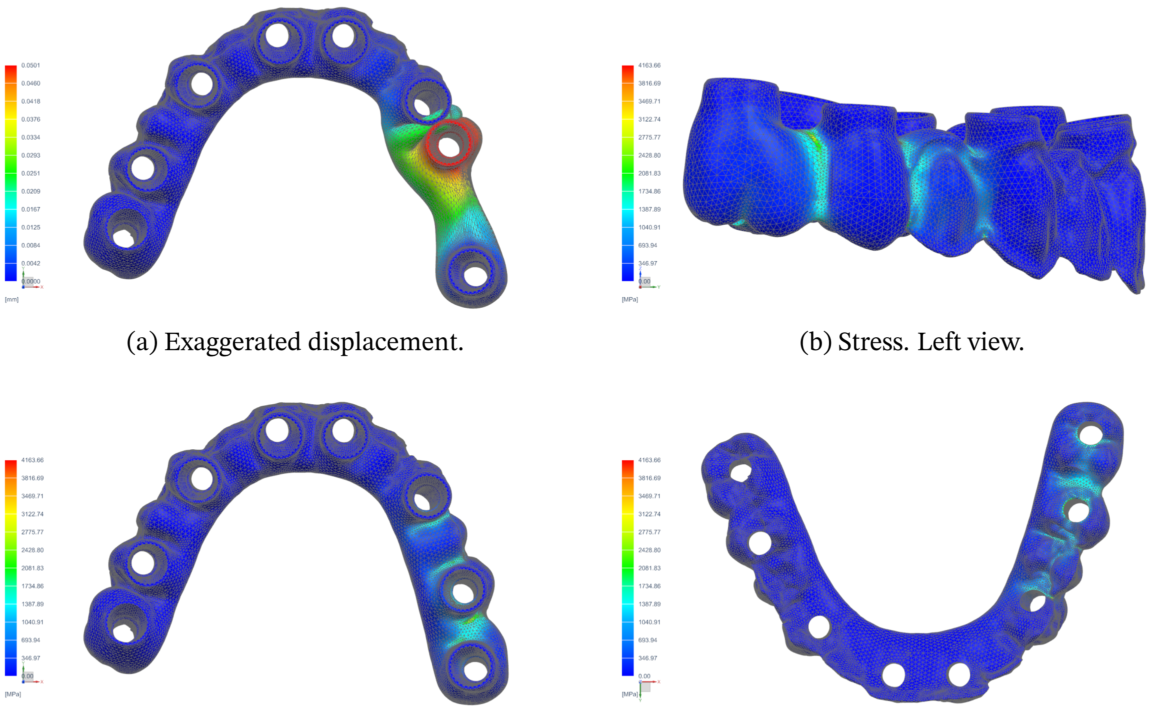

(a) Exaggerated displacement.

(b) Stress. Left view.

(c) Stress. Top view.

(d) Stress. Bottom view.

Figure 4.14.: Displacement and stress caused by a 50 [μm] misfit in the tangent direction applied on the second access hole of an All-on-8 prosthesis.

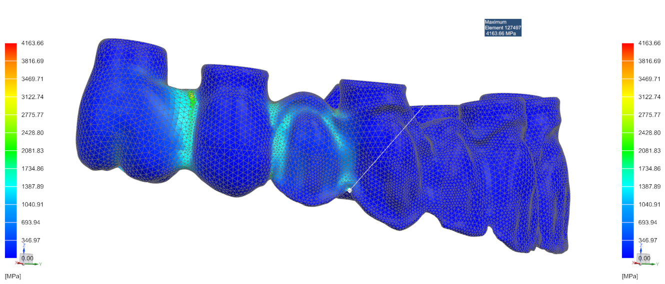

(a) Localization.

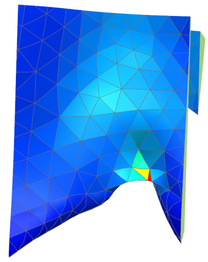

(b) Zoom.

Figure 4.15.: Singularity when a 50 $[\mu m]$ misfit in the tangent direction is applied on the second access hole of an All-on-8 prosthesis.

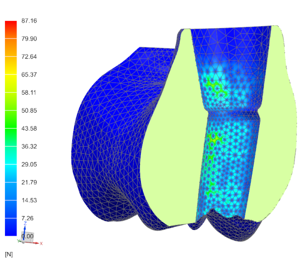

(a) Reaction forces on the first access hole.

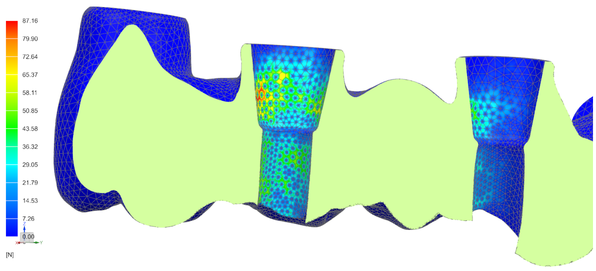

(b) Reaction forces on the second access hole.

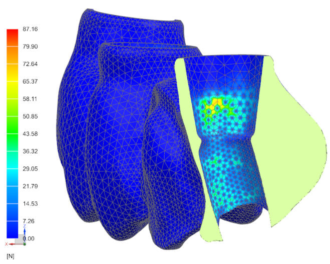

(c) Reaction forces on the third access hole.

Figure 4.16.: Reaction forces for an All-on-8 prosthesis with a 50 $[\mu m]$ misfit in the tangent direction applied on the second access hole.

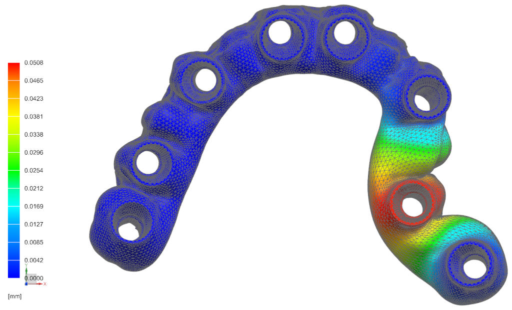

(a) Exaggerated displacement.

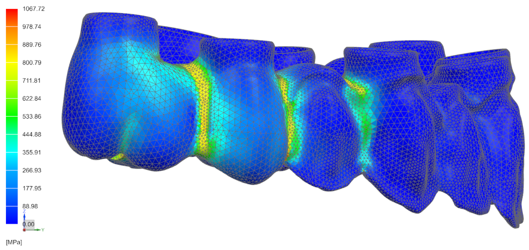

(b) Stress. Left view.

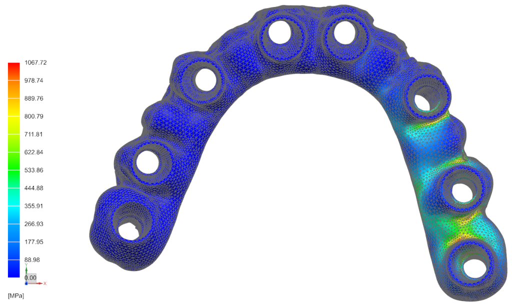

(c) Stress. Top view.

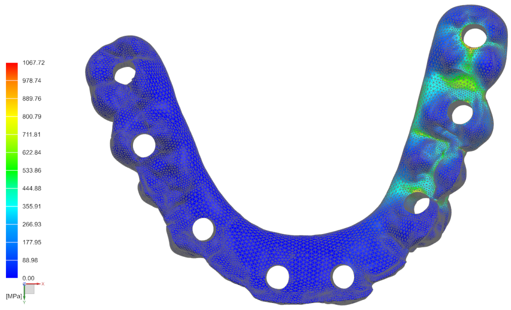

(d) Stress. Bottom view.

Figure 4.17.: Displacement and stress caused by a 50 [μm] misfit in the binormal direction applied on the second access hole of an All-on-8 prosthesis.

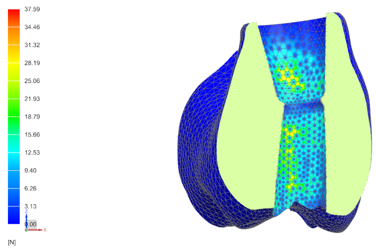

(a) Reaction forces on the first access hole.

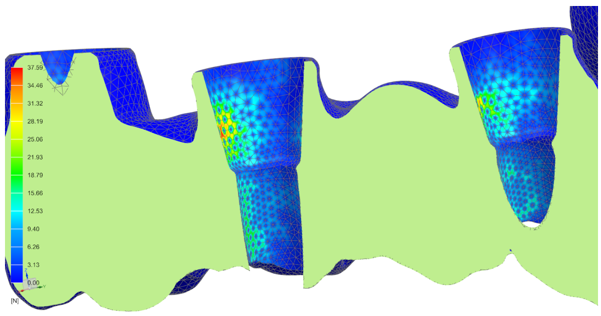

(b) Reaction forces on the second access hole.

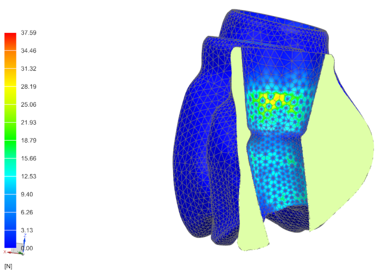

(c) Reaction forces on the third access hole.

Figure 4.18.: Reaction forces for an All-on-8 prosthesis with a 50 [μm] misfit in the binormal direction applied on the second access hole.

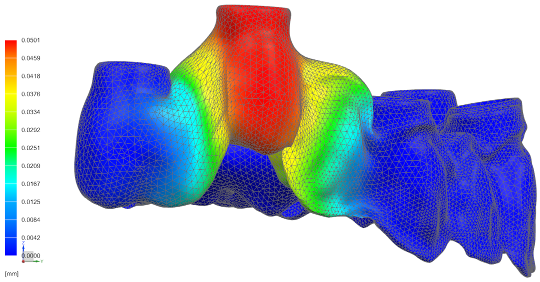

(a) Exaggerated displacement.

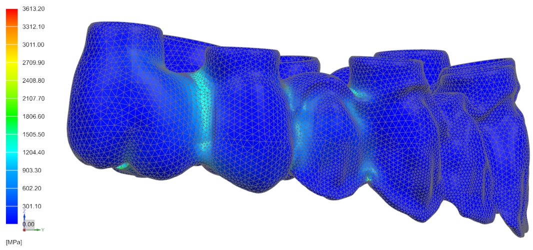

(b) Stress. Left view.

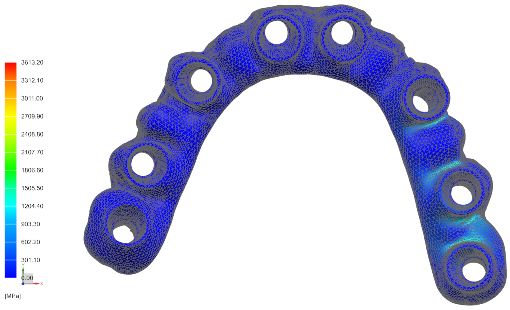

(c) Stress. Top view.

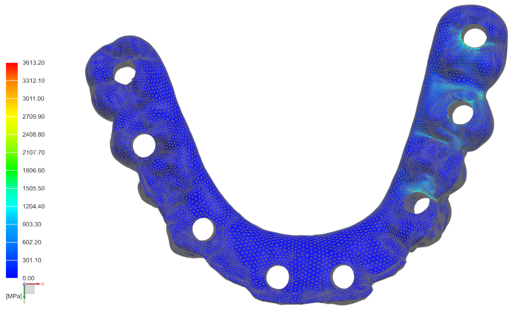

(d) Stress. Bottom view.

Figure 4.19.: Displacement and stress caused by a 50 [μm] misfit in the binormal direction applied on the second access hole of an All-on-8 prosthesis.

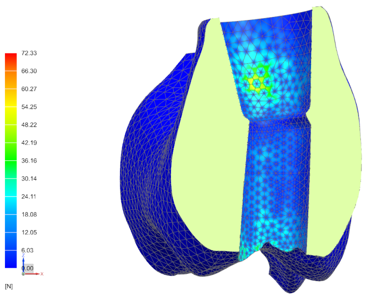

(a) Reaction forces on the first access hole.

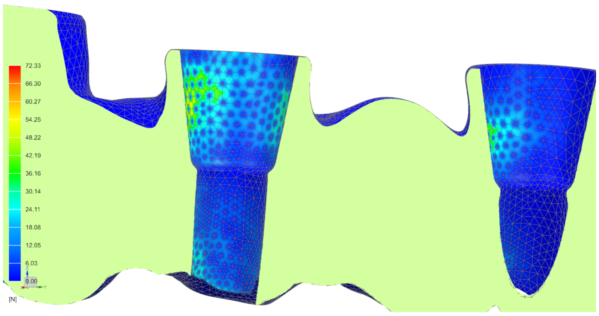

(b) Reaction forces on the second access hole.

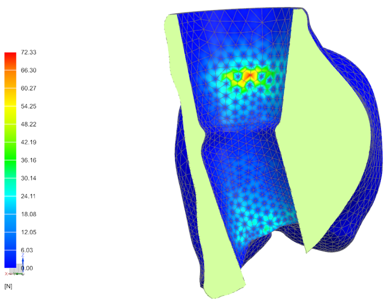

(c) Reaction forces on the third access hole.

Figure 4.20.: Reaction forces for an All-on-8 prosthesis with a 50 [μm] misfit in the normal direction applied on the second access hole.

Third Access Hole The 50 [μm] misfit is now located in the third access hole.

For the tangent displacement, the stress concentrations are now located in the inter-hole regions between the first access hole and the second one and between the second and third access holes. This can be observed from Figure 4.21. The maximum stress on Figures 4.21b, 4.21c and 4.21d is due to a singularity and has thus to be excluded. The maximum stress is thus approximately 1980 [MPa]. There are reaction forces in the second, third and fourth access holes as can be seen in Figure 4.22.

In the binormal direction, the same conclusions are drawn when looking at Figures 4.23 and 4.24. The singularities are, once again, excluded and the maximum stress in concentration regions is around 1150 [MPa].

For the last direction, the maximum stress is equal to 1620 [MPa] as can be seen in Figures 4.25b, 4.25c and 4.25d.

The same conclusion as for the two other access holes concerning the most detrimental direction is drawn.

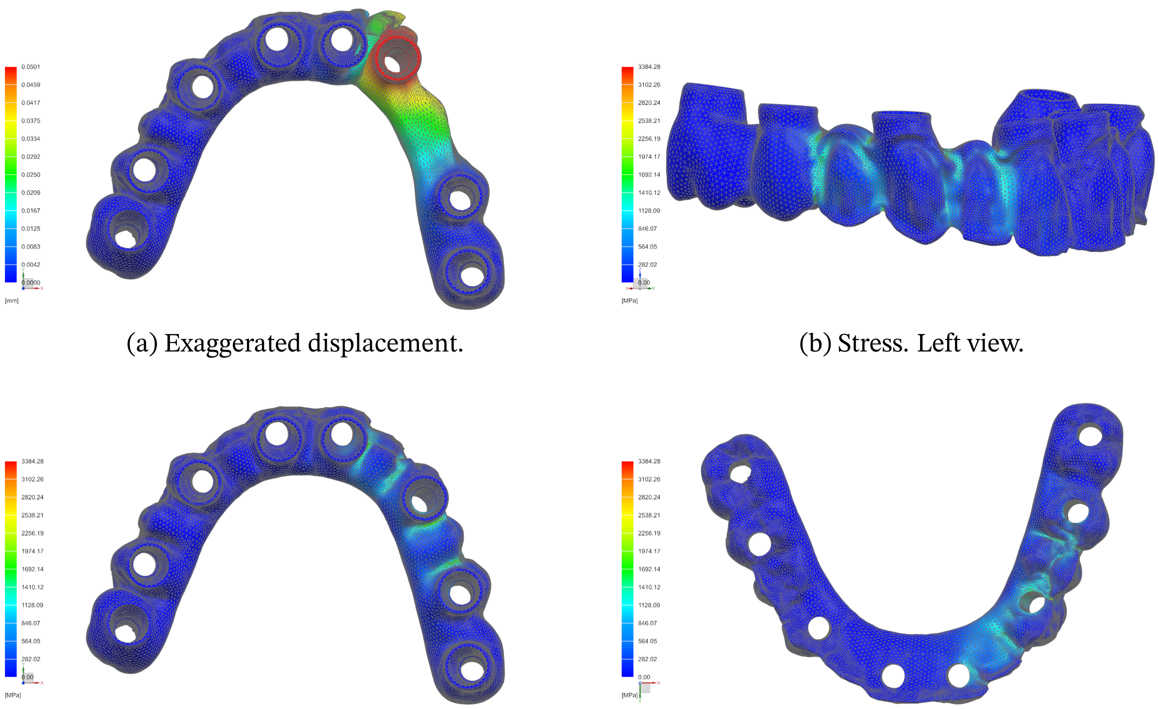

(a) Exaggerated displacement.

(b) Stress. Left view.

(c) Stress. Top view.

(d) Stress. Bottom view.

Figure 4.21.: Displacement and stress caused by a 50 [μm] misfit in the tangent direction applied on the third access hole of an All-on-8 prosthesis.

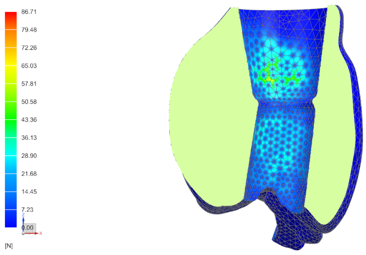

(a) Reaction forces on the second access hole.

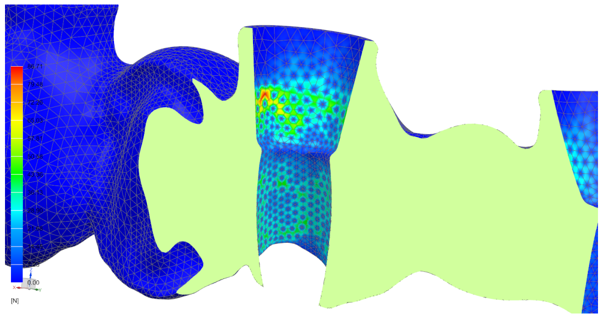

(b) Reaction forces on the third access hole.

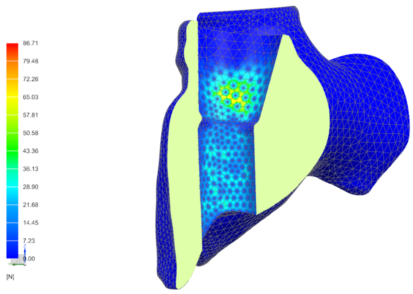

(c) Reaction forces on the fourth access hole.

Figure 4.22.: Reaction forces for an All-on-8 prosthesis with a 50 [μm] misfit in the tangent direction applied on the third access hole.

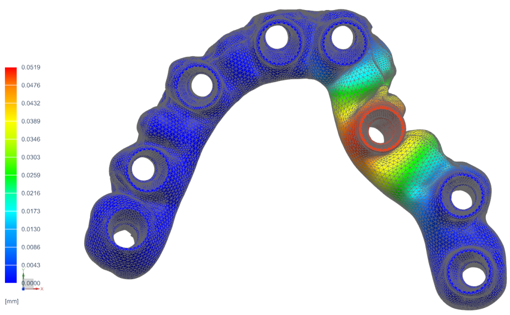

(a) Exaggerated displacement.

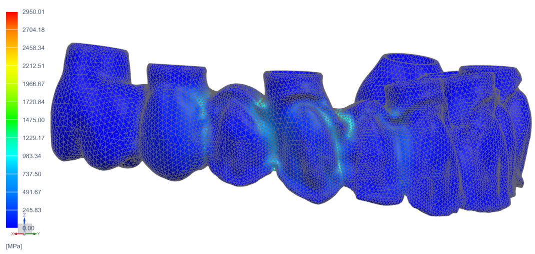

(b) Stress. Left view.

(c) Stress. Top view.

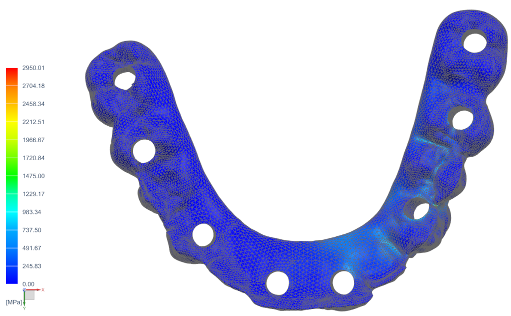

(d) Stress. Bottom view.

Figure 4.23.: Displacement and stress caused by a 50 [μm] misfit in the binormal direction applied on the third access hole of an All-on-8 prosthesis.

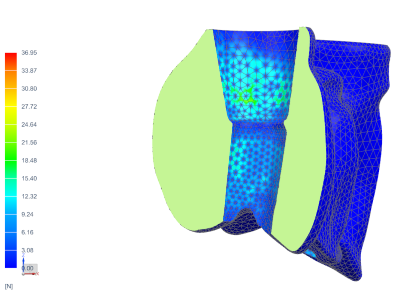

(a) Reaction forces on the second access hole.

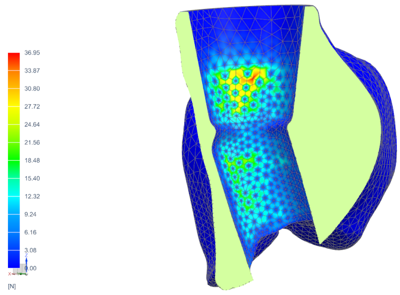

(b) Reaction forces on the third access hole.

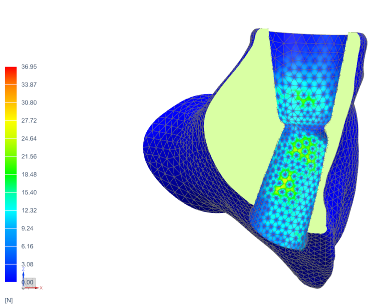

(c) Reaction forces on the third access hole.

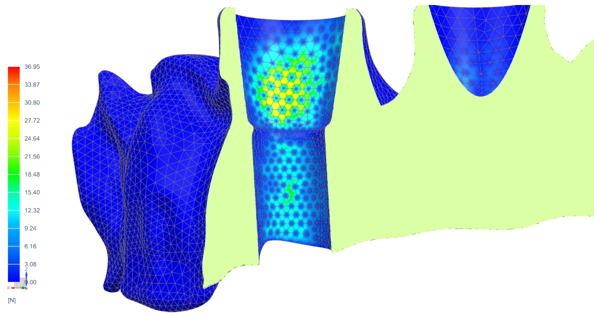

(d) Reaction forces on the fourth access hole.

Figure 4.24.: Reaction forces for an All-on-8 prosthesis with a 50 [μm] misfit in the binormal direction applied on the second access hole.

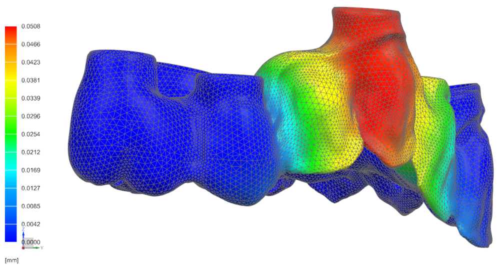

(a) Exaggerated displacement.

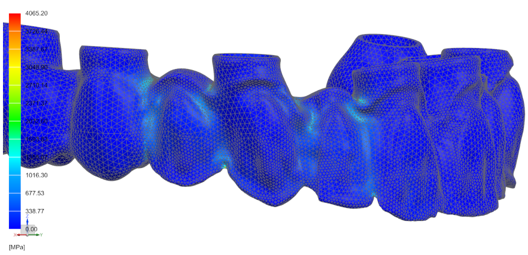

(b) Stress. Left view.

(c) Stress. Top view.

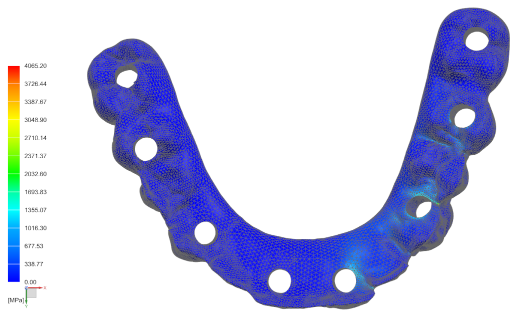

(d) Stress. Bottom view.

Figure 4.25.: Displacement and stress caused by a 50 [μm] misfit in the normal direction applied on the third access hole of an All-on-8 prosthesis.

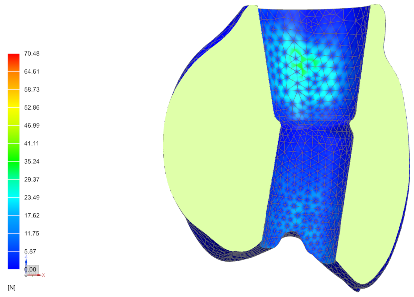

(a) Reaction forces on the second access hole.

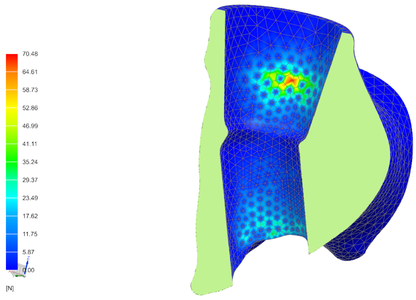

(b) Reaction forces on the third access hole.

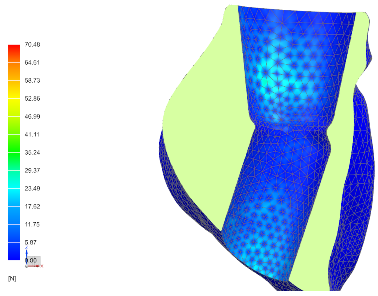

(c) Reaction forces on the third access hole.

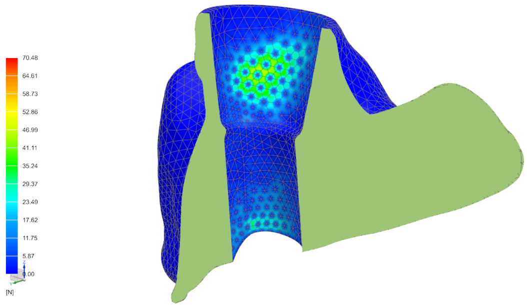

(d) Reaction forces on the fourth access hole.

Figure 4.26.: Reaction forces for an All-on-8 prosthesis with a 50 [μm] misfit in the normal direction applied on the third access hole.

Fourth Access Hole When comparing Figures 4.27, 4.29 and 4.31, it is observable that the most detrimental direction is the tangent one and the maximum stress is around 3500 [MPa]. The binormal direction presents a maximum stress of 1880 [MPa] and the normal one of 2050 [MPa]. For the three directions, stress constraints are located between the third and fourth access holes and between the fourth and fifth access holes. It can be seen in Figures 4.28, 4.30 and 4.32 that the reaction forces are higher in the third, fourth and fifth access holes.

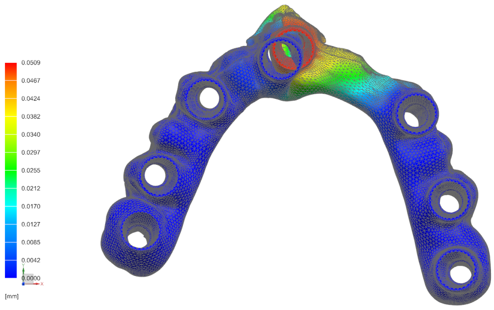

(a) Exaggerated displacement.

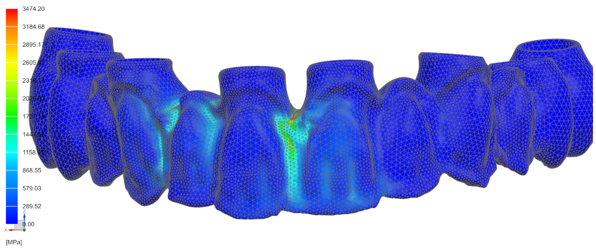

(b) Stress. Face view.

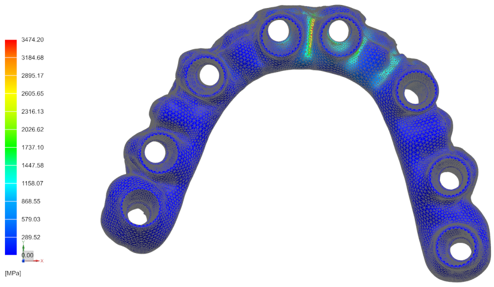

(c) Stress. Top view.

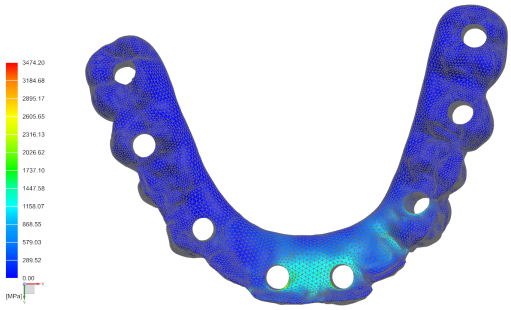

(d) Stress. Bottom view.

Figure 4.27.: Displacement and stress caused by a 50 [μm] misfit in the tangent direction applied on the fourth access hole of an All-on-8 prosthesis.

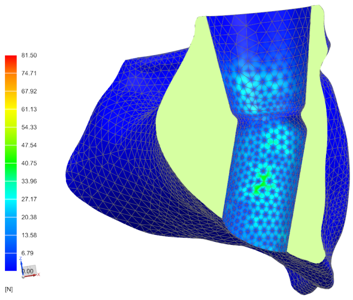

(a) Reaction forces on the third access hole.

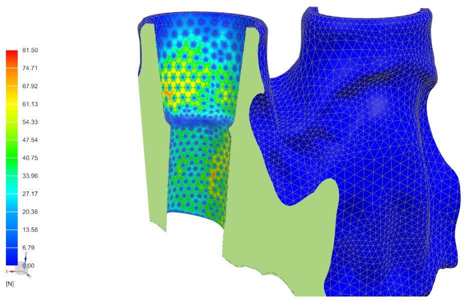

(b) Reaction forces on the fourth access hole.

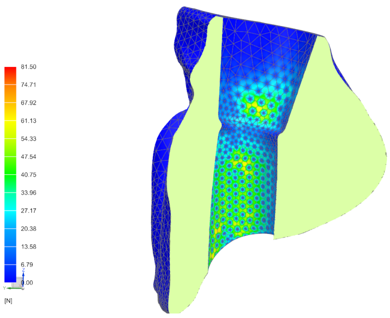

(c) Reaction forces on the fifth access hole.

Figure 4.28.: Reaction forces for an All-on-8 prosthesis with a 50 [μm] misfit in the tangent direction applied on the fourth access hole.

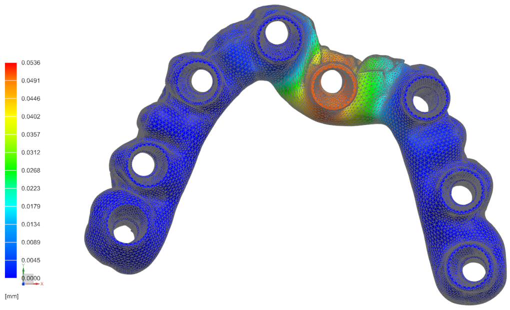

(a) Exaggerated displacement.

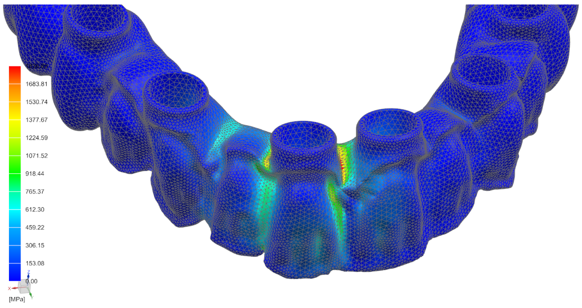

(b) Stress. Face view.

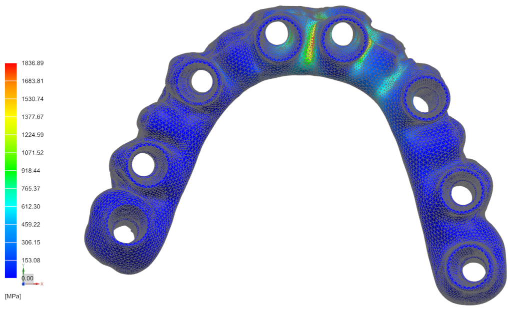

(c) Stress. Top view.

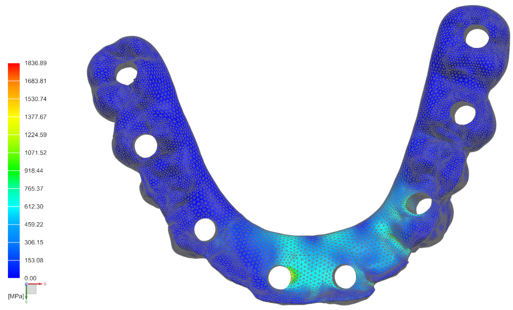

(d) Stress. Bottom view.

Figure 4.29.: Displacement and stress caused by a 50 [μm] misfit in the binormal direction applied on the fourth access hole of an All-on-8 prosthesis.

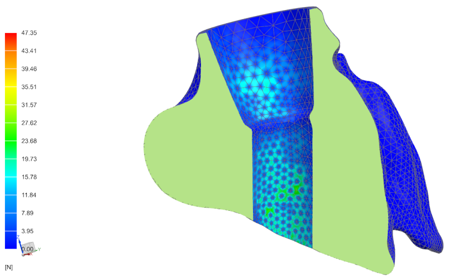

(a) Reaction forces on the third access hole.

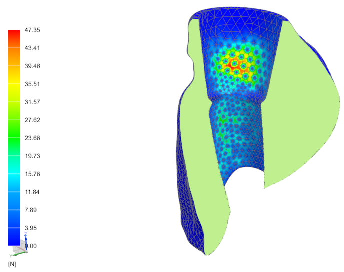

(b) Reaction forces on the fourth access hole.

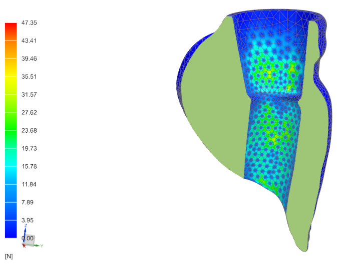

(c) Reaction forces on the fourth access hole.

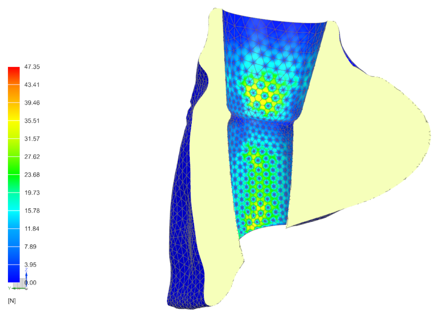

(d) Reaction forces on the fifth access hole.

Figure 4.30.: Reaction forces for an All-on-8 prosthesis with a 50 [μm] misfit in the binormal direction applied on the fourth access hole.

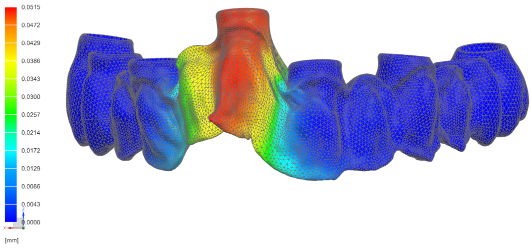

(a) Exaggerated displacement.

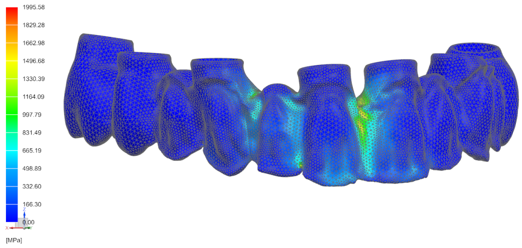

(b) Stress. Face view.

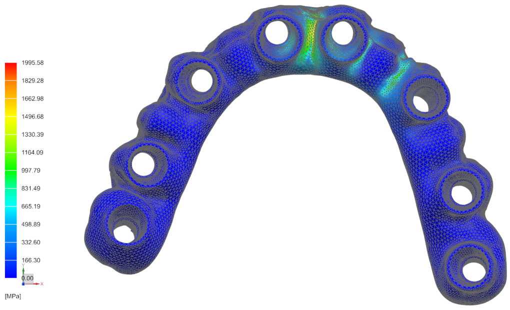

(c) Stress. Top view.

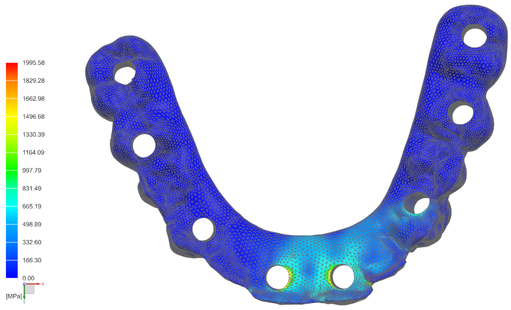

(d) Stress. Bottom view.

Figure 4.31.: Displacement and stress caused by a 50 [μm] misfit in the normal direction applied on the fourth access hole of an All-on-8 prosthesis.

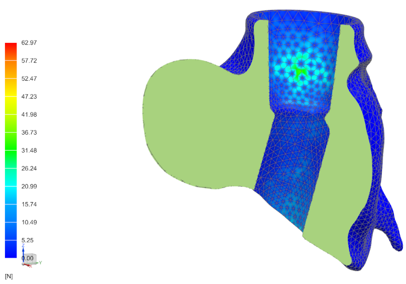

(a) Reaction forces on the third access hole.

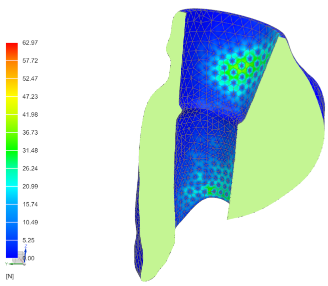

(b) Reaction forces on the fourth access hole.

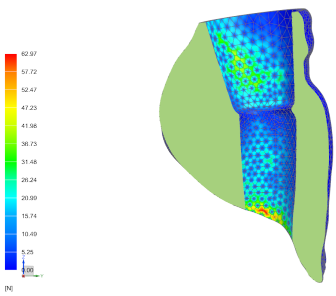

(c) Reaction forces on the fourth access hole.

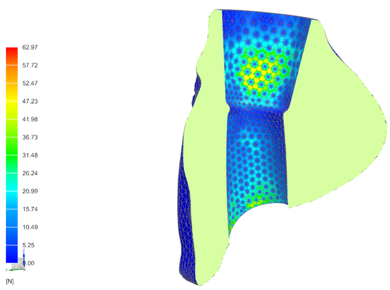

(d) Reaction forces on the fifth access hole.

Figure 4.32.: Reaction forces for an All-on-8 prosthesis with a 50 [μm] misfit in the normal direction applied on the fourth access hole.

Discussion For each implant analysed, the most detrimental direction is the tangent, followed by the normal and finally the binormal. In Table 4.1, a summary of the maximum stress values can be seen.
In every direction, the most detrimental access hole is the fourth one.

Implant Position	Direction	Maximum Stress [MPa]
First	Tangent	2580
	Binormal	1100
	Normal	1620
Second	Tangent	2660
	Binormal	1200
	Normal	1740
Third	Tangent	1980
	Binormal	1150
	Normal	1620
Fourth	Tangent	3500
	Binormal	1880
	Normal	2050

Table 4.1.: Comparison of the maximum stress in the different configurations for the All-on-8 prosthesis in titanium.

All-on-6 Prosthesis

First Access Hole In Figure 4.33, the displacement, stress and reaction forces when applying a 50 [μm] misfit in the tangent direction on the first access hole of an All-on-6 prosthesis are shown. As mentioned above, the singularities should not be taken into account in the stress analysis. The maximum stress constraints are located between the two first access holes and inside of them. The highest value is approximately 1170 [MPa]. As for the All-on-8 prosthesis, the reaction forces are mainly located inside the two first access holes.

In Figure 4.34, the misfit is applied in the binormal direction. The same conclusion can be drawn than for the tangent direction, except that the highest value of the stresses is approximately 390 [MPa].

For the binormal direction, when looking at Figure 4.35, the same observations can be conducted. The maximum stress is around 780 [MPa].

The tangent direction is thus the most detrimental for the first access hole, followed by the normal one.

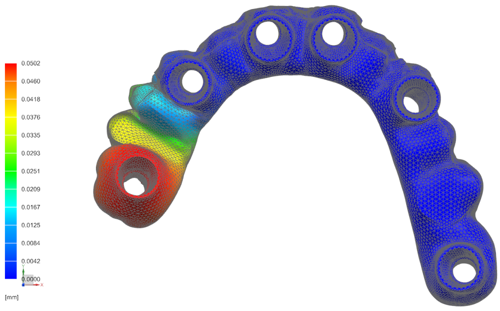

(a) Exaggerated displacement.

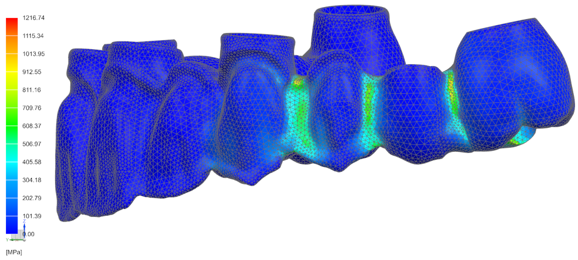

(b) Stress. Right view.

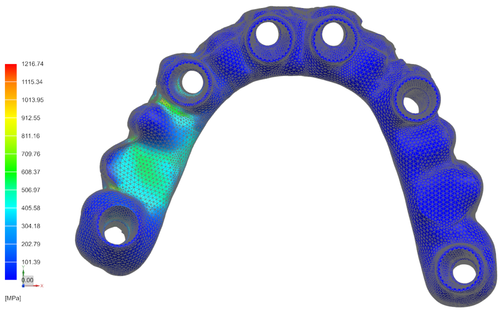

(c) Stress. Top view.

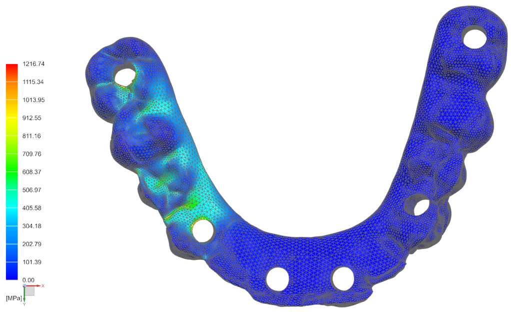

(d) Stress. Bottom view.

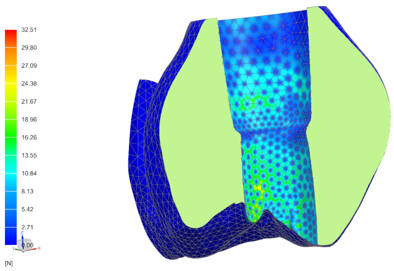

(e) Reaction forces. View inside the first access hole.

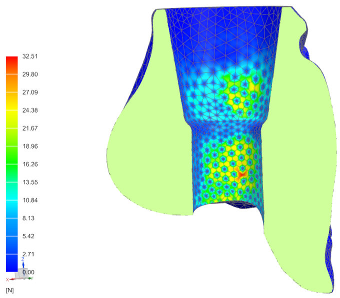

(f) Reaction forces. View inside the second access hole.

Figure 4.33.: 50 [μm] misfit in the tangent direction applied on the first access hole of an All-on-6 prosthesis.

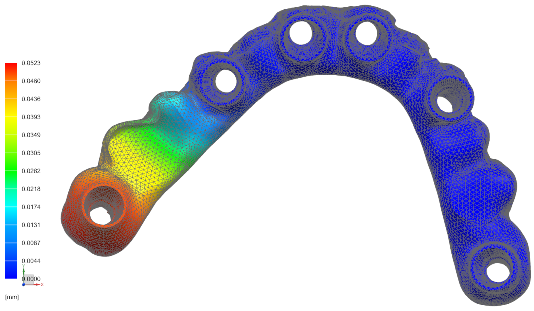

(a) Exaggerated displacement.

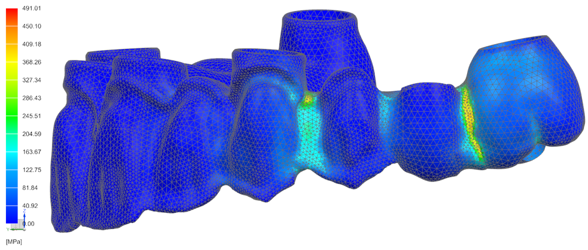

(b) Stress. Right view.

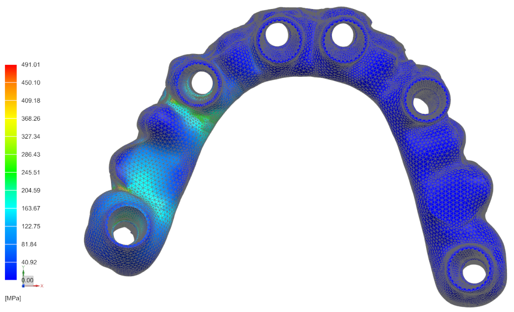

(c) Stress. Top view.

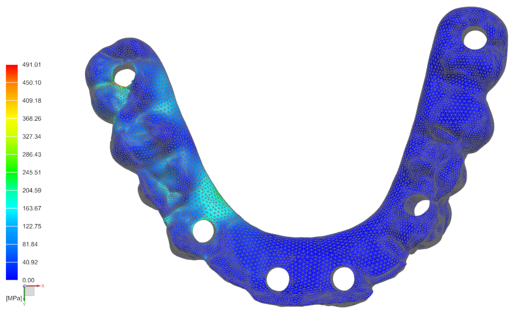

(d) Stress. Bottom view.

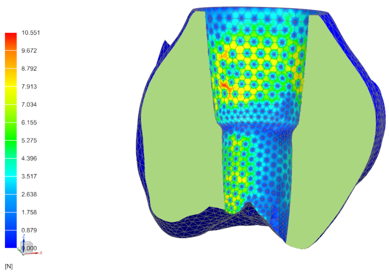

(e) Reaction forces. View inside the first access hole.

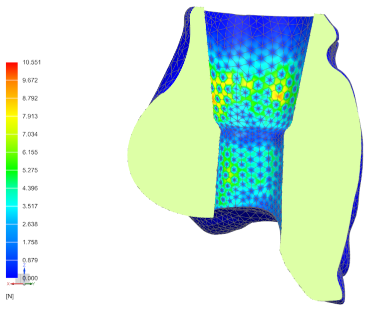

(f) Reaction forces. View inside the second access hole.

Figure 4.34.: 50 [μm] misfit in the binormal direction applied on the first access hole of an All-on-6 prosthesis.

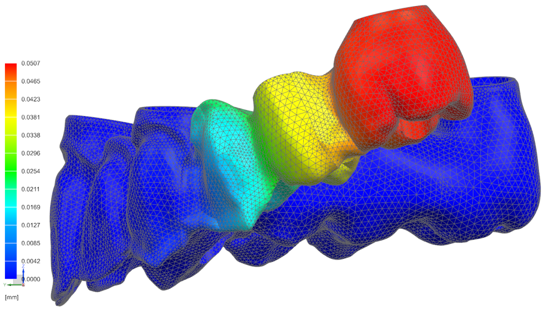

(a) Exaggerated displacement.

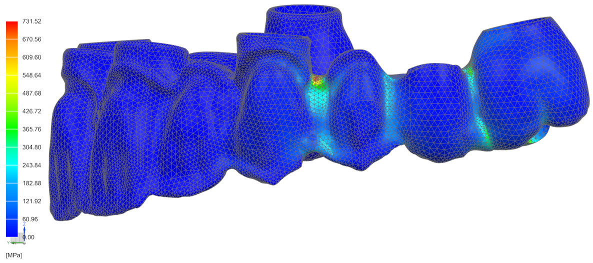

(b) Stress. Right view.

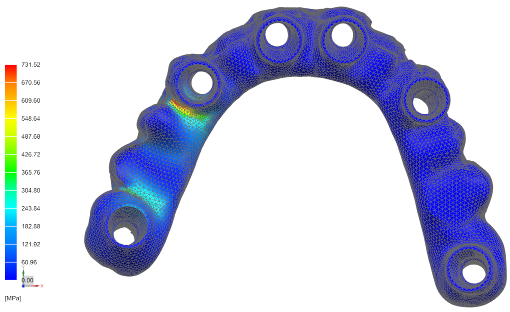

(c) Stress. Top view.

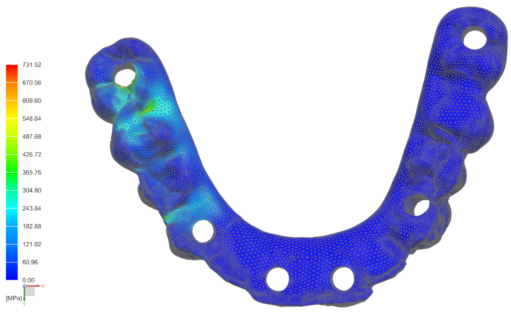

(d) Stress. Bottom view.

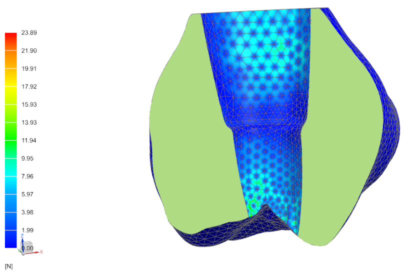

(e) Reaction forces. View inside the first access hole.

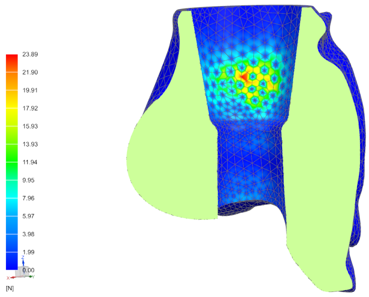

(f) Reaction forces. View inside the second access hole.

Figure 4.35.: 50 [μm] misfit in the normal direction applied on the first access hole of an All-on-6 prosthesis.

Second Access Hole Figures 4.36, 4.37 and 4.38 illustrates the displacement, stress constraints and reaction forces when applying a 50 [μm] misfit on the second access hole of an All-on-6 prosthesis. It can be seen that the stress constraints are mainly between in the first two inter-hole regions. The reaction forces are mainly inside the second and third access holes.

As shown in Figures 4.36b, 4.36c and 4.36d, the maximal stress is approximately 1600 [MPa] in the tangential direction.

In the binormal direction, the maximum stress is in the range 1000-1040 [MPa].

In the normal direction, the maximum stress is higher than when the misfit is applied in the tangent direction.

The most destructive direction is thus the normal.

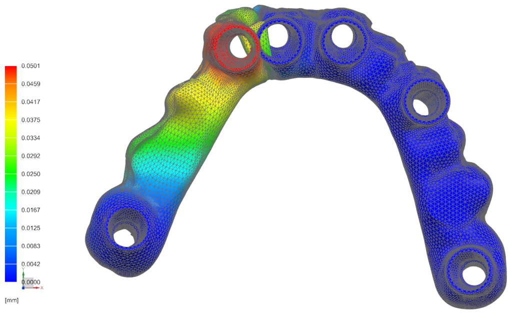

(a) Exaggerated displacement.

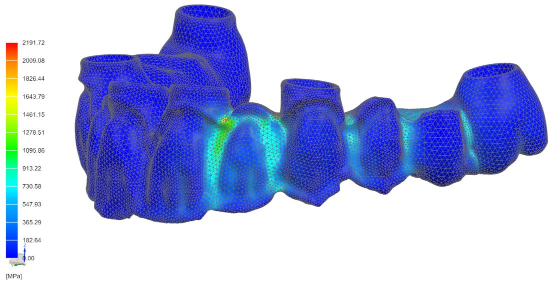

(b) Stress. Right view.

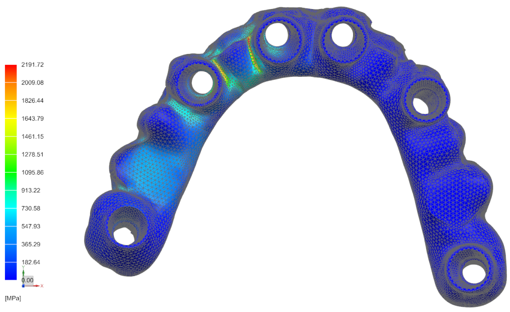

(c) Stress. Top view.

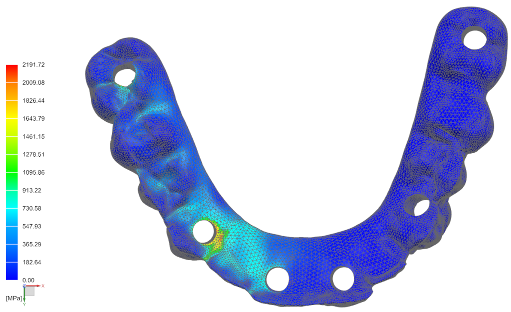

(d) Stress. Bottom view.

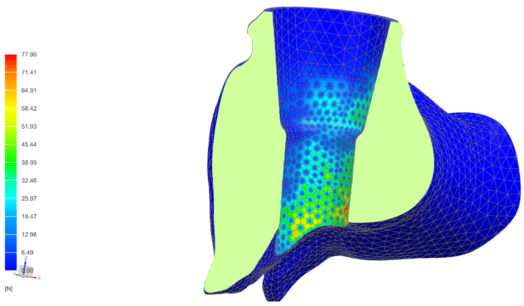

(e) Reaction forces. View inside the second access hole.

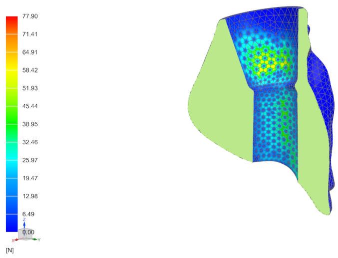

(f) Reaction forces. View inside the third access hole.

Figure 4.36.: 50 [μm] misfit in the tangent direction applied on the second access hole of an All-on-6 prosthesis.

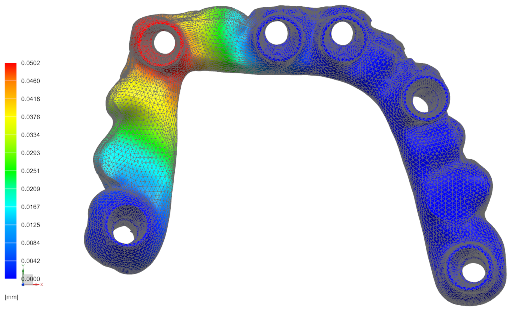

(a) Exaggerated displacement.

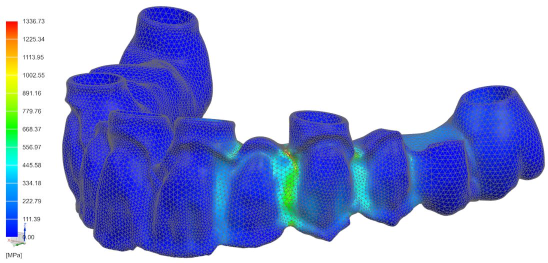

(b) Stress. Right view.

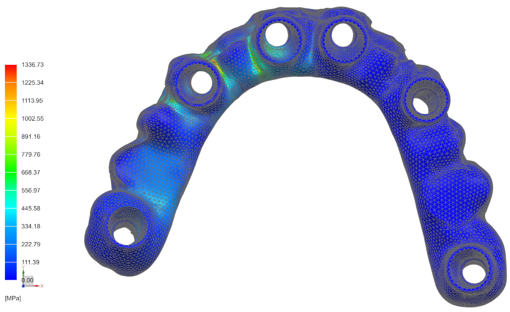

(c) Stress. Top view.

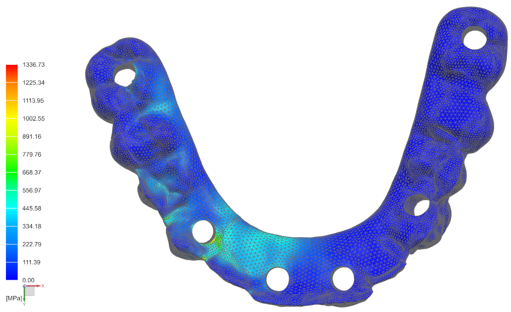

(d) Stress. Bottom view.

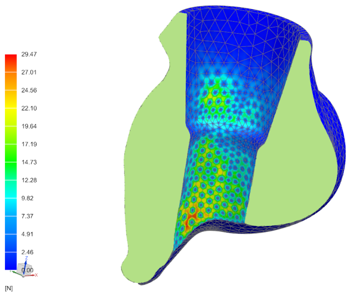

(e) Reaction forces. View inside the second access hole.

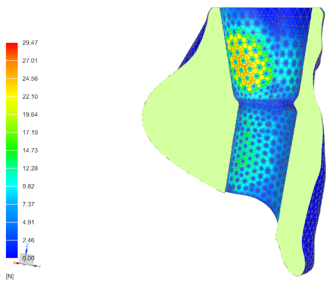

(f) Reaction forces. View inside the third access hole.

Figure 4.37.: 50 [μm] misfit in the binormal direction applied on the second access hole of an All-on-6 prosthesis.

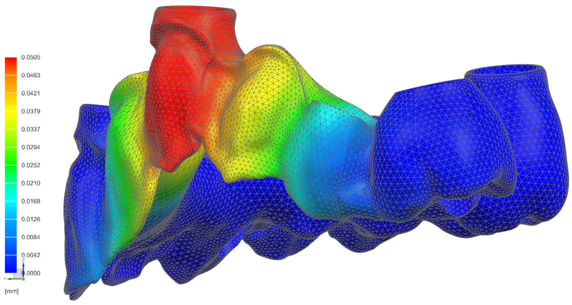

(a) Exaggerated displacement.

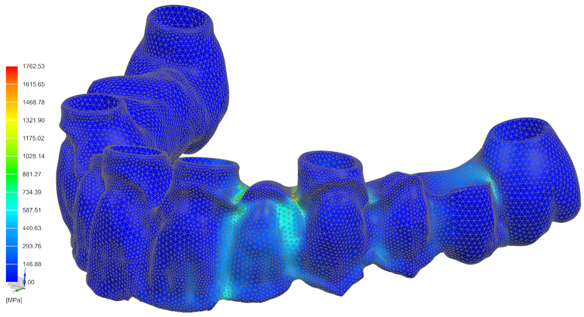

(b) Stress. Right view.

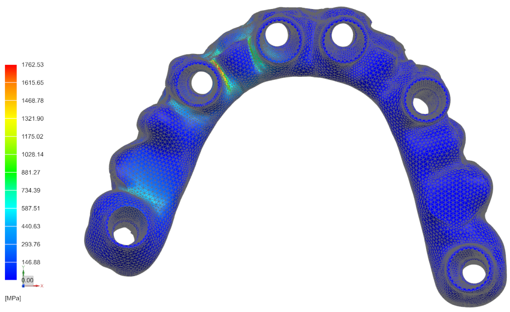

(c) Stress. Top view.

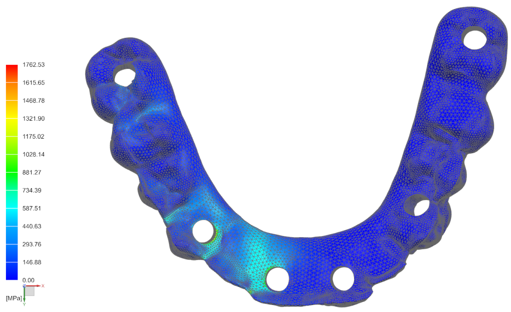

(d) Stress. Bottom view.

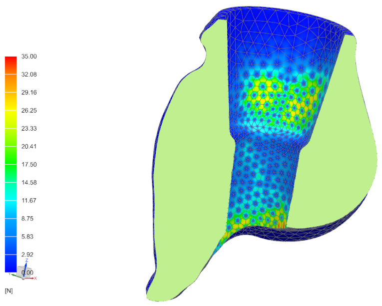

(e) Reaction forces. View inside the second access hole.

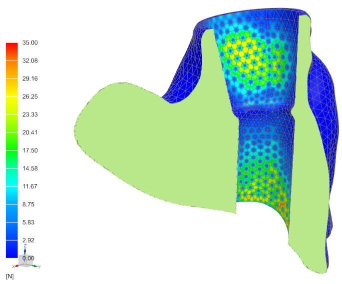

(f) Reaction forces. View inside the third access hole.

Figure 4.38.: 50 [μm] misfit in the normal direction applied on the second access hole of an All-on-6 prosthesis.

Third Access Hole As illustrated by Figures 4.39, 4.41 and 4.43, the stress constraints are mainly located in the second and third inter-hole regions. Concerning the reaction forces, as shown in Figures 4.40, 4.42 and 4.44, they are high in the second, third and fourth access holes.

In the tangent direction, the maximum stress is approximately 3300 [MPa]. Following the binormal, the maximum elemental stress is 1930 [MPa]. For the normal direction, it is 200 [MPa]. The most detrimental direction is again the tangent direction.

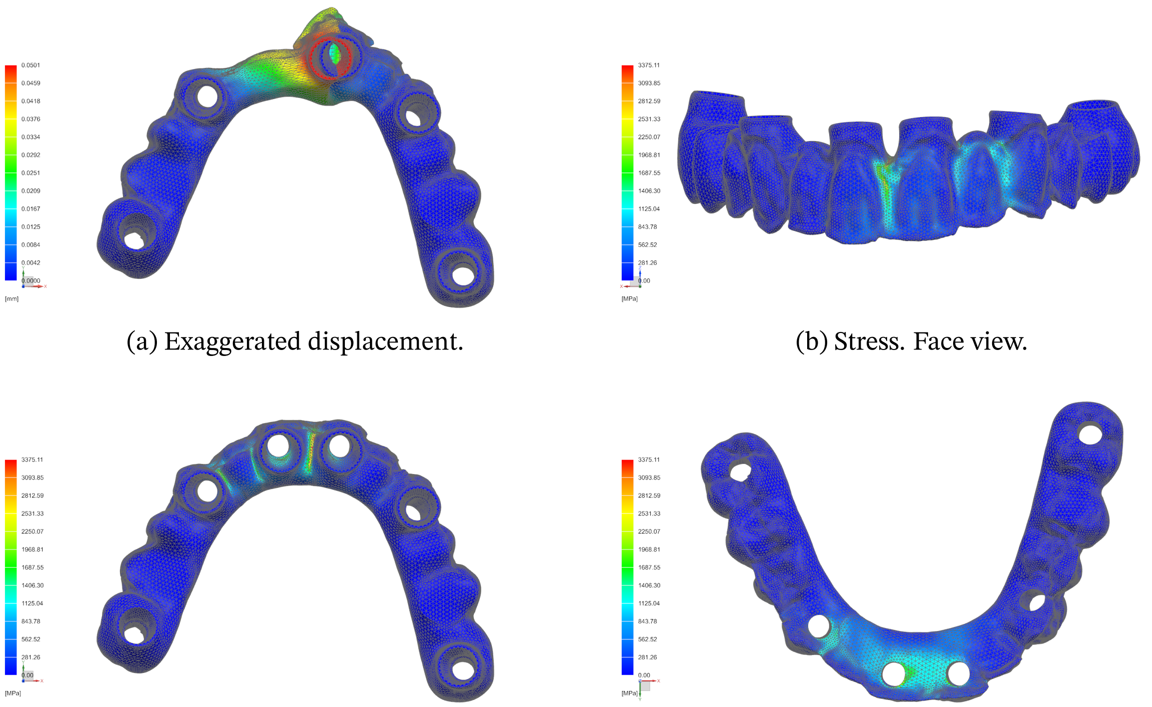

(a) Exaggerated displacement.

(b) Stress. Face view.

(c) Stress. Top view.

(d) Stress. Bottom view.

Figure 4.39.: Displacement and stress caused by a 50 [μm] misfit in the tangent direction applied on the third access hole of an All-on-6 prosthesis.

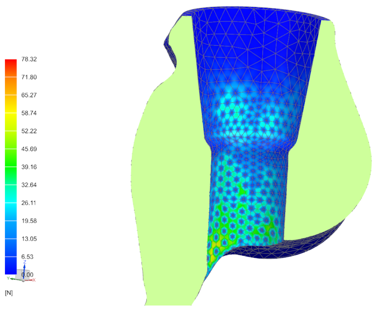

(a) Reaction forces on the second access hole.

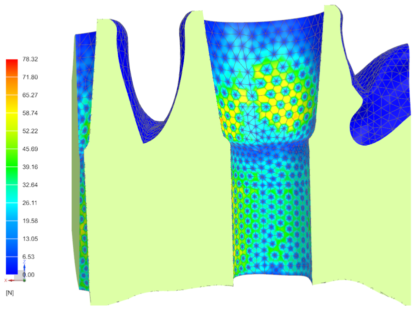

(b) Reaction forces on the third access hole.

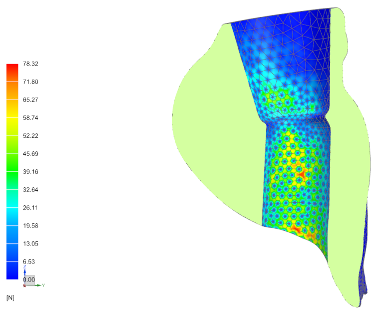

(c) Reaction forces on the fourth access hole.

Figure 4.40.: Reaction forces for an All-on-6 prosthesis with a 50 $[\mu m]$ misfit in the tangent direction applied on the third access hole.

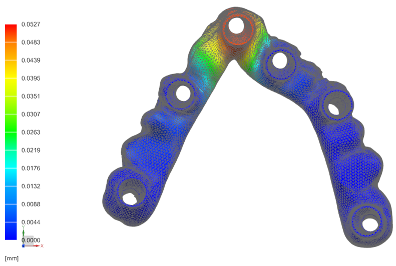

(a) Exaggerated displacement.

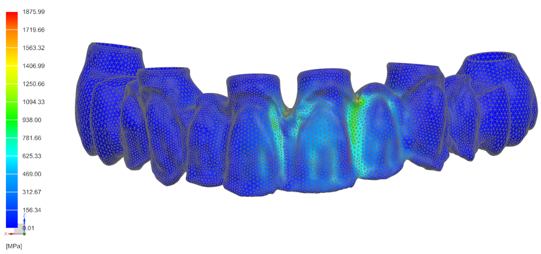

(b) Stress. Face view.

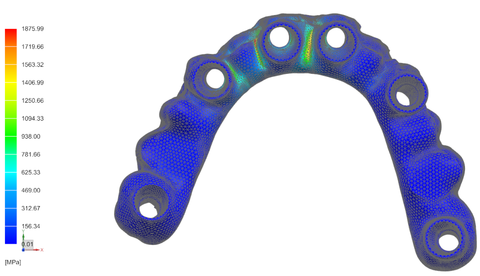

(c) Stress. Top view.

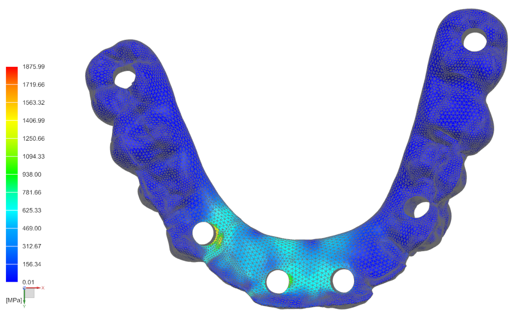

(d) Stress. Bottom view.

Figure 4.41.: Displacement and stress caused by a 50 $[\mu m]$ misfit in the binormal direction applied on the third access hole of an All-on-6 prosthesis.

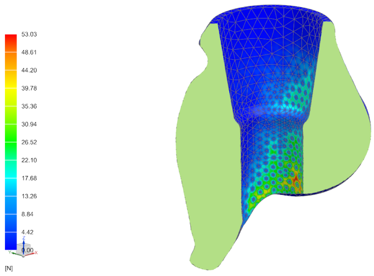

(a) Reaction forces on the second access hole.

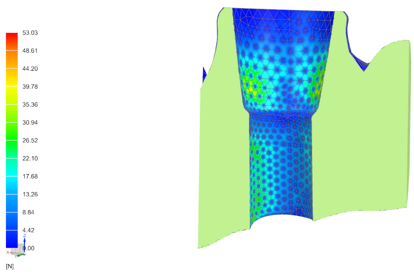

(b) Reaction forces on the third access hole.

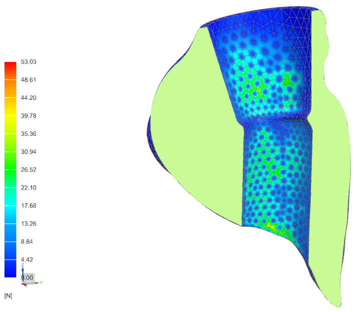

(c) Reaction forces on the fourth access hole.

Figure 4.42.: Reaction forces for an All-on-6 prosthesis with a 50 [μm] misfit in the binormal direction applied on the third access hole.

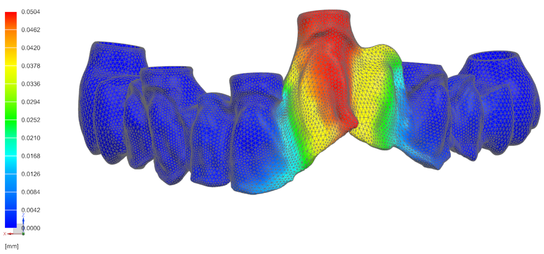

(a) Exaggerated displacement.

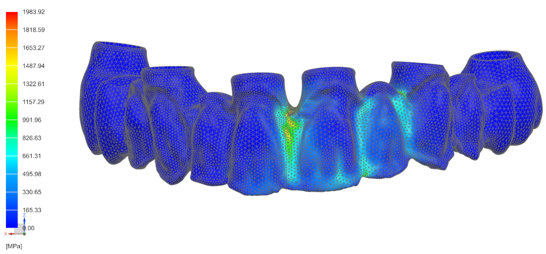

(b) Stress. Face view.

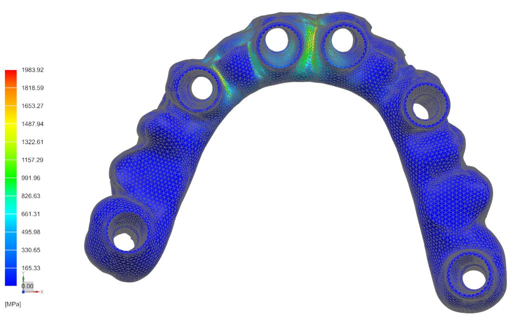

(c) Stress. Top view.

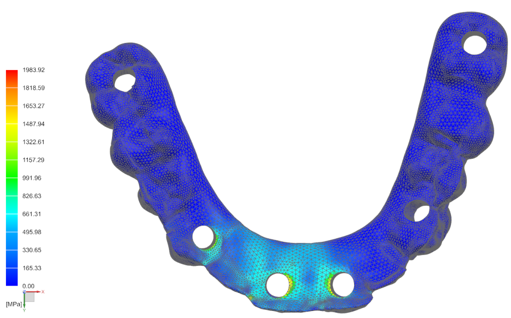

(d) Stress. Bottom view.

Figure 4.43.: Displacement and stress caused by a 50 [μm] misfit in the normal direction applied on the third access hole of an All-on-6 prosthesis.

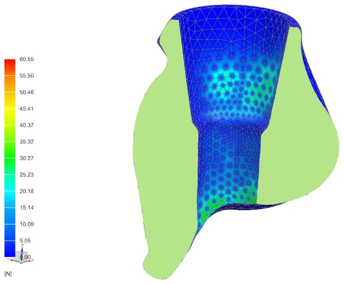

(a) Reaction forces on the second access hole.

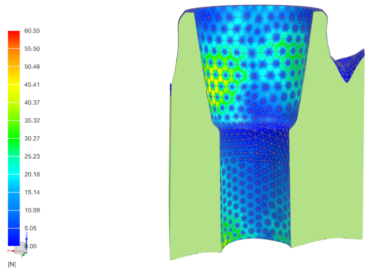

(b) Reaction forces on the third access hole.

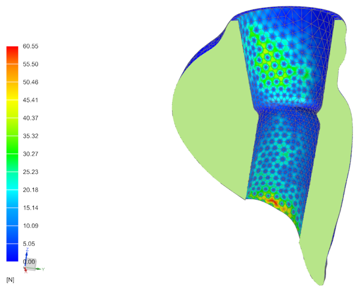

(c) Reaction forces on the fourth access hole.

Figure 4.44.: Reaction forces for an All-on-6 prosthesis with a 50 [μm] misfit in the normal direction applied on the third access hole.

Discussion For each implant analysed, the most damaging direction is the tangent, followed by the normal. The maximum stress values can be seen in Table 4.2. There is a huge difference between the different position of misfits.

Implant Position	Direction	Maximum Stress [MPa]
First	Tangent	1170
	Binormal	390
	Normal	780
Second	Tangent	1600
	Binormal	1040
	Normal	1730
Third	Tangent	3300
	Binormal	1930
	Normal	2000

Table 4.2.: Comparison of the maximum stress in the different configurations for the All-on-6 prosthesis.

All-on-4 Prosthesis

First Access Hole For the first access hole of the All-on-4 prosthesis, the displacement, stresses and reaction forces are shown in Figures 4.45, 4.46 and 4.47. The reaction forces are high in the two first access holes.

The stress in the tangential direction, illustrated in Figures 4.45b, 4.45c and 4.45d, show a maximum value of around 1190 [MPa]. In the binormal direction, this maximum is approximately 400 [MPa]. Finally, for the normal direction, it tends to 800 [MPa].

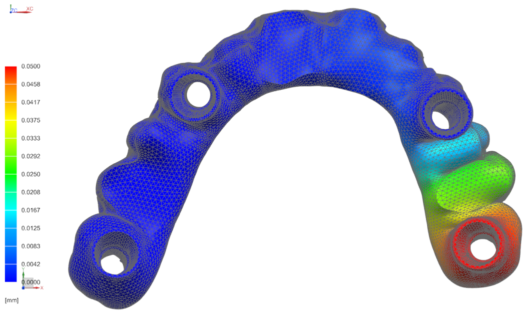

(a) Exaggerated displacement.

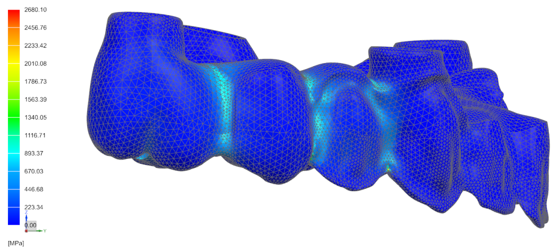

(b) Stress. Left view.

(c) Stress. Top view.

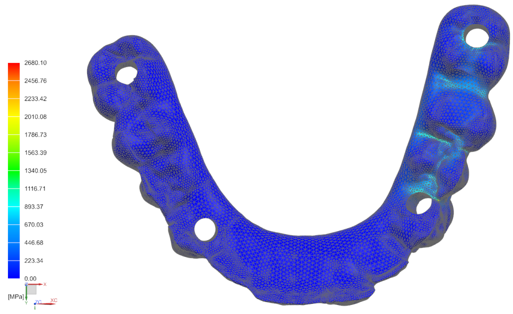

(d) Stress. Bottom view.

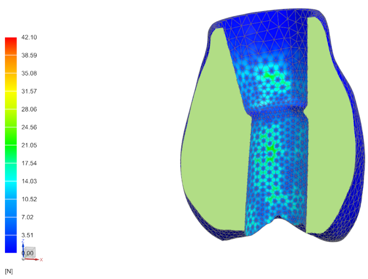

(e) Reaction forces. View inside the first access hole.

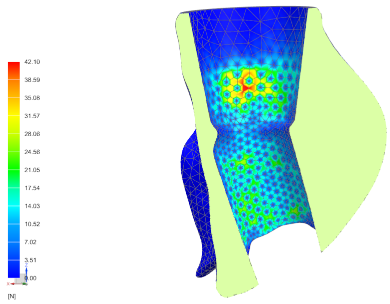

(f) Reaction forces. View inside the second access hole.

Figure 4.45.: 50 [μm] misfit in the tangent direction applied on the first access hole of an All-on-4 prosthesis.

(a) Exaggerated displacement.

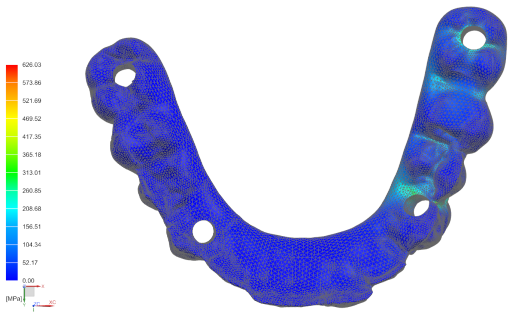

(b) Stress. Left view.

(c) Stress. Top view.

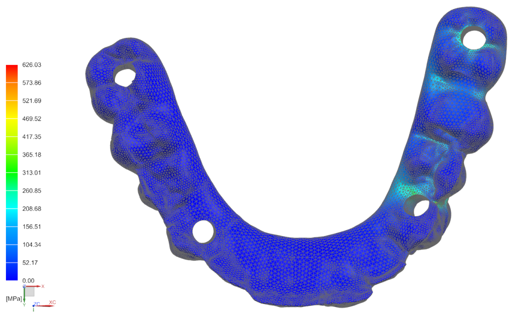

(d) Stress. Bottom view.

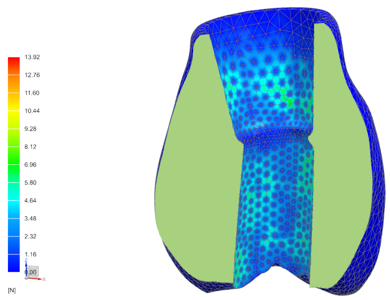

(e) Reaction forces. View inside the first access hole.

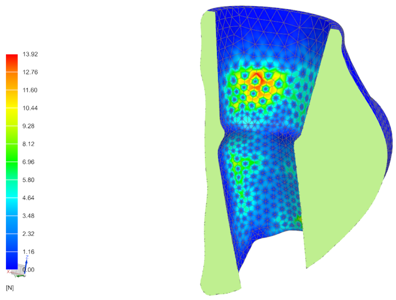

(f) Reaction forces. View inside the second access hole.

Figure 4.46.: 50 [μm] misfit in the binormal direction applied on the first access hole of an All-on-4 prosthesis.

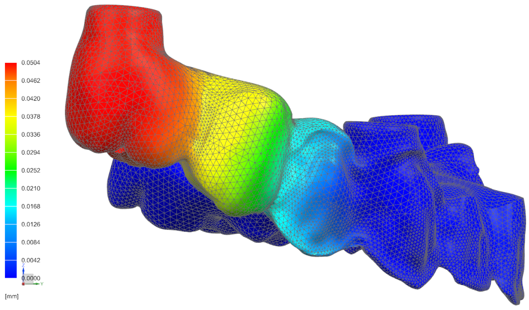

(a) Exaggerated displacement.

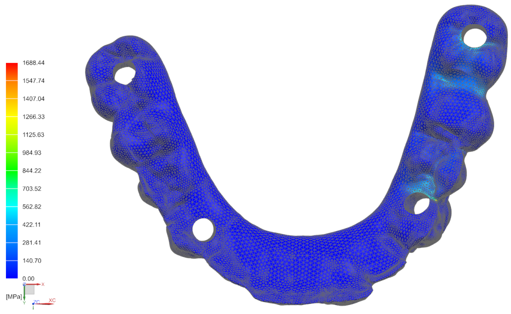

(b) Stress. Left view.

(c) Stress. Top view.

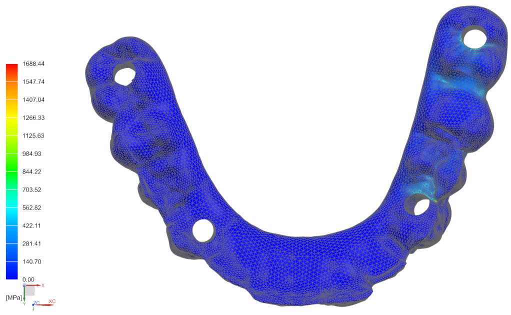

(d) Stress. Bottom view.

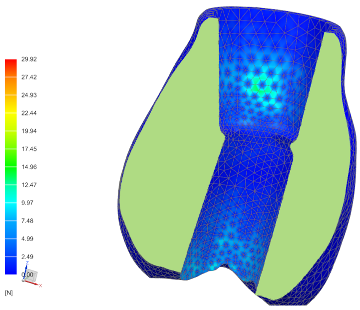

(e) Reaction forces. View inside the first access hole.

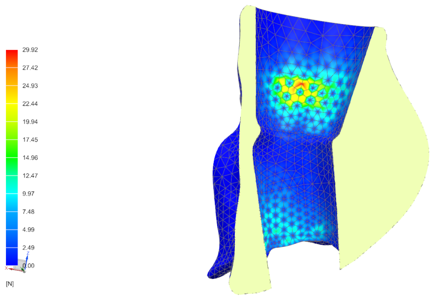

(f) Reaction forces. View inside the second access hole.

Figure 4.47.: 50 [μm] misfit in the normal direction applied on the first access hole of an All-on-4 prosthesis.

Second Access Hole The displacement, stress and reaction forces when a 50 [μm] misfit is applied to the second access hole are shown in Figures 4.48, 4.49, 4.50 and 4.51. Concerning the reaction forces, they are mainly located in the first two access holes. The maximum stress is 1100 [MPa] in the tangent direction, 800 [MPa] in the binormal and 750 [MPa] when the misfit is in the normal direction.

For this configuration, the least detrimental direction is the normal and the most damaging one is the tangent.

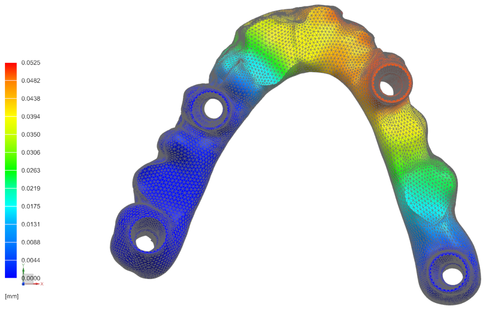

(a) Exaggerated displacement.

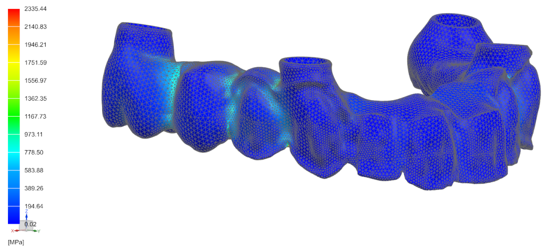

(b) Stress. Left view.

(c) Stress. Top view.

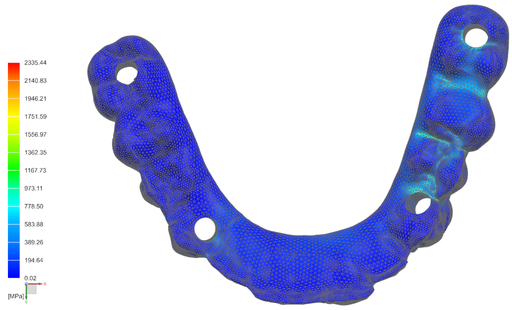

(d) Stress. Bottom view.

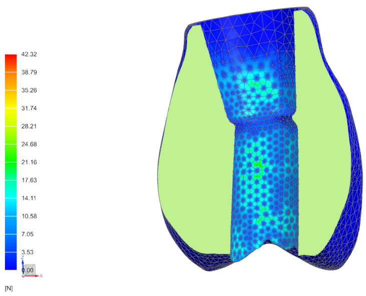

(e) Reaction forces. View inside the first access hole.

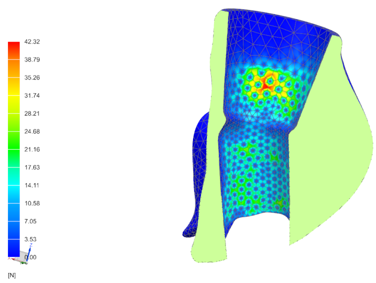

(f) Reaction forces. View inside the second access hole.

Figure 4.48.: 50 [μm] misfit in the tangent direction applied on the second access hole of an All-on-4 prosthesis.

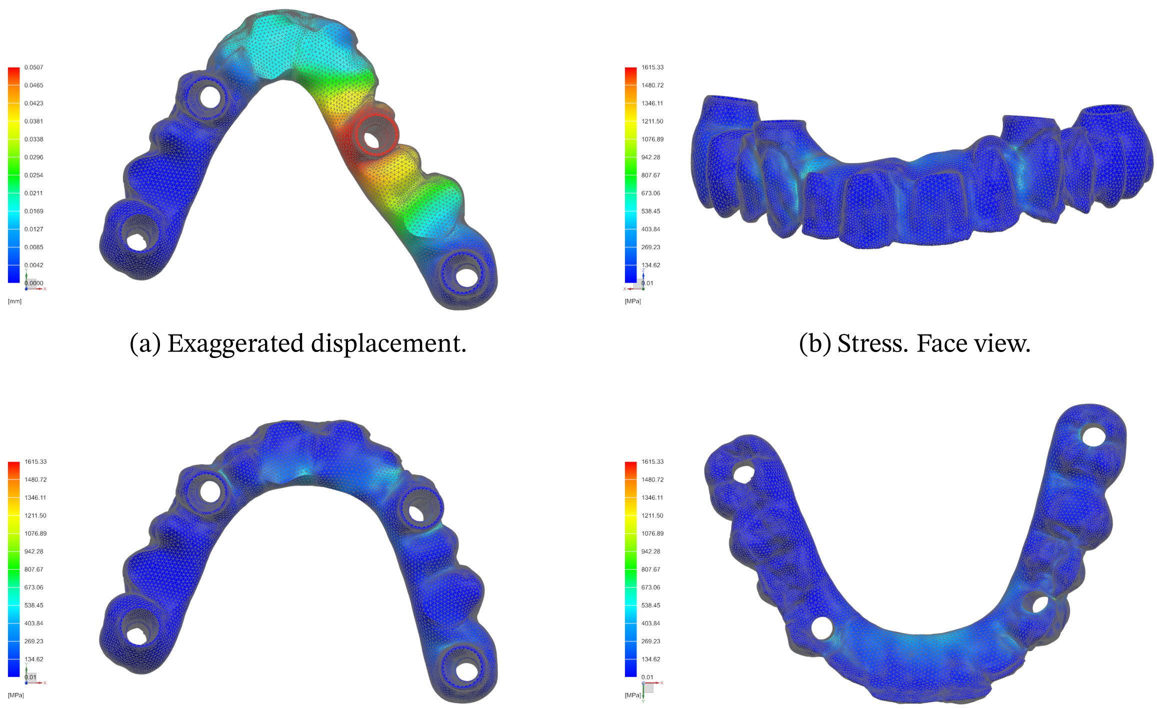

(a) Exaggerated displacement.

(b) Stress. Face view.

(c) Stress. Top view.

(d) Stress. Bottom view.

Figure 4.49.: Displacement and stress caused by a 50 [μm] misfit in the binormal direction applied on the second access hole of an All-on-4 prosthesis.

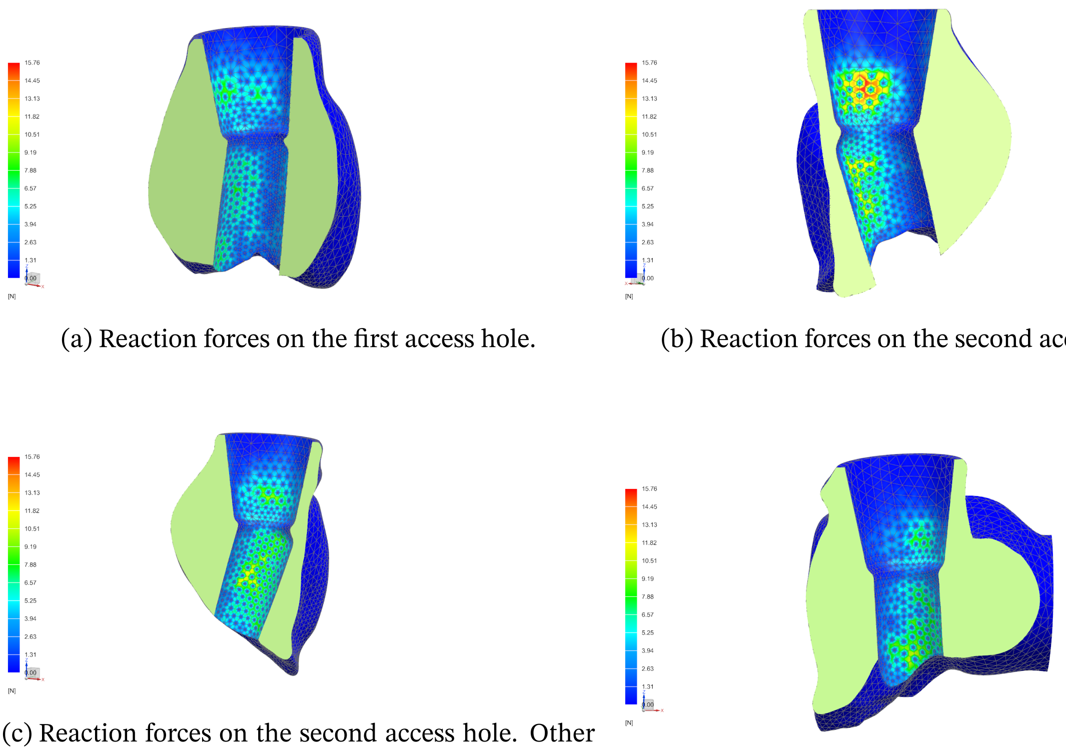

(a) Reaction forces on the first access hole.

(b) Reaction forces on the second access hole.

(c) Reaction forces on the second access hole. Other view.

(d) Reaction forces on the third access hole.

Figure 4.50.: Reaction forces for an All-on-4 prosthesis with a 50 [μm] misfit in the binormal direction applied on the second access hole.

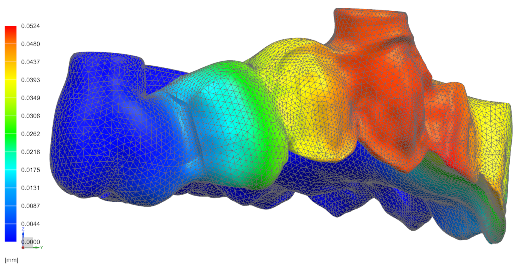

(a) Exaggerated displacement.

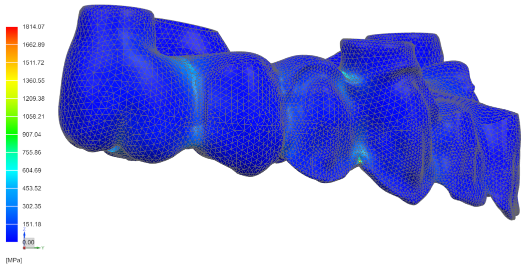

(b) Stress. Left view.

(c) Stress. Top view.

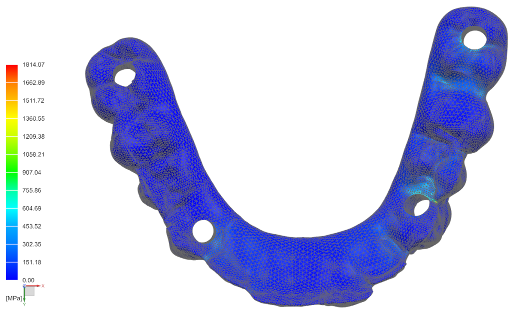

(d) Stress. Bottom view.

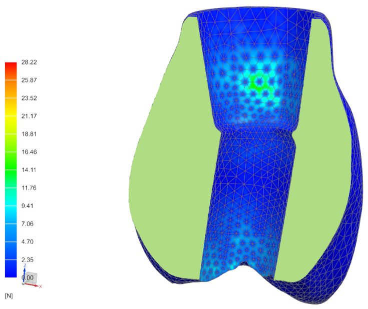

(e) Reaction forces. View inside the first access hole.

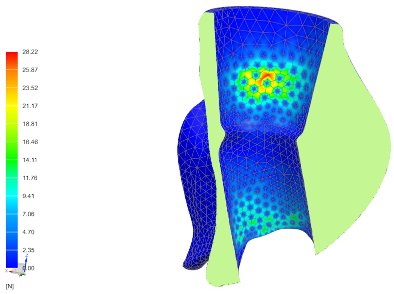

(f) Reaction forces. View inside the second access hole.

Figure 4.51.: 50 [μm] misfit in the normal direction applied on the second access hole of an All-on-4 prosthesis.

Discussion As for the two other prostheses, the most detrimental direction is the tangent. For the first implant, the binormal direction is the least damaging to apply a misfit. For the second access hole, the normal and the binormal give maximum stresses in the same range.

Implant Position	Direction	Maximum Stress [MPa]
First	Tangent	1190
	Binormal	400
	Normal	800
Second	Tangent	1100
	Binormal	800
	Normal	750

Table 4.3.: Comparison of the maximum stress in the different configurations for the All-on-4 prosthesis.

4.4.2. Zirconia Cases

Now that the different titanium cases have been assessed, the zirconia frameworks are simulated. The figures for the Zirconia are in Appendices A.1, A.2 and A.3. The results for the zirconia should be higher than for the titanium. Indeed, when two materials are subjected to the same deformation, the material with the higher Young's modulus experiences greater stress. Young's modulus measures the stiffness of a material. It quantifies the relationship between tensile or compressive stress σ and axial strain ε in the linear elastic region of a material:

$$E = \frac{\sigma}{\varepsilon} \tag{4.2}$$

If two materials undergo the same amount of strain, the stress in each material is directly proportional to its Young's modulus. Therefore, a material with a higher Young's modulus will generate more stress compared to a material with a lower Young's modulus when subjected to the same deformation. The stresses found for the zirconia frameworks should be $\frac{210}{121} \approx 1.73$ times bigger than those found for the titanium. Tables 4.4, 4.5 and 4.6 present the maximum stress values found for the different configurations.

When comparing the different tables of maximum stresses, this hypothesis is verified.

Implant Position	Direction	Maximum Stress [MPa]
First	Tangent	4460
	Binormal	1910
	Normal	2800
Second	Tangent	4600
	Binormal	2050
	Normal	3000
Third	Tangent	3430
	Binormal	2020
	Normal	2800
Fourth	Tangent	6000
	Binormal	3255
	Normal	3570

Table 4.4.: Comparison of the maximum stress in the different configurations for the All-on-8 prosthesis in zirconia.

Implant Position	Direction	Maximum Stress [MPa]
First	Tangent	2030
	Binormal	670
	Normal	1350
Second	Tangent	2800
	Binormal	1800
	Normal	3000
Third	Tangent	5720
	Binormal	3340
	Normal	3460

Table 4.5.: Comparison of the maximum stress in the different configurations for the All-on-6 prosthesis.

Implant Position	Direction	Maximum Stress [MPa]
First	Tangent	2060
	Binormal	700
	Normal	1380
Second	Tangent	1910
	Binormal	1370
	Normal	1300

Table 4.6.: Comparison of the maximum stress in the different configurations for the All-on-4 prosthesis.

4.4.3. Comparison between the two Materials

In this subsection, the Titanium and the Zirconia cases are compared.

To determine whether the prosthesis breaks or undergoes plastification (yielding), it is essential to compare the stress values resulting from the deformation with the yield strength, σ_y, and the ultimate tensile strength, UTS. As a reminder, yield strength is the stress at which the material begins to deform plastically. If the calculated stress exceeds the yield strength, the material plastically deforms. If the stress exceeds the ultimate tensile strength of the material, then it breaks. Zirconia does not exhibit a plastic region and thus immediately breaks because its yield strength is the same value as its ultimate tensile strength. The comparison of maximum stress, yield strength and ultimate tensile strength for the two materials in different implant positions and directions for the three types of prostheses is made in Table 4.7. The configurations that breaks are highlighted in red, and the ones that do not are in green. It can be concluded that for a misfit of 50 [μm], most of the configurations are damaging for the prostheses. There are more configurations that do not break for the titanium than for the zirconia. It is logical because the titanium exhibits less stress for the same imposed displacement than zirconia due to the difference in Young's moduli as explained above. Even though the zirconia has an elastic modulus nearly twice as big as the titanium, its ultimate tensile strength is close to the one of titanium. It is thus logical that it breaks for more configurations.

Prosthesis Type	Implant Position	Direction	Titanium			Zirconia	
			Maximum Stress [MPa]	σ_y [MPa]	UTS [MPa]	Maximum Stress [MPa]	σ_y UTS [MPa]
All-on-8	1	Tangent	2580	805	845	4460	850
		Binormal	1100	805	845	1910	850
		Normal	1620	805	845	2800	850
	2	Tangent	2660	805	845	4600	850
		Binormal	1200	805	845	2050	850
		Normal	1740	805	845	3000	850
	3	Tangent	1980	805	845	3430	850
		Binormal	1150	805	845	2020	850
		Normal	1620	805	845	2800	850
	4	Tangent	3500	805	845	6000	850
		Binormal	1880	805	845	3255	850
		Normal	2050	805	845	3570	850
All-on-6	1	Tangent	1170	805	845	2030	850
		Binormal	390	805	845	670	850
		Normal	780	805	845	1350	850
	2	Tangent	1600	805	845	2800	850
		Binormal	1040	805	845	1800	850
		Normal	1730	805	845	3000	850
	3	Tangent	3300	805	845	5720	850
		Binormal	1930	805	845	3340	850
		Normal	2000	805	845	3460	850
All-on-4	1	Tangent	1190	805	845	2060	850
		Binormal	400	805	845	700	850
		Normal	800	805	845	1380	850
	2	Tangent	1100	805	845	1910	850
		Binormal	800	805	845	1370	850
		Normal	750	805	845	1300	850

Table 4.7.: Comparison of Maximum Stress, Yield Strength, and Ultimate Tensile Strength for Titanium and Zirconia Prostheses in Different Implant Positions and Directions for the three types of protheses.

4.4.4. Impact of the Number of Implants

As mentioned in Chapter 2, the number of implants has an impact on the prothesis when a misfit is applied. The more access holes there are, the higher the maximum stress is. To be able to compare the stress for the three prosthesis, it is important to keep in mind that the second access hole of an All-on-6 prosthesis corresponds to the third access hole of an All-on-8 prothesis. The second access hole of an All-on-4 prosthesis is the third access hole of an All-on-8 overdenture. Table 4.8 presents a comparison of the maximum stress values for the three types of prostheses in different implant positions and directions for the titanium cases.

The All-on-8 configuration evolves more access holes, which may lead to higher cumulative stresses, especially if the load is not well distributed, particularly if there are misalignments or misfits. The table shows higher stress values for the All-on-8 prosthesis in every configuration.

One important thing to note on the table if that, for the first implant, the All-on-4 prosthesis presents higher stress values than the All-on-6. Since the prosthesis has fewer access holes, this means that each implant bears a larger portion of the load. It might be linked to its position and the lever effect.

All-on-8			All-on-6		All-on-4	
Implant Position	Direction	Maximum Stress [MPa]	Equivalent Position	Maximum Stress [MPa]	Equivalent Position	Maximum Stress [MPa]
1	Tangent	2580	1	1170	1	1190
	Binormal	1100		390		400
	Normal	1620		780		800
2	Tangent	2660	/	/	/	/
	Binormal	1200		/		/
	Normal	1740		/		/
3	Tangent	1980	2	1600	2	1100
	Binormal	1150		1040		800
	Normal	1620		1730		750
4	Tangent	3500	3	3300	/	/
	Binormal	1880		1930		/
	Normal	2050		2000		/

Table 4.8.: Maximum Stress Comparison of All-on-8, All-on-6, and All-on-4 Prostheses in Different Implant Positions and Directions.

4.4.5. Stiffness of the Prosthesis

It is essential to determine the stiffness of the prostheses when undergoing different loads. If the stiffness of the prosthesis is greater than that of the bone or an implant, it could cause problems, as explained in the previous sections. The stiffness values of the different prosthesis are presented in Table 4.9. To determine these values, the reaction forces components are extracted for each node. Then, the values for each component are summed. Once, this step is done for each component, the magnitude in the direction of the applied displacement is found. Finally, the stiffness is found. These steps are described in Equations 4.3, 4.4 and 4.5.

$$F_j = \sum_{i=1}^{\text{Number of nodes}} F_{j,i} \qquad \text{for } j = x, y, \text{ or } z \tag{4.3}$$

$$F = \sqrt{F_x^2 + F_y^2 + F_z^2} \tag{4.4}$$

$$k = \frac{F}{x} = \frac{F}{50} [N/\mu m] \tag{4.5}$$

For every type of prosthesis, it is stiffer when the misfit is applied in the tangent direction. As expected, the zirconia prostheses are stiffer than the titanium ones. Once again, the Young's modulus of the titanium is lower than the one of the zirconia. A material with a higher elastic modulus is stiffer and deforms less under a given load. Furthermore, zirconia being stiffer, it resists deformation more, leading to a greater apparent stiffness.

			Titanium	Zirconia
Prosthesis Type	Implant Position	Direction	Stiffness [N/μm]	Stiffness [N/μm]
All-on-8	1	Tangent	655.46	1117.39
		Binormal	149.51	278.59
		Normal	214.04	384.81
	2	Tangent	1,020.89	1753.1
		Binormal	253.95	463.71
		Normal	322.14	572.82
	3	Tangent	789.31	1353.43
		Binormal	203.66	362.44
		Normal	199.22	349.47
	4	Tangent	948.61	1608.11
		Binormal	347.48	665.98
		Normal	371.70	667.2
All-on-6	1	Tangent	203.43	453.96
		Binormal	25.92	69.32
		Normal	42.76	50.17
	2	Tangent	202.59	449.03
		Binormal	27.09	66.46
		Normal	43.10	51.43
	3	Tangent	1,007.83	1265.76
		Binormal	410.18	620.38
		Normal	394.04	667
All-on-4	1	Tangent	266.09	453.95
		Binormal	19.92	68.70
		Normal	28.99	50.06
	2	Tangent	282.11	474.47
		Binormal	75.49	168.3
		Normal	31.71	54.65

Table 4.9.: Stiffness values of titanium and zirconia for different prosthesis types, implant positions, and directions when a misfit of 50 μm is applied.

4.4.6. Stiffness of the Implant

As explained earlier, it is crucial that the stiffness of the prosthesis does not exceed the stiffness of the bone or the implant. Due to the lack of information on the stiffness of dental implant, its value is not available. However, it can be approximated by considering the implant as a cylinder in Ti-6Al-4V. The stiffness of an implant can be calculated as such,

$$k_{implant} = \frac{E \times \pi \times d^2}{4L}, \tag{4.6}$$

where E is the Young's modulus of the implant, d its diameter and L its length. This thus gives a stiffness of

$$k_{implant} = \frac{121[GPa] \times \pi \times (4.3[mm])^2}{4 \times 13[mm]} \approx 129.2[N/\mu m]. \tag{4.7}$$

The stiffness of the prosthesis is higher than that of the implant for most of the configurations. This could thus lead to implant fracture.

4.4.7. Stiffness of the Bone

Once again, there is not enough data available on the stiffness of the maxillary bone. This is thus approximated. To determine the stiffness of the bone, Equation 4.8 is used. In this equation, E_{bone} is the Young's modulus of the bone, L_{bone} the length of the bone and A_{bone} its cross-sectional area. The first hypothesis made is that the bone is isotropic, thus a unique Young's modulus is taken.

$$k_{bone} = \frac{E_{bone} A_{bone}}{L_{bone}} \tag{4.8}$$

Another hypothesis that can be made is that the length of the bone is approximately the same length as the prosthesis. This is considered reasonable as the prosthesis is designed to match the dimensions of the maxilla for effective dental restoration. By rearranging Equation 4.8 and comparing it to the equivalent equation for the prosthesis, Equation 4.9.

$$\frac{E_{bone} A_{bone}}{k_{bone}} = \frac{E_{prosthesis} A_{prosthesis}}{k_{prosthesis}} \tag{4.9}$$

It can be rewritten as Equation 4.10.

$$k_{bone} = \frac{E_{bone} A_{bone} k_{prosthesis}}{E_{prosthesis} A_{prosthesis}} \tag{4.10}$$

In the above equation, all variables are known and have been presented, except the two cross-sectional areas. For the prosthesis, its cross-section is found using *Siemens NX1859*. A cut is made in the molar area and the *Measure* tool of the software is used. The cross-sectional area is approximately 39.3 $[mm^2]$. For the maxillary bone, the cross-section area in the molar region is approximated. A hypothesis that is made is that the bone is elliptical. As mentioned in Chapter 2, the stiffness of the bone for the studied configurations is unknown, but the dimensions are known. Thus, the cross-sectional are approximated using Equation 4.11. In this equation, a is the length of the semi-major axis, and b of the semi-minor axis.

$$A_{bone} = \pi ab = \pi \times 8 \times 7.55[mm^2] \approx 189.8[mm^2] \tag{4.11}$$

Now that all the variables are known, it is possible to determine the stiffness of the bone in the different configurations. These results are presented in Table 4.10.

The stiffness of the bone is known for the different configurations. It is thus possible to determine the ratio of stiffnesses and thus the displacement that is applied to the bone. When the prosthesis is in titanium, the ratio of stiffnesses tends to 1.7 and when it is in zirconia, it is approximately 2.9. This ratio is inversely proportional to the ratio of displacements. The forces acting on the prosthesis are the same as those acting on the bone. Equation 4.12 states the Hooke's law governing the bone. In this equation, x_{bone} is the displacement of the bone.

$$F_{bone} = k_{bone} x_{bone} \tag{4.12}$$

$$\begin{aligned} F_{bone} &= F_{prosthesis} & (4.13)\\ k_{bone} x_{bone} &= k_{prosthesis} x_{prosthesis} & (4.14)\\ \frac{x_{bone}}{x_{prosthesis}} &= \frac{k_{prosthesis}}{k_{bone}} & (4.15)\\ x_{bone} &= \frac{k_{prosthesis} x_{prosthesis}}{k_{bone}} & (4.16) \end{aligned}$$

When applying a 50 [μm] misfit to the prosthesis, the displacement for the bone when it is in Ti-6Al-4V is approximately 83.5 [μm]. For the zirconia, it tends to 144.9 [μm].

4.4.8. Total Displacement

Since the problem is linear and the stress induced by a 50 [μ m] misfit is known, it is possible to determine the displacement that has to be applied to obtain a stress equal to the yield strength of each material. Specifically, for each material (the prosthesis and the bone), the displacement corresponding to the yield strength can be calculated using the relationship between stress and displacement.

Given that the force F is the same for both the bone and the prosthesis, the displacement at the bone will be greater than at the prosthesis because the stiffness of the bone (k_{bone}) is smaller than the stiffness of the prosthesis ($k_{prosthesis}$). This relationship can be expressed as:

$$\Delta_{bone} = \frac{k_{prosthesis}}{k_{bone}} \Delta_{prosthesis} \tag{4.17}$$

where Δ represents the displacement.

Once this displacement is known, and since the ratio of stiffness was determined in Section 4.4.8, the displacement at the bone level can be determined by multiplying the displacement of the prosthesis by the stiffness ratio:

$$\text{Stiffness Ratio} = \frac{k_{prosthesis}}{k_{bone}} \tag{4.18}$$

Finally, by summing the two displacements that can be reached before the prosthesis plasticizes (if in titanium) or breaks, the total misfit of the system is found. This means adding the displacement that causes the prosthesis to reach its yield strength and the displacement that causes the bone to reach its yield strength:

$$\Delta_{total} = \Delta_{prosthesis} + \Delta_{bone}. \tag{4.19}$$

			Titanium		Zirconia	
Prosthesis Type	Implant Position	Direction	Stiffness [N/μm]	Bone Stiffness [N/μm]	Stiffness [N/μm]	Bone Stiffness [N/μm]
All-on-8	1	Tangent	655.46	392.42	1117.39	385.46
		Binormal	149.51	89.51	278.59	96.10
		Normal	214.04	128.15	384.81	132.75
	2	Tangent	1,020.89	611.21	1753.1	604.76
		Binormal	253.95	152.04	463.71	159.96
		Normal	322.14	192.86	572.82	197.60
	3	Tangent	789.31	472.56	1353.43	466.89
		Binormal	203.66	121.93	362.44	125.03
		Normal	199.22	119.27	349.47	120.56
	4	Tangent	948.61	567.93	1608.11	554.74
		Binormal	347.48	208.03	665.98	229.74
		Normal	371.70	222.53	667.2	230.16
All-on-6	1	Tangent	203.43	121.80	453.96	156.60
		Binormal	25.92	15.52	69.32	23.91
		Normal	42.76	25.60	50.17	17.31
	2	Tangent	202.59	121.29	449.03	154.90
		Binormal	27.09	16.22	66.46	22.93
		Normal	43.10	25.80	51.43	17.74
	3	Tangent	1,007.83	603.39	1265.76	436.64
		Binormal	410.18	245.57	620.38	214.01
		Normal	394.04	235.91	667	230.09
All-on-4	1	Tangent	266.09	159.31	453.95	156.60
		Binormal	19.92	11.93	68.70	23.70
		Normal	28.99	17.35	50.06	17.27
	2	Tangent	282.11	168.90	474.47	163.68
		Binormal	75.49	45.20	168.3	58.06
		Normal	31.71	18.98	54.65	18.85

Table 4.10.: Bone stiffness values for the different configurations when a misfit of 50 μm is applied.

The different displacements are presented in Tables 4.11 and 4.12. The greater the total acceptable misfit, the greater the configuration is. If the prosthesis is made of titanium, a larger misfit can be tolerated before it plastifies because titanium exhibits significantly lower internal stresses compared to zirconia. Because of these greater stress concentrations and because the ultimate tensile strength (UTS) of both materials are nearly identical, zirconia fractures at smaller displacement than titanium. As mentioned in Section 2.5, the mean error with plaster impressions is approximately 24.6 [μm]. For photogrammetry, it is 87.6 [μm] and for intraoral scanners, 137.2 [μm]. For titanium, since the tolerable misfit for every prosthesis is higher than the mean error with plaster impressions, it is acceptable to keep using this technique. Photogrammetry mean error exceeds the tolerable misfit for most of the configurations, and only four configurations allow a misfit higher than the mean error for intraoral scanners. It is thus imperative to use plaster or to find solutions to increase the accuracy of other types of impressions. Nearly the same conclusions are drawn for the zirconia framework, except that using a intraoral scanner is not a viable option at all.

			Titanium				Bone	Total
Prosthesis Type	Implant Position	Direction	Misfit [μm]	Maximum Stress [MPa]	UTS [MPa]	Misfit if UTS [μm]	Misfit [μm]	Misfit [μm]
All-on-8	1	Tangent	50	2580	805	15.60	26.52	42.12
		Binormal	50	1100	805	36.59	62.20	98.80
		Normal	50	1620	805	24.85	42.24	67.08
	2	Tangent	50	2660	805	15.13	25.72	40.86
		Binormal	50	1200	805	33.54	57.02	90.56
		Normal	50	1740	805	23.13	39.32	62.46
	3	Tangent	50	1980	805	20.33	34.56	54.89
		Binormal	50	1150	805	35.00	59.50	94.50
		Normal	50	1620	805	24.85	42.24	67.08
	4	Tangent	50	3500	805	11.50	19.55	31.05
		Binormal	50	1880	805	21.41	36.40	57.81
		Normal	50	2050	805	19.63	33.38	53.01
All-on-6	1	Tangent	50	1170	805	34.40	58.48	92.88
		Binormal	50	390	805	103.21	175.45	278.65
		Normal	50	780	805	51.60	87.72	139.33
	2	Tangent	50	1600	805	25.16	42.77	67.92
		Binormal	50	1040	805	38.70	65.79	104.50
		Normal	50	1730	805	23.27	39.55	62.82
	3	Tangent	50	3300	805	12.20	20.73	32.93
		Binormal	50	1930	805	20.85	35.45	56.31
		Normal	50	2000	805	20.13	34.21	54.34
All-on-4	1	Tangent	50	1190	805	33.82	57.50	91.32
		Binormal	50	400	805	100.63	171.06	271.69
		Normal	50	800	805	50.31	85.53	135.84
	2	Tangent	50	1100	805	36.59	62.20	98.80
		Binormal	50	800	805	50.31	85.53	135.84
		Normal	50	750	805	53.67	91.23	144.90

Table 4.11.: Determination of displacement at ultimate tensile strength (UTS) for a titanium framework, bone, and the total misfit for different prosthesis types, implant positions, and directions, starting from the stress when a 50 [μm] misfit is applied.

			Zirconia				Bone	Total
Prosthesis Type	Implant Position	Direction	Misfit [μm]	Maximum Stress [MPa]	UTS [MPa]	Misfit if UTS [μm]	Misfit [μm]	Misfit [μm]
All-on-8	1	Tangent	50	4460	850	9.53	27.63	37.16
		Binormal	50	1910	850	22.25	64.53	86.78
		Normal	50	2800	850	15.18	44.02	59.20
	2	Tangent	50	4600	850	9.24	26.79	36.03
		Binormal	50	2050	850	20.73	60.12	80.85
		Normal	50	3000	850	14.17	41.08	55.25
	3	Tangent	50	3430	850	12.39	35.93	48.32
		Binormal	50	2020	850	21.04	61.02	82.06
		Normal	50	2800	850	15.18	44.02	59.20
	4	Tangent	50	6000	850	7.08	20.54	27.62
		Binormal	50	3255	850	13.06	37.86	50.92
		Normal	50	3570	850	11.90	34.52	46.42
All-on-6	1	Tangent	50	2030	850	20.94	60.71	81.65
		Binormal	50	670	850	63.43	183.95	247.38
		Normal	50	1350	850	31.48	91.30	122.78
	2	Tangent	50	2800	850	15.18	44.02	59.20
		Binormal	50	1800	850	23.61	68.47	92.08
		Normal	50	3000	850	14.17	41.08	55.25
	3	Tangent	50	5720	850	7.43	21.55	28.98
		Binormal	50	3340	850	12.72	36.90	49.62
		Normal	50	3460	850	12.28	35.62	47.90
All-on-4	1	Tangent	50	2060	850	20.63	59.83	80.46
		Binormal	50	700	850	60.71	176.07	236.78
		Normal	50	1380	850	30.80	89.31	120.11
	2	Tangent	50	1910	850	22.25	64.53	86.78
		Binormal	50	1370	850	31.02	89.96	120.98
		Normal	50	1300	850	32.69	94.81	127.5

Table 4.12.: Determination of displacement at ultimate tensile strength (UTS) for a zirconia framework, bone, and the total misfit for different prosthesis types, implant positions, and directions, starting from the stress when a 50 [μm] misfit is applied.

5. Perspectives

5.1. Assumptions

In this thesis, the bone is considered isotropic. However, this assumption does not accurately represent reality. To enhance the precision of stiffness calculations, and thus displacement calculations, it is necessary to account for the anisotropic nature of bone, which would better capture its true mechanical behaviour under various loading conditions.

Furthermore, the problem is treated as linear, but certain regions, particularly those where plastic deformation occurs, require a nonlinear approach. Addressing this nonlinearity is essential for a more accurate representation of the mechanical response.

To avoid singularities in the model, the geometry could be refined to make it less angular, dedicating more time to the development of the CAD model. This refinement would help create a more robust model, requiring less post-treatment of the simulation results.

It is also essential to consider bone more precisely in experimental tests. A more detailed modelling approach would enable more accurate simulation of bone behaviour, providing better insights into the implant-bone interaction.

The theoretical scenarios involve displacement in only one spatial direction, with all other possible movements constrained. This simplification does not reflect practical situations where multidirectional forces and movements are present. Addressing this limitation would enhance the applicability of the findings to more realistic scenarios.

By refining these aspects, the accuracy and reliability of implantology models can be significantly improved, ultimately leading to better clinical outcomes.

5.2. New Materials

The titanium alloy Ti-6Al-4V, commonly used in biomedical applications, has recently come under scrutiny due to its elastic modulus of 110 GPa, which is significantly higher than that of bone tissue (5-30 GPa) [69]. This disparity can lead to the "stress shielding" phenomenon, where the implant absorbs the loads instead of stimulating the bone tissue, resulting in peri-implant bone resorption [70, 71, 72, 73, 74, 75]. To address this mechanical incompatibility, researchers have proposed several solutions. The first one consists in using titanium alloys with lower moduli of elasticity and higher resistance to compression, such as beta titanium [76, 77, 78, 79, 80, 81]. The second solution consists in developing porous implants through additive manufacturing, which reduces the modulus of elasticity based on the amount and size of the pores and promotes internal bone growth for mechanical interlocking [76, 82, 77, 83, 84, 85, 86, 87, 88, 89, 90, 91]. The third solution is applying graded coatings with bioactive hydroxyapatite(HA)/collagen to achieve a similar modulus of elasticity at the implant/bone interface [76, 92, 93, 77, 94, 95, 96, 97, 98].

6. Conclusion

This thesis aimed to determine the influence of misfit on implant-supported prostheses, particularly focusing on the All-on-4, All-on-6 and All-on-8 configurations. Through Finite Element Analysis (FEA), the study simulated the effect of a 50 [μm] misfit in different directions on the prosthesis to determine the conditions that are the most detrimental to implant stability and bone integrity.

The analysis revealed several key findings. First, the tangent direction consistently was the most detrimental direction of misfit across all prostheses configurations. This direction induced the highest stresses and reaction forces, especially in the first and second access holes. This highlights the need for precise alignment in this axis to minimize potential complications. Second, a comparison of the two analysed materials, titanium (Ti-6Al-4V) and zirconia (Y-TZP), indicated distinct stress distribution patterns attributable to their differing mechanical properties. Zirconia, with its higher Young's modulus, showed higher stress concentrations compared to titanium. This suggests that although zirconia offers superior aesthetic properties, titanium may be more resilient to misfit-induced stresses, making it a preferable choice in scenarios where misfit is likely. These findings underscore the importance of achieving a passive fit in implant-supported prostheses. Even small misfits can lead to significant stress concentrations, potentially compromising implant stability and bone health. Therefore, clinicians must prioritize precision in both surgical placement and prothesis fabrication to ensure long-term success.

The implications of these findings suggest that further research is needed to explore the effects of dynamic loadings and long-term wear on prostheses with misfits. Additionally, the development of new materials and fabrication techniques that can better accommodate minor misfits could enhance the durability and performance of implant-supported prostheses.

In conclusion, this study highlights the critical role of fit accuracy in the success of implant-supported prostheses. By understanding the biomechanical implications of misfit and selecting appropriate materials and configurations, dental professionals can improve patient outcomes and extend the lifespan of these restorative solutions. The research provides a comprehensive of understanding of the factors that influence the stability and functionality of implant-supported prostheses, paving the way for improved clinical practices and enhanced patient care.

Appendix

A. Zirconia frameworks

A.1. All-on-8

A.1.1. First Access Hole

Tangent

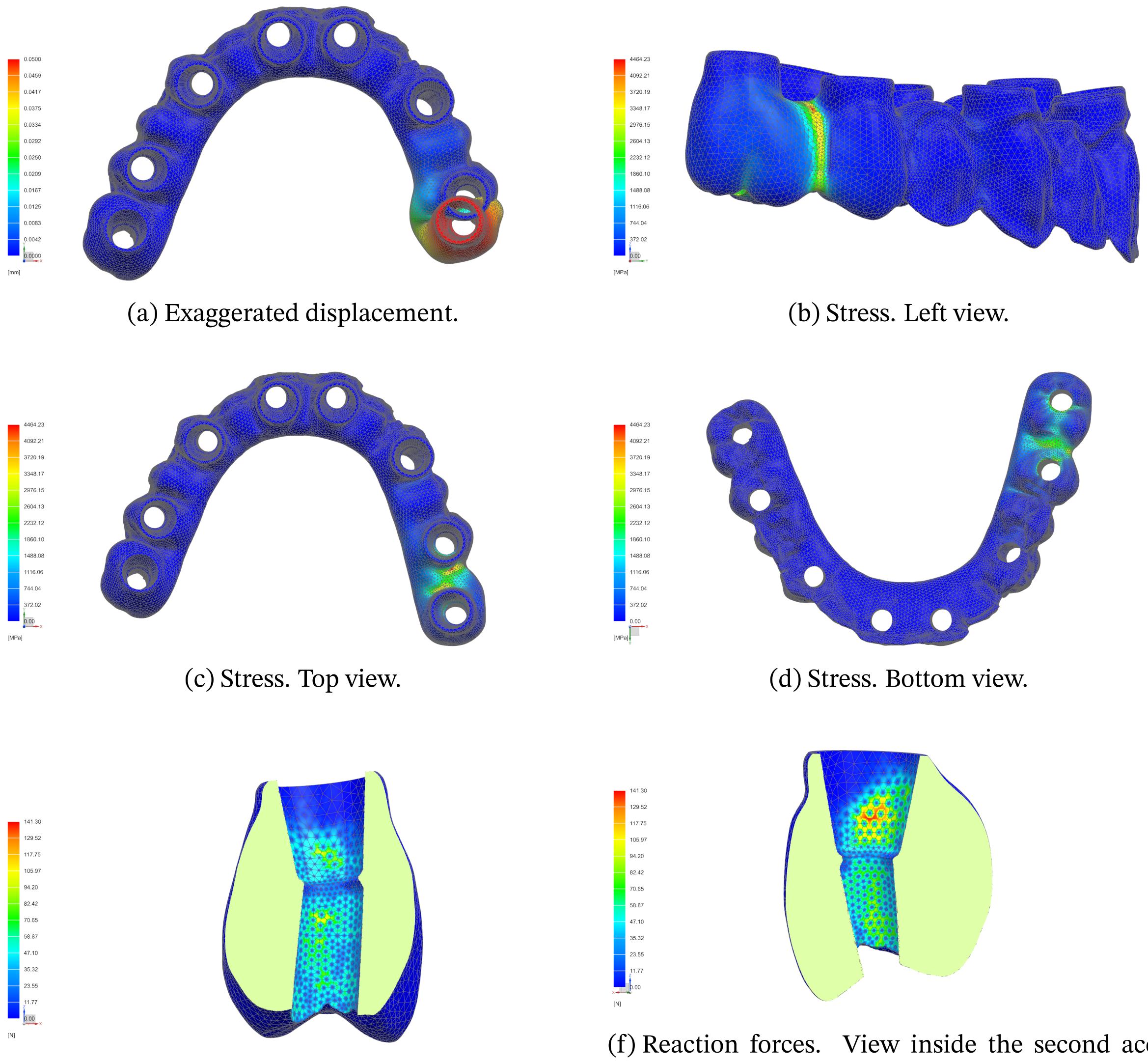

(a) Exaggerated displacement.

(b) Stress. Left view.

(c) Stress. Top view.

(d) Stress. Bottom view.

(e) Reaction forces. View inside the first access hole.

(f) Reaction forces. View inside the second access hole.

Figure A.1.: 50 [μm] misfit in the tangent direction applied on the first access hole of an All-on-8 prosthesis.

Binormal

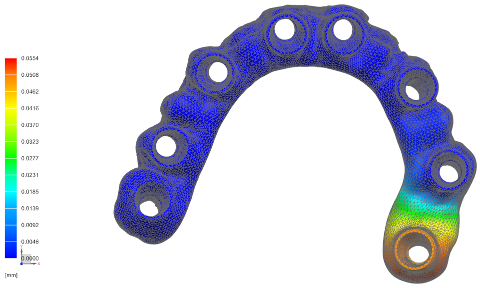

(a) Exaggerated displacement.

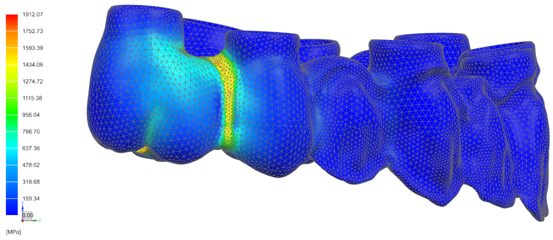

(b) Stress. Left view.

(c) Stress. Top view.

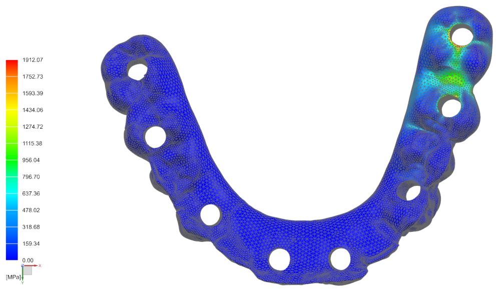

(d) Stress. Bottom view.

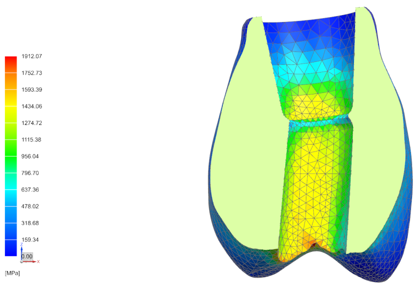

(e) Reaction forces. View inside the first access hole.

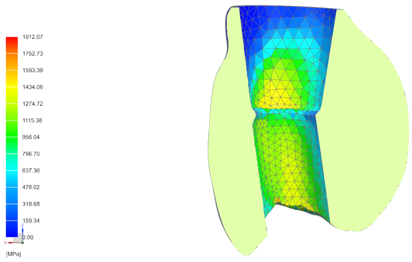

(f) Reaction forces. View inside the second access hole.

Figure A.2.: 50 [μm] misfit in the binormal direction applied on the first access hole of an All-on-8 prosthesis.

Normal

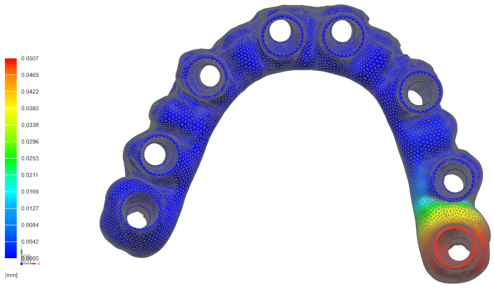

(a) Exaggerated displacement.

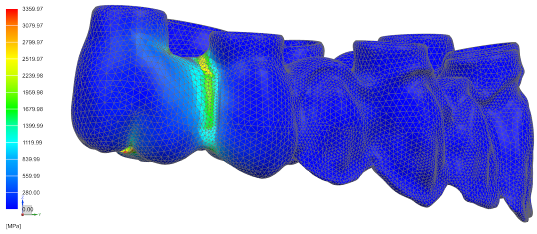

(b) Stress. Left view.

(c) Stress. Top view.

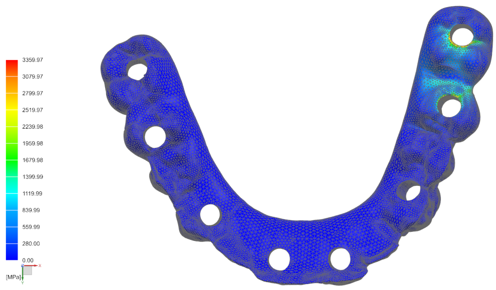

(d) Stress. Bottom view.

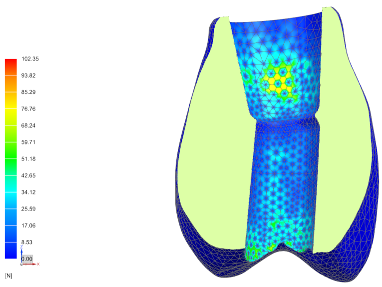

(e) Reaction forces. View inside the first access hole.

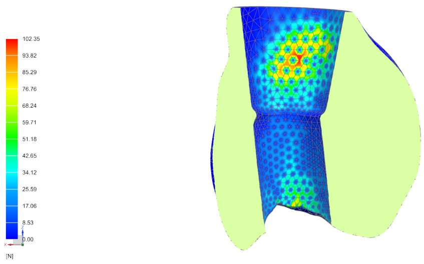

(f) Reaction forces. View inside the second access hole.

Figure A.3.: 50 [μm] misfit in the normal direction applied on the first access hole of an All-on-8 prosthesis.

A.1.2. Second Access Hole

Tangent

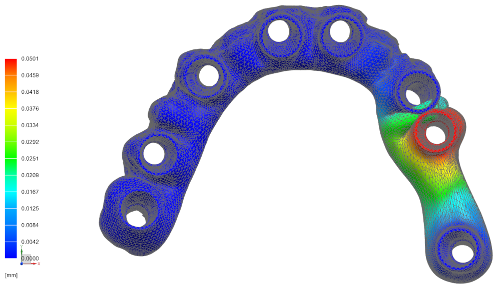

(a) Exaggerated displacement.

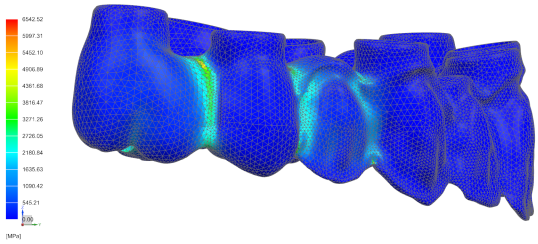

(b) Stress. Left view.

(c) Stress. Top view.

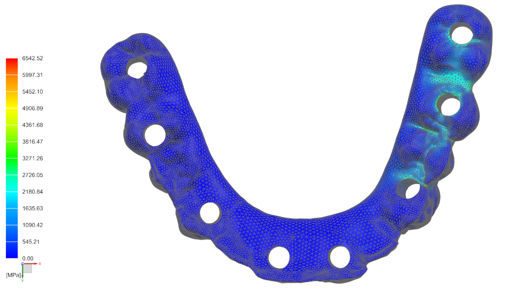

(d) Stress. Bottom view.

Figure A.4.: 50 [μm] misfit in the tangent direction applied on the second access hole of an All-on-8 prosthesis.

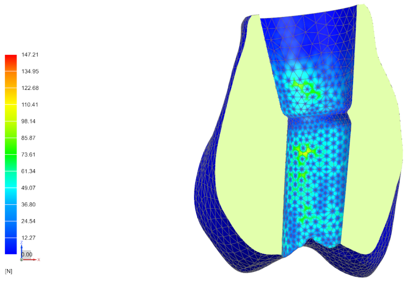

(a) Reaction forces on the first access hole.

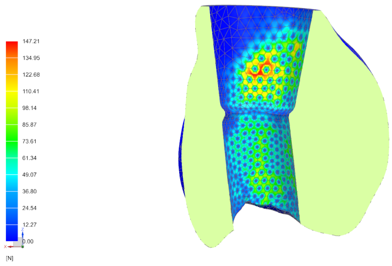

(b) Reaction forces on the second access hole.

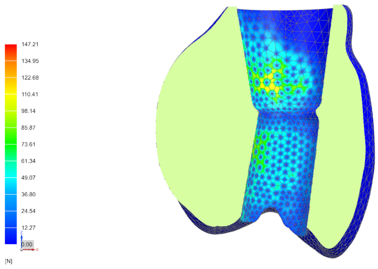

(c) Reaction forces on the second access hole.

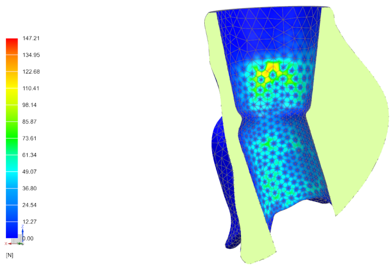

(d) Reaction forces on the third access hole.

Figure A.5.: Reaction forces for an All-on-8 prosthesis with a 50 [μm] misfit in the tangent direction applied on the second access hole.

Binormal

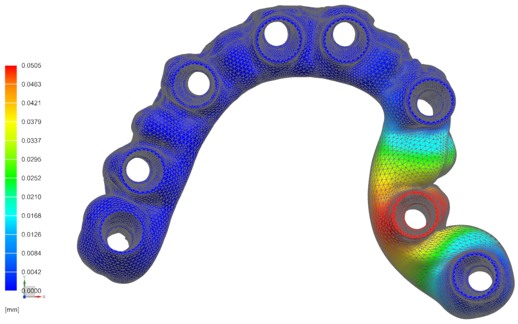

(a) Exaggerated displacement.

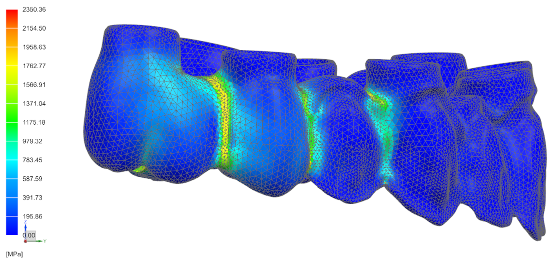

(b) Stress. Left view.

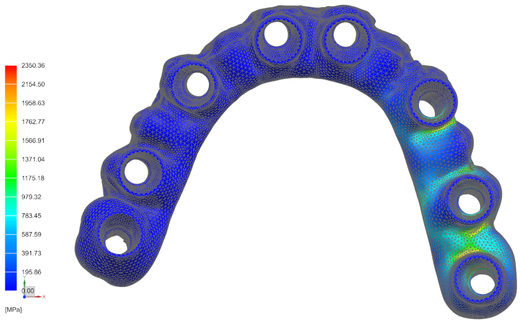

(c) Stress. Top view.

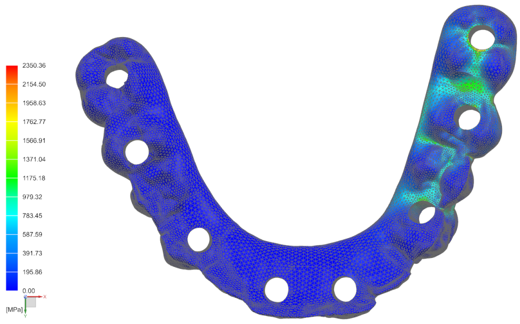

(d) Stress. Bottom view.

Figure A.6.: 50 [μm] misfit in the binormal direction applied on the second access hole of an All-on-8 prosthesis.

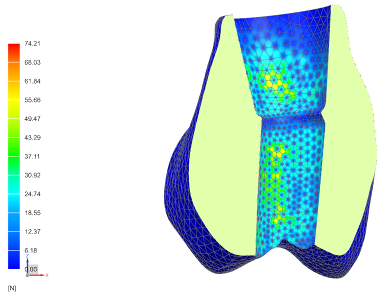

(a) Reaction forces on the first access hole.

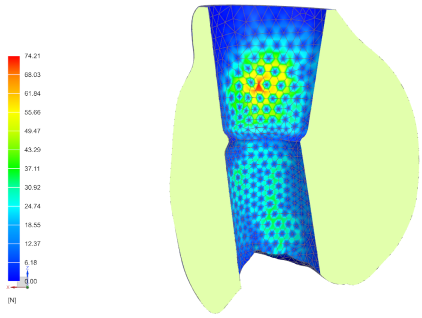

(b) Reaction forces on the second access hole.

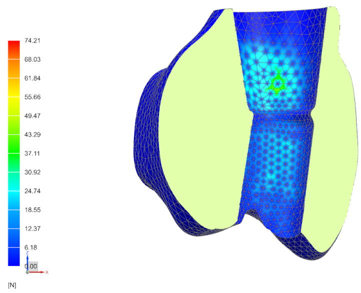

(c) Reaction forces on the second access hole.

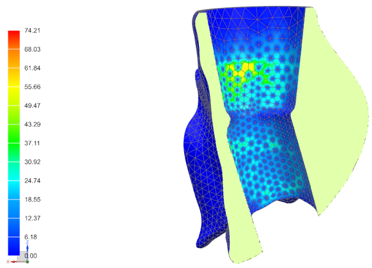

(d) Reaction forces on the third access hole.

Figure A.7.: Reaction forces for an All-on-8 prosthesis with a 50 [μm] misfit in the binormal direction applied on the second access hole.

Normal

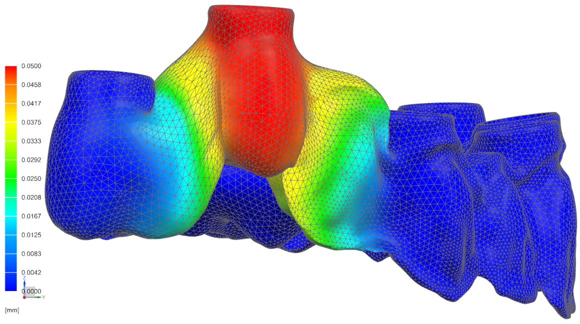

(a) Exaggerated displacement.

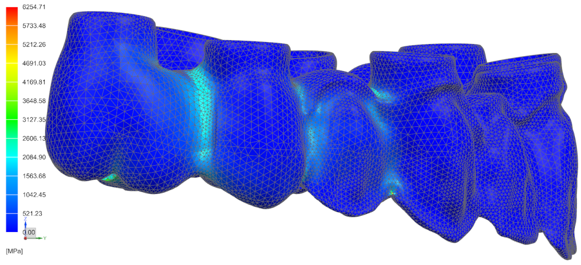

(b) Stress. Left view.

(c) Stress. Top view.

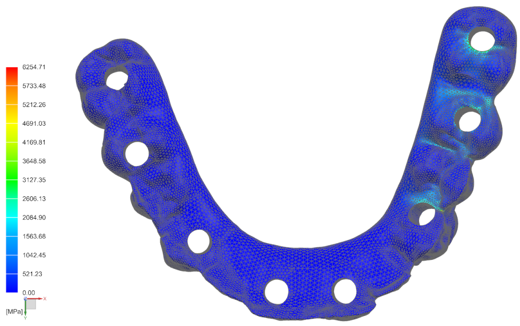

(d) Stress. Bottom view.

Figure A.8.: 50 [μm] misfit in the normal direction applied on the second access hole of an All-on-8 prosthesis.

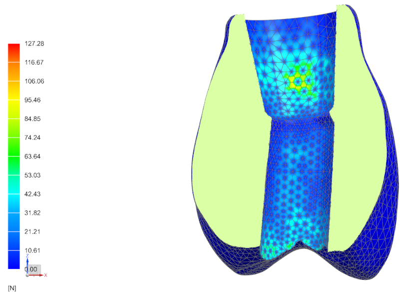

(a) Reaction forces on the first access hole.

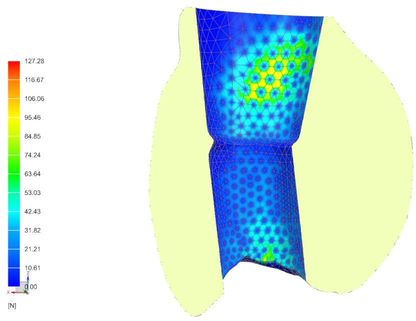

(b) Reaction forces on the second access hole.

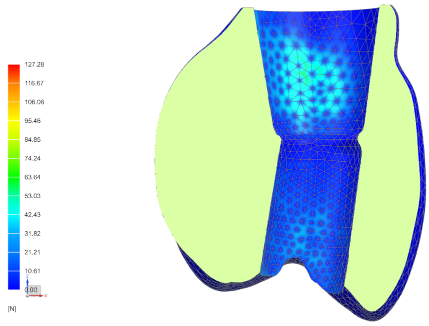

(c) Reaction forces on the second access hole.

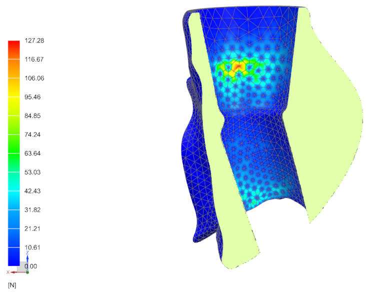

(d) Reaction forces on the third access hole.

Figure A.9.: Reaction forces for an All-on-8 prosthesis with a 50 [μm] misfit in the normal direction applied on the second access hole.

A.1.3. Third Access Hole

Tangent

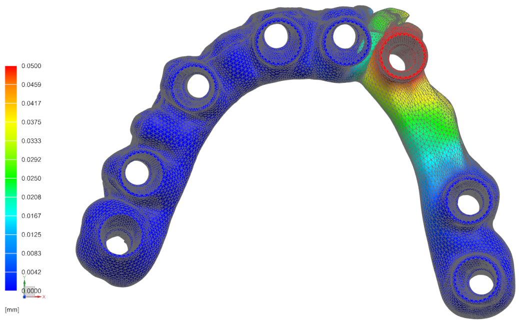

(a) Exaggerated displacement.

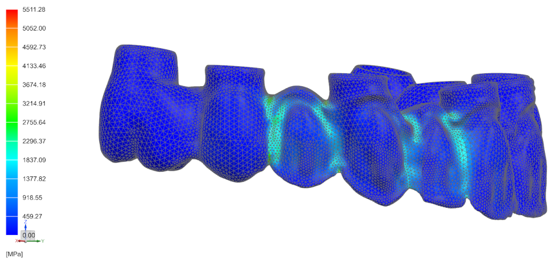

(b) Stress. Face view.

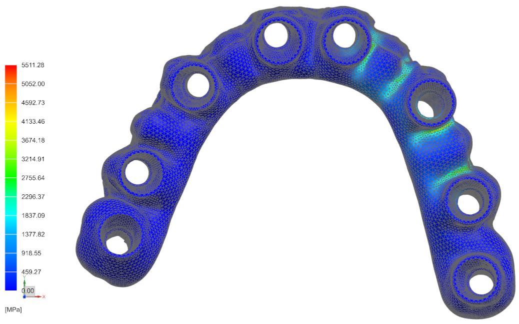

(c) Stress. Top view.

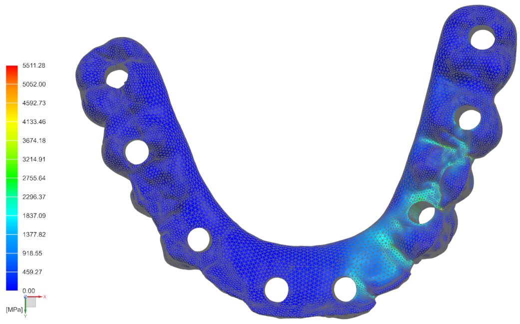

(d) Stress. Bottom view.

Figure A.10.: 50 [μm] misfit in the tangent direction applied on the third access hole of an All-on-8 prosthesis.

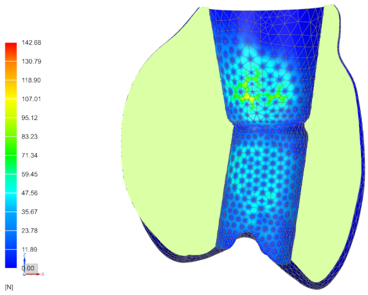

(a) Reaction forces on the second access hole.

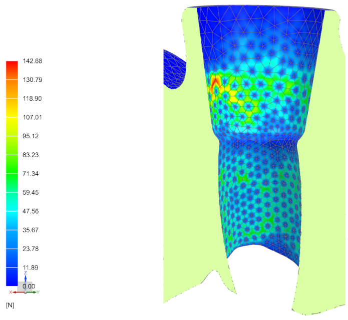

(b) Reaction forces on the third access hole.

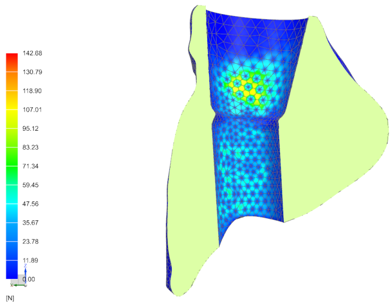

(c) Reaction forces on the fourth access hole.

Figure A.11.: Reaction forces for an All-on-8 prosthesis with a 50 [μm] misfit in the tangent direction applied on the third access hole.

Binormal

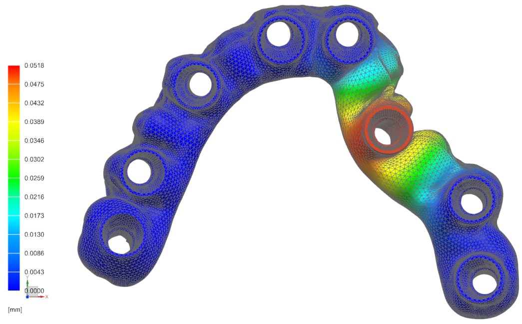

(a) Exaggerated displacement.

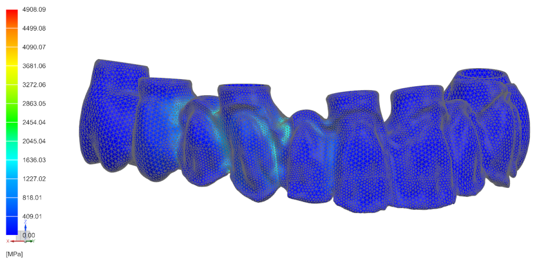

(b) Stress. Face view.

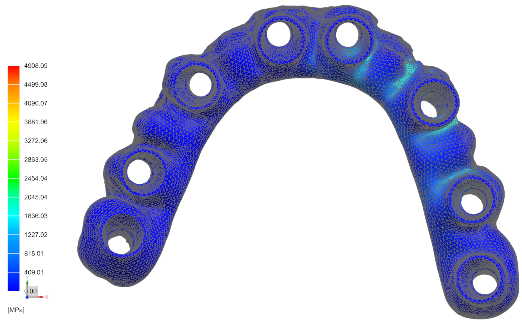

(c) Stress. Top view.

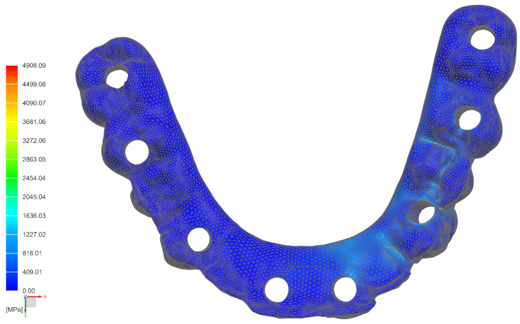

(d) Stress. Bottom view.

Figure A.12.: 50 [μm] misfit in the binormal direction applied on the third access hole of an All-on-8 prosthesis.

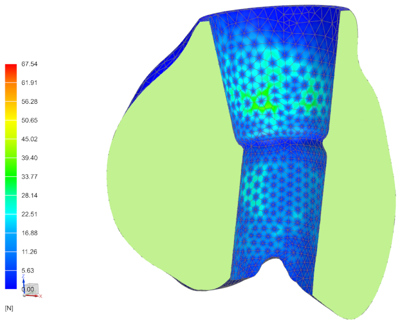

(a) Reaction forces on the second access hole.

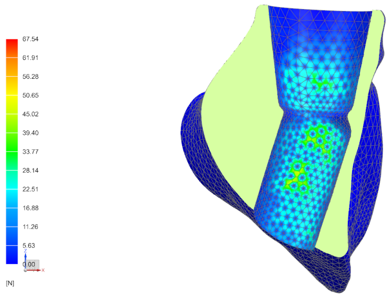

(b) Reaction forces on the third access hole.

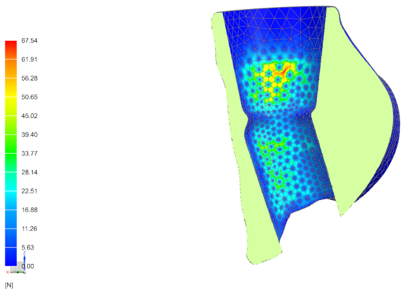

(c) Reaction forces on the fourth access hole.

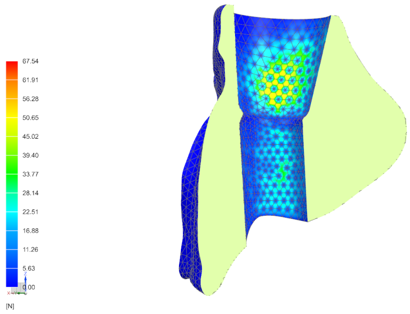

(d) Reaction forces on the second access hole.

Figure A.13.: Reaction forces for an All-on-8 prosthesis with a 50 [μm] misfit in the binormal direction applied on the third access hole.

Normal

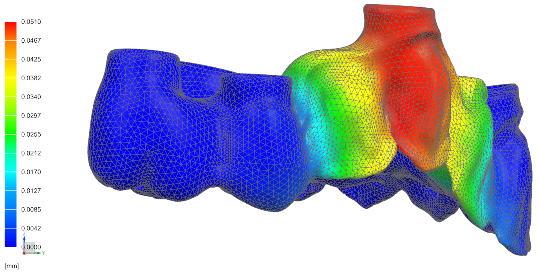

(a) Exaggerated displacement.

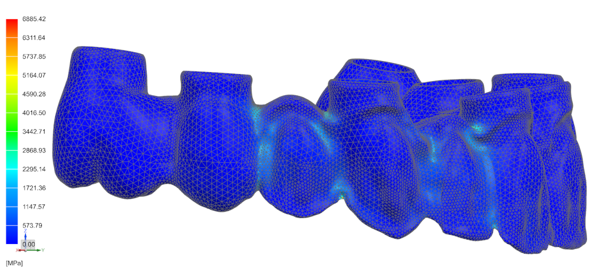

(b) Stress. Left view.

(c) Stress. Top view.

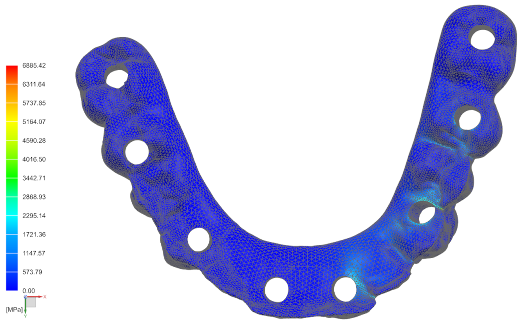

(d) Stress. Bottom view.

Figure A.14.: 50 [μm] misfit in the tangent direction applied on the third access hole of an All-on-8 prosthesis.

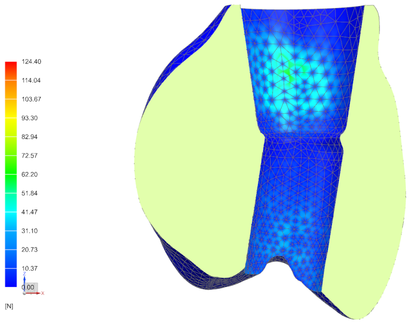

(a) Reaction forces on the second access hole.

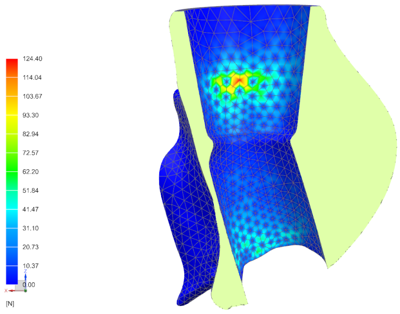

(b) Reaction forces on the third access hole.

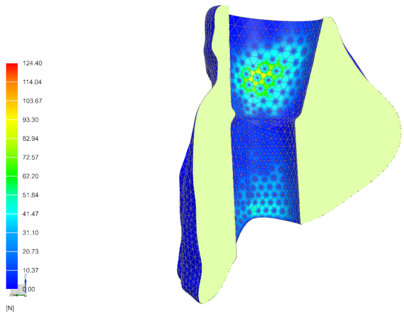

(c) Reaction forces on the fourth access hole.

Figure A.15.: Reaction forces for an All-on-8 prosthesis with a 50 [μm] misfit in the normal direction applied on the third access hole.

A.1.4. Fourth Access Hole

Tangent

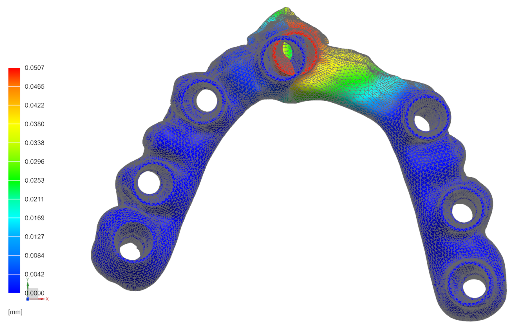

(a) Exaggerated displacement.

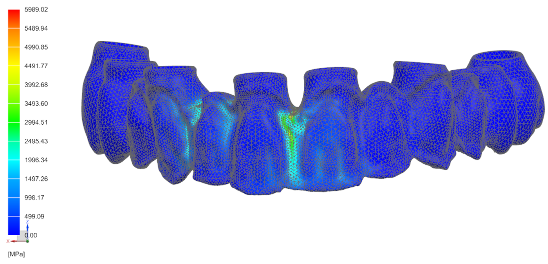

(b) Stress. Face view.

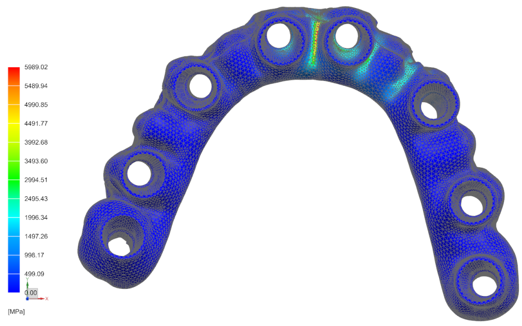

(c) Stress. Top view.

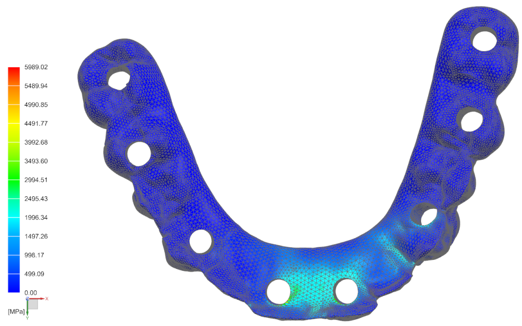

(d) Stress. Bottom view.

Figure A.16.: 50 [μm] misfit in the tangent direction applied on the fourth access hole of an All-on-8 prosthesis.

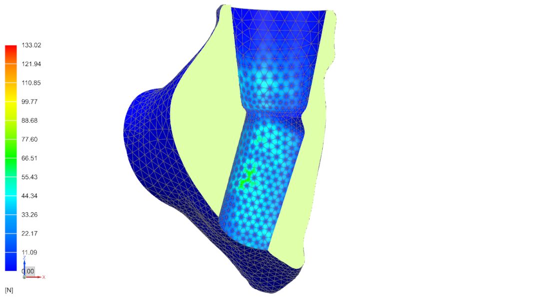

(a) Reaction forces on the third access hole.

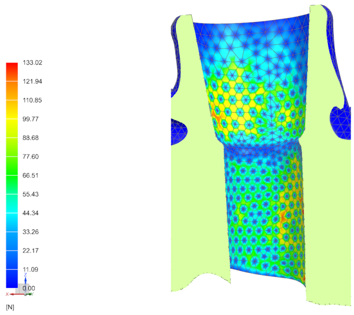

(b) Reaction forces on the fourth access hole.

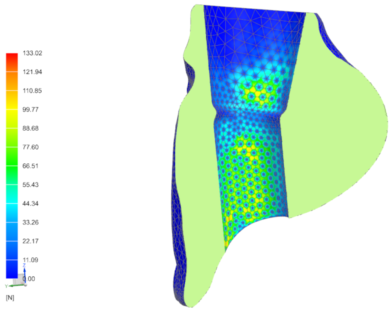

(c) Reaction forces on the fifth access hole.

Figure A.17.: Reaction forces for an All-on-8 prosthesis with a 50 [μm] misfit in the tangent direction applied on the fourth access hole.

Binormal

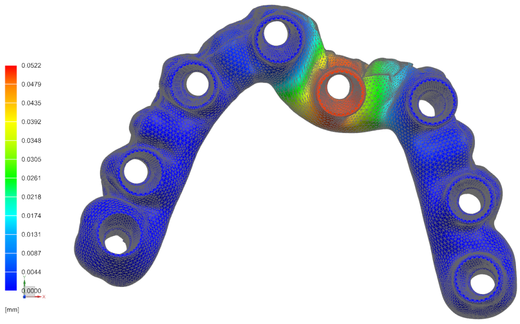

(a) Exaggerated displacement.

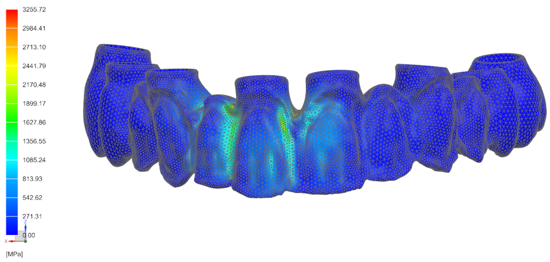

(b) Stress. Face view.

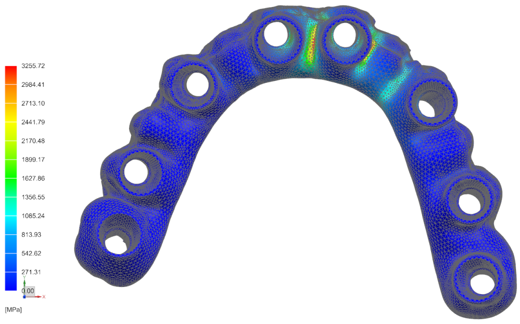

(c) Stress. Top view.

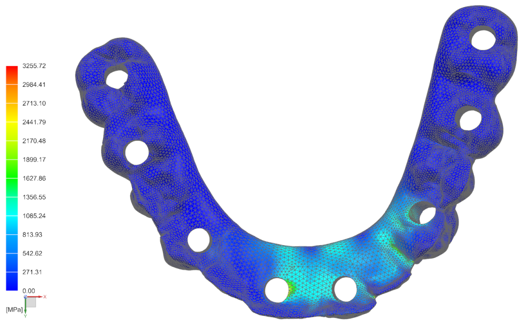

(d) Stress. Bottom view.

Figure A.18.: 50 [μm] misfit in the binormal direction applied on the fourth access hole of an All-on-8 prosthesis.

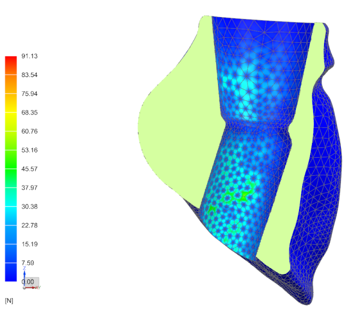

(a) Reaction forces on the third access hole.

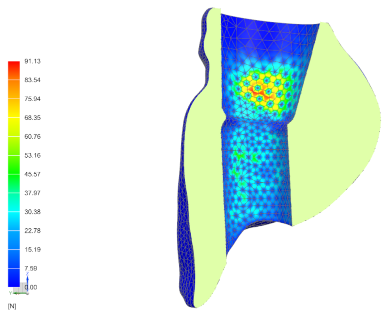

(b) Reaction forces on the fourth access hole.

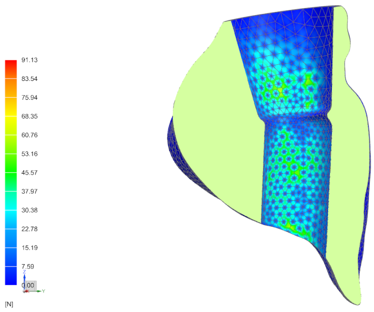

(c) Reaction forces on the fourth access hole.

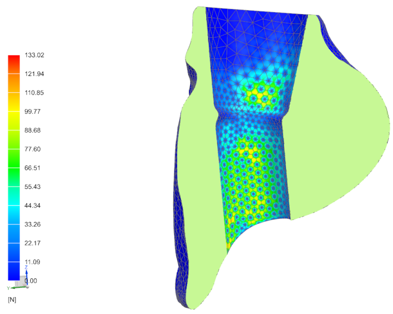

(d) Reaction forces on the fifth access hole.

Figure A.19.: Reaction forces for an All-on-8 prosthesis with a 50 [μm] misfit in the binormal direction applied on the fourth access hole.

Normal

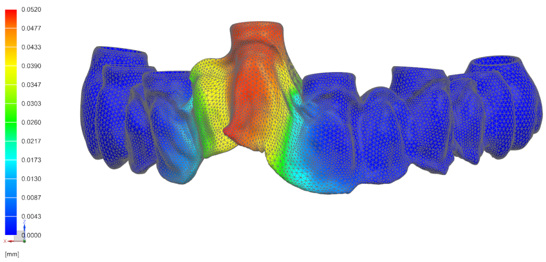

(a) Exaggerated displacement.

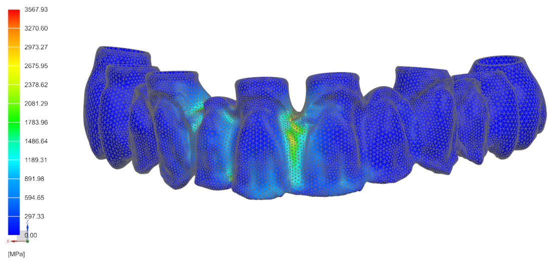

(b) Stress. Face view.

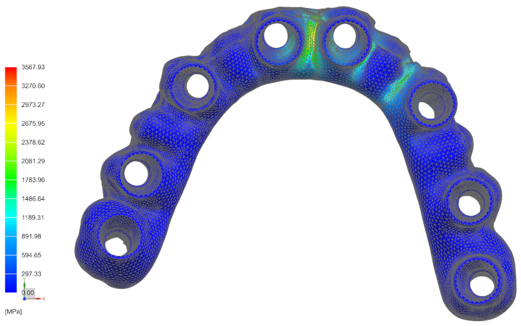

(c) Stress. Top view.

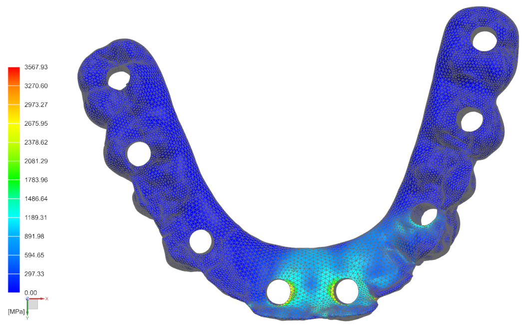

(d) Stress. Bottom view.

Figure A.20.: 50 [μm] misfit in the normal direction applied on the fourth access hole of an All-on-8 prosthesis.

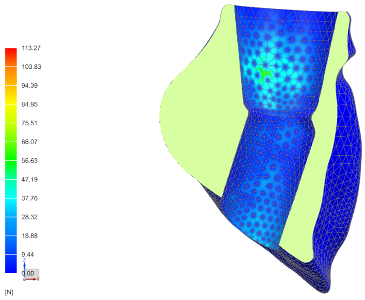

(a) Reaction forces on the third access hole.

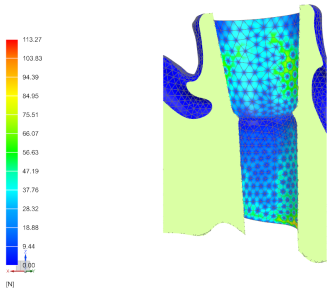

(b) Reaction forces on the fourth access hole.

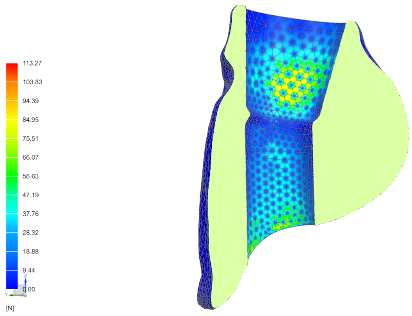

(c) Reaction forces on the fifth access hole.

Figure A.21.: Reaction forces for an All-on-8 prosthesis with a 50 [μm] misfit in the normal direction applied on the fourth access hole.

A.2. All-on-6

A.2.1. First Access Hole

Tangent

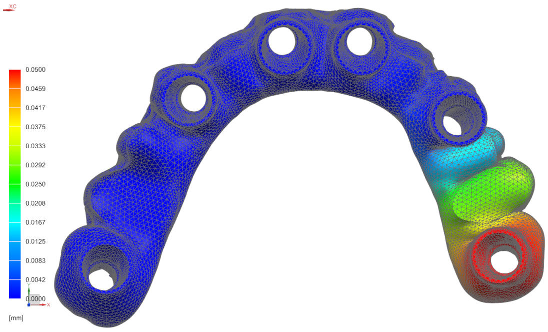

(a) Exaggerated displacement.

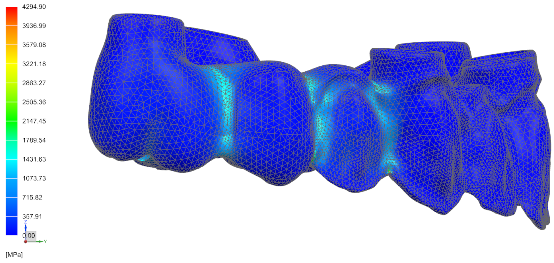

(b) Stress. Left view.

(c) Stress. Top view.

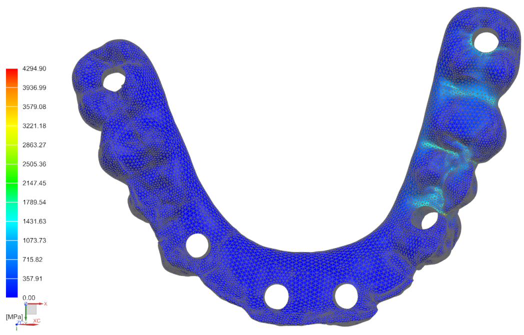

(d) Stress. Bottom view.

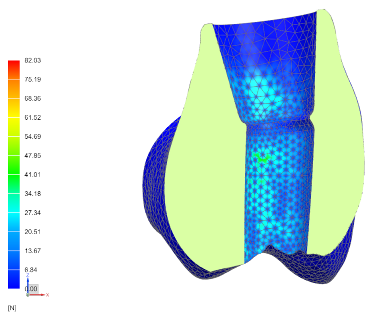

(e) Reaction forces. View inside the first access hole.

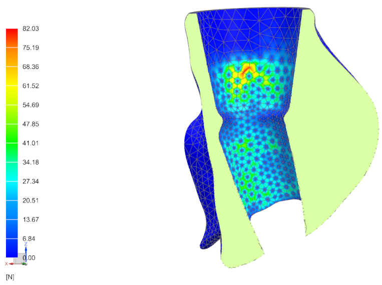

(f) Reaction forces. View inside the second access hole.

Figure A.22.: 50 [μm] misfit in the tangent direction applied on the first access hole of an All-on-6 prosthesis.

Binormal

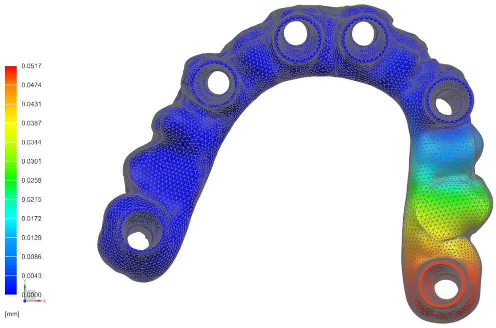

(a) Exaggerated displacement.

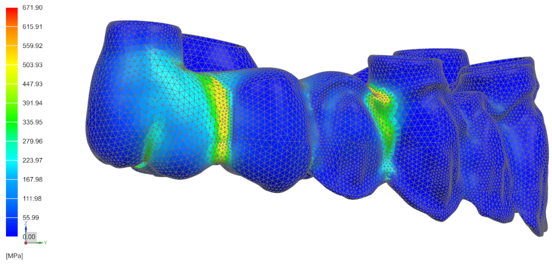

(b) Stress. Left view.

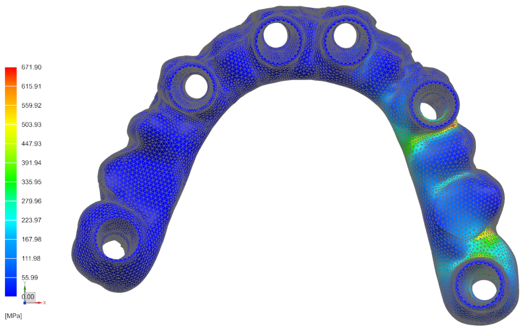

(c) Stress. Top view.

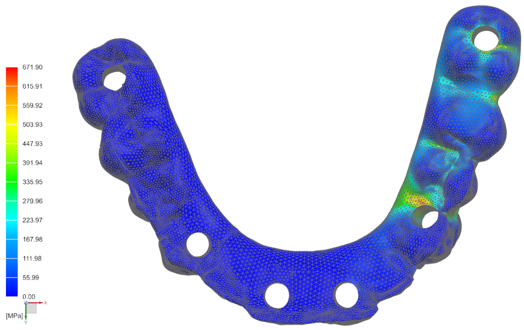

(d) Stress. Bottom view.

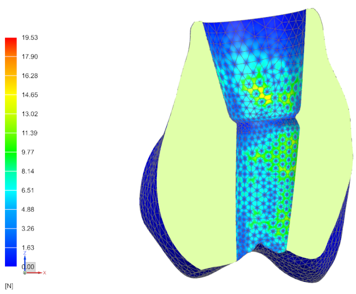

(e) Reaction forces. View inside the first access hole.

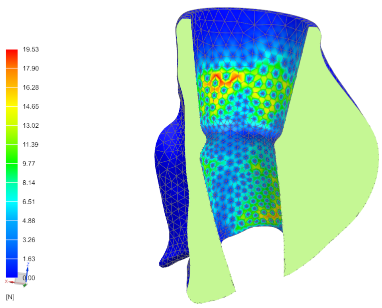

(f) Reaction forces. View inside the second access hole.

Figure A.23.: 50 [μm] misfit in the binormal direction applied on the first access hole of an All-on-6 prosthesis.

Normal

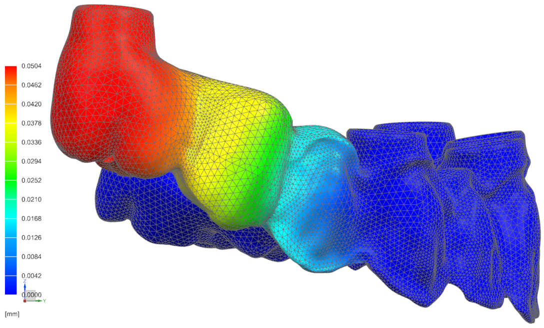

(a) Exaggerated displacement.

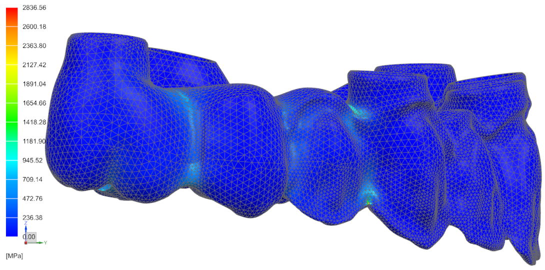

(b) Stress. Left view.

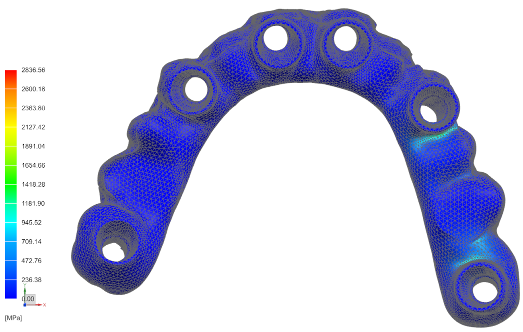

(c) Stress. Top view.

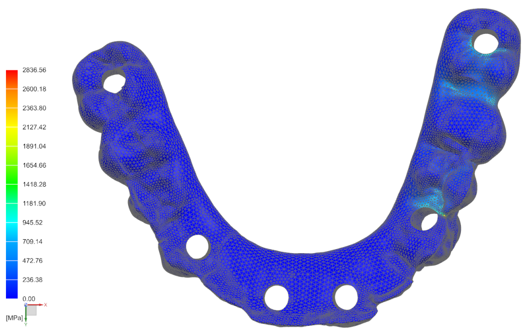

(d) Stress. Bottom view.

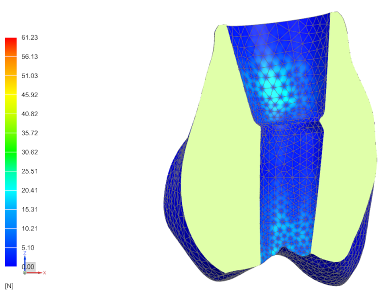

(e) Reaction forces. View inside the first access hole.

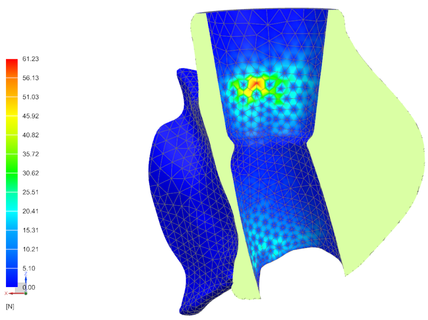

(f) Reaction forces. View inside the second access hole.

Figure A.24.: 50 [μm] misfit in the normal direction applied on the first access hole of an All-on-6 prosthesis.

A.2.2. Second Access Hole

Tangent

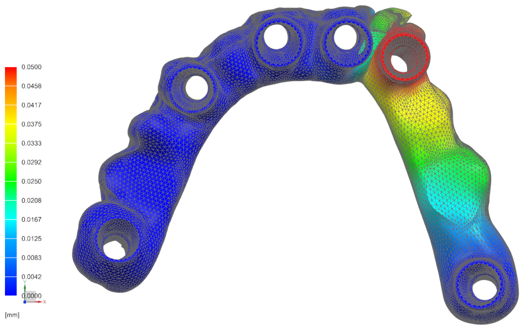

(a) Exaggerated displacement.

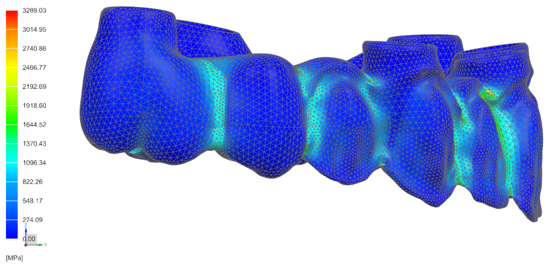

(b) Stress. Left view.

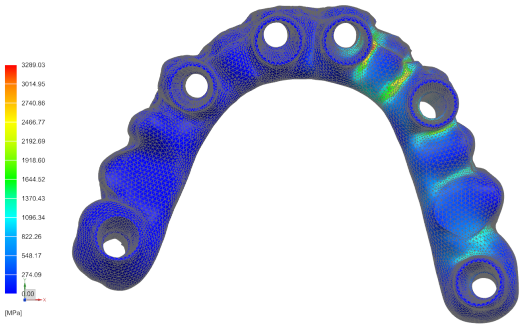

(c) Stress. Top view.

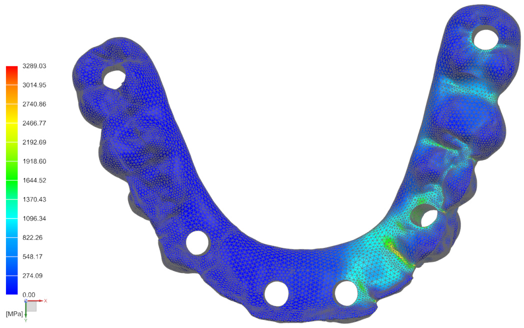

(d) Stress. Bottom view.

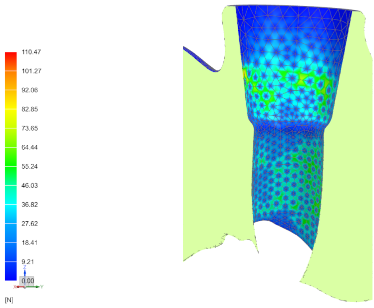

(e) Reaction forces. View inside the second access hole.

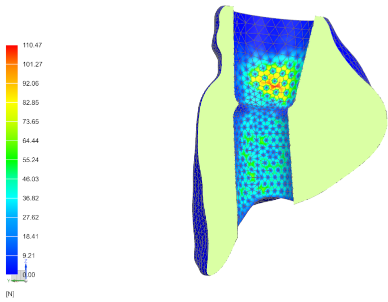

(f) Reaction forces. View inside the third access hole.

Figure A.25.: 50 [μm] misfit in the tangent direction applied on the second access hole of an All-on-6 prosthesis.

Binormal

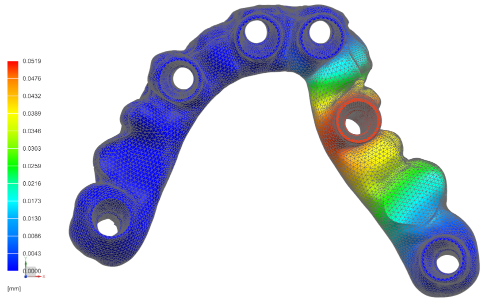

(a) Exaggerated displacement.

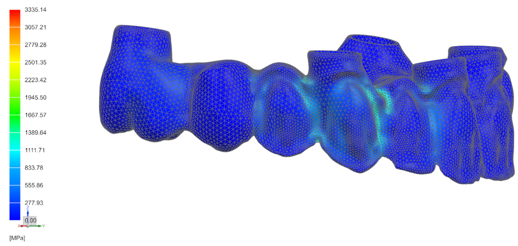

(b) Stress. Left view.

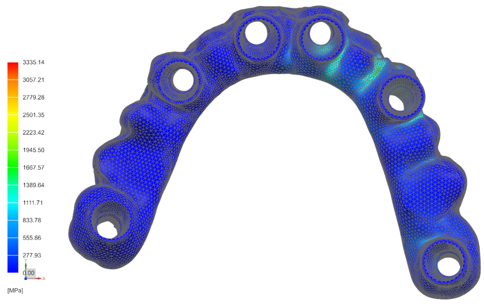

(c) Stress. Top view.

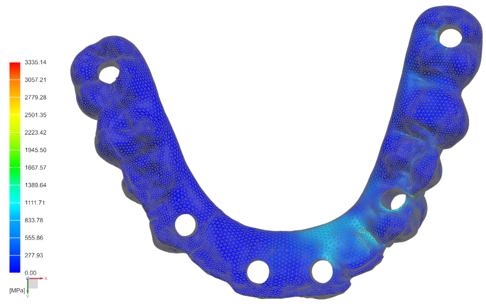

(d) Stress. Bottom view.

Figure A.26.: Displacement and stress caused by a 50 [μm] misfit in the binormal direction applied on the second access hole of an All-on-6 prosthesis.

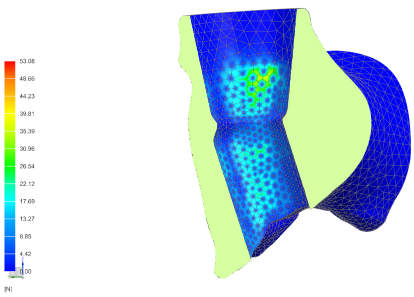

(a) Reaction forces on the second access hole.

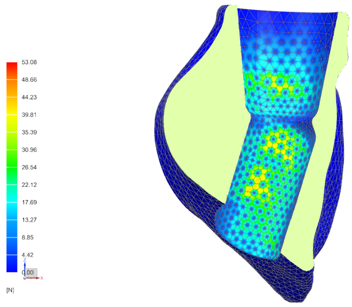

(b) Reaction forces on the second access hole.

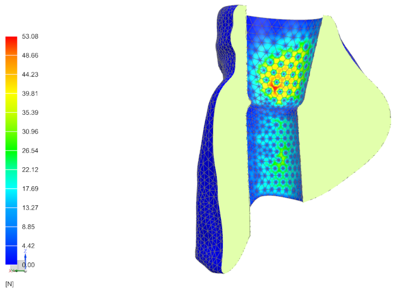

(c) Reaction forces on the third access hole.

Figure A.27.: Reaction forces for an All-on-6 prosthesis with a 50 [μm] misfit in the binormal direction applied on the second access hole.

Normal

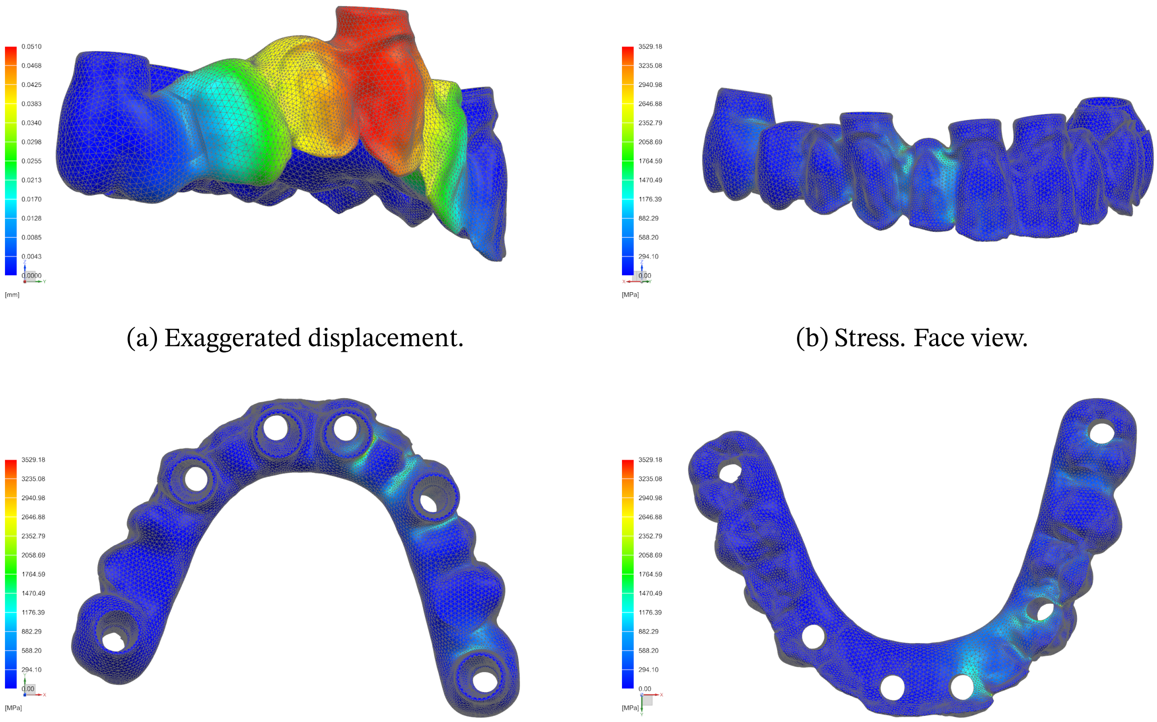

(a) Exaggerated displacement.

(b) Stress. Face view.

(c) Stress. Top view.

(d) Stress. Bottom view.

Figure A.28.: Displacement and stress caused by a 50 [μm] misfit in the normal direction applied on the second access hole of an All-on-6 prosthesis.

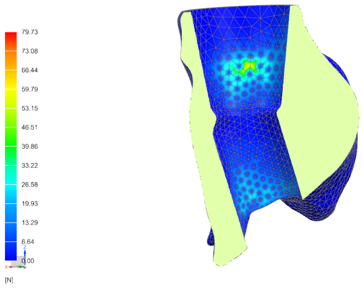

(a) Reaction forces on the second access hole.

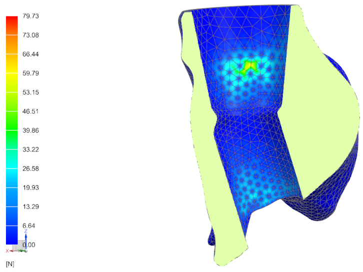

(b) Reaction forces on the second access hole.

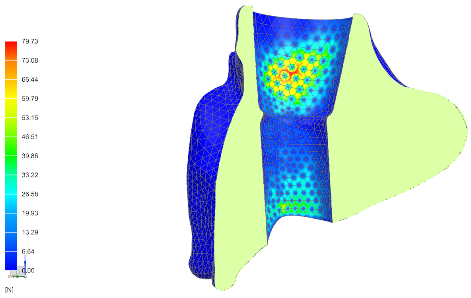

(c) Reaction forces on the third access hole.

Figure A.29.: Reaction forces for an All-on-6 prosthesis with a 50 [μm] misfit in the normal direction applied on the second access hole.

A.2.3. Third Access Hole

Tangent

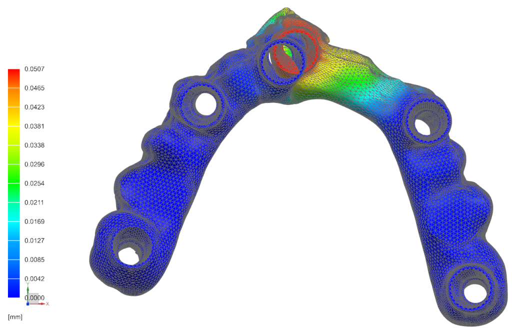

(a) Exaggerated displacement.

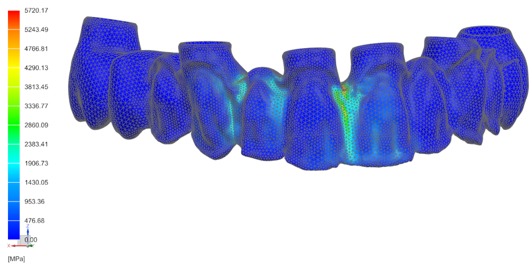

(b) Stress. Face view.

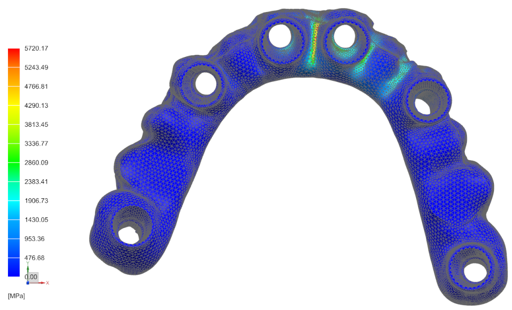

(c) Stress. Top view.

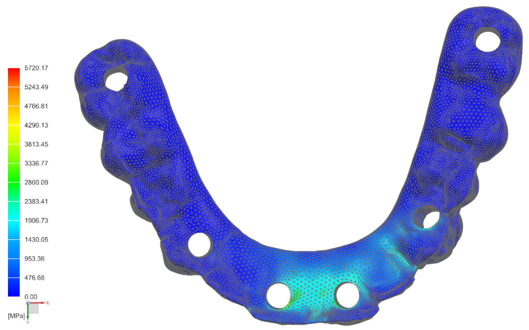

(d) Stress. Bottom view.

Figure A.30.: Displacement and stress caused by a 50 [μm] misfit in the tangent direction applied on the third access hole of an All-on-6 prosthesis.

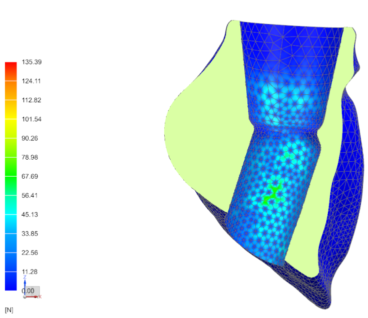

(a) Reaction forces on the second access hole.

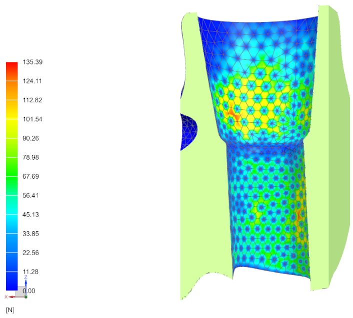

(b) Reaction forces on the third access hole.

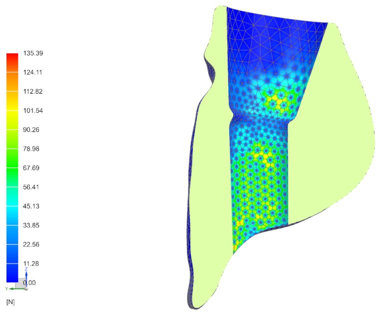

(c) Reaction forces on the fourth access hole.

Figure A.31.: Reaction forces for an All-on-6 prosthesis with a 50 [μm] misfit in the tangent direction applied on the second access hole.

Binormal

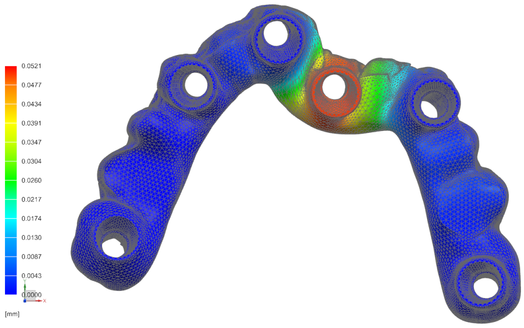

(a) Exaggerated displacement.

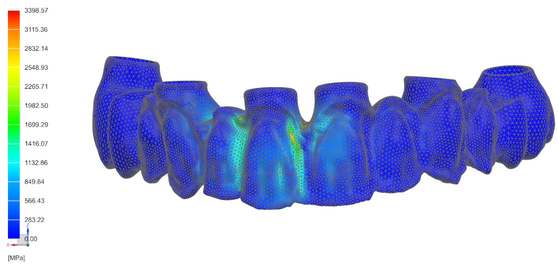

(b) Stress. Face view.

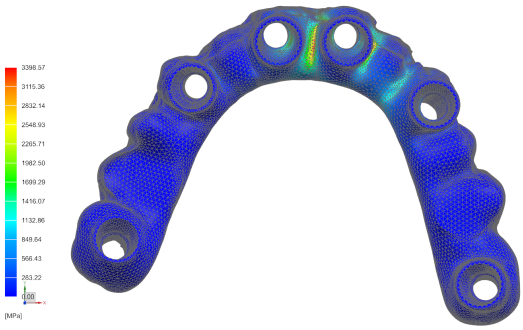

(c) Stress. Top view.

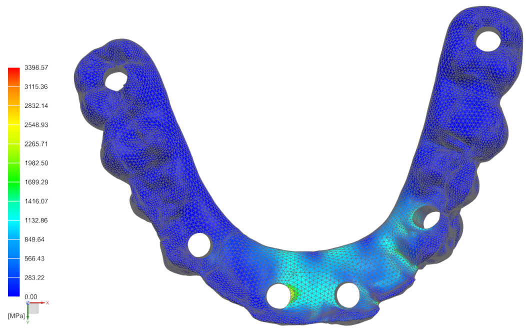

(d) Stress. Bottom view.

Figure A.32.: Displacement and stress caused by a 50 [μm] misfit in the binormal direction applied on the third access hole of an All-on-6 prosthesis.

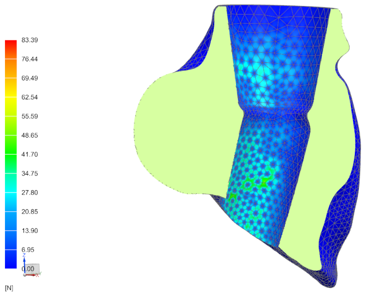

(a) Reaction forces on the second access hole.

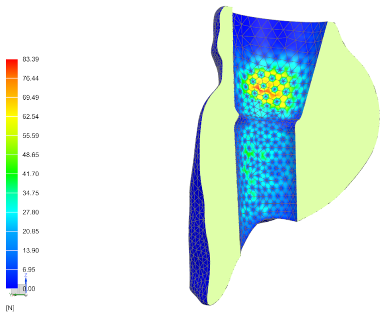

(b) Reaction forces on the third access hole.

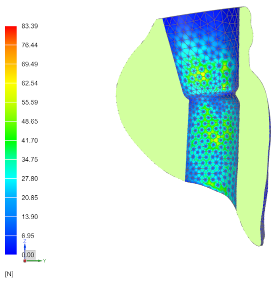

(c) Reaction forces on the third access hole.

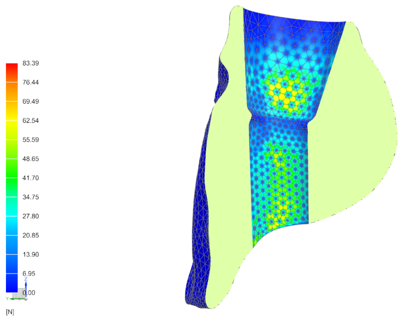

(d) Reaction forces on the fourth access hole.

Figure A.33.: Reaction forces for an All-on-6 prosthesis with a 50 [μm] misfit in the binormal direction applied on the second access hole.

Normal

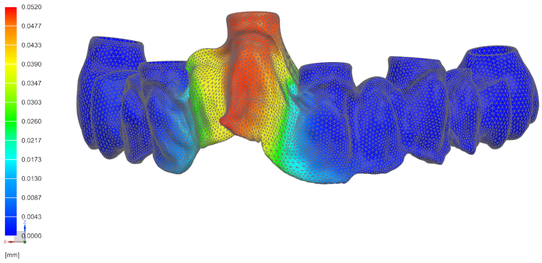

(a) Exaggerated displacement.

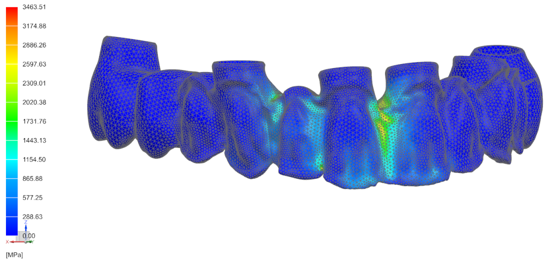

(b) Stress. Face view.

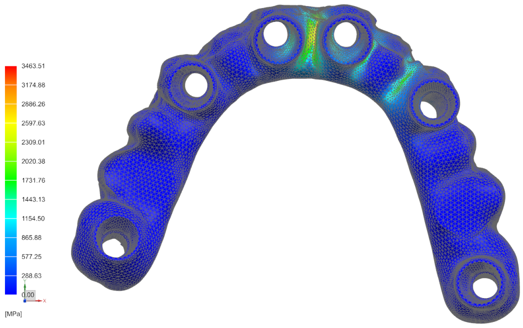

(c) Stress. Top view.

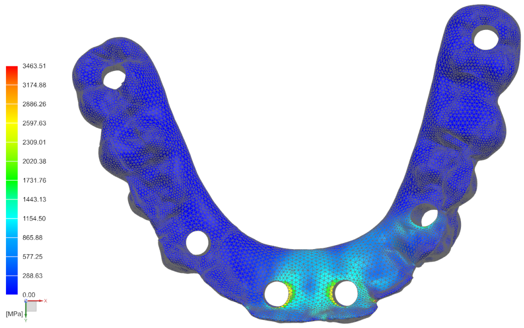

(d) Stress. Bottom view.

Figure A.34.: Displacement and stress caused by a 50 [μm] misfit in the normal direction applied on the third access hole of an All-on-6 prosthesis.

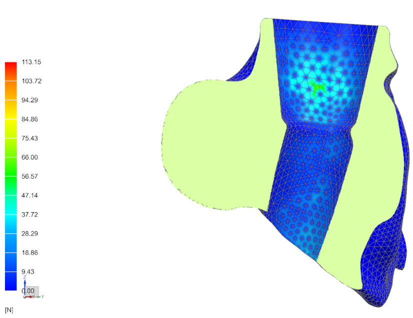

(a) Reaction forces on the second access hole.

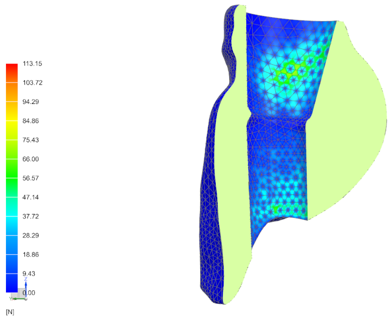

(b) Reaction forces on the third access hole.

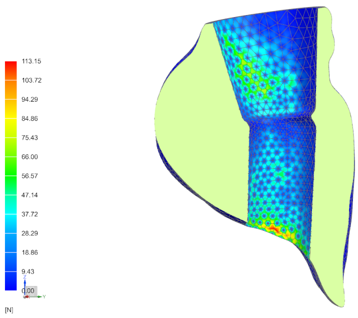

(c) Reaction forces on the third access hole.

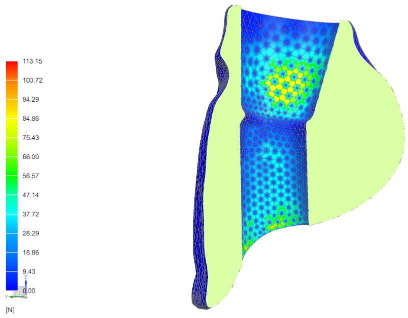

(d) Reaction forces on the fourth access hole.

Figure A.35.: Reaction forces for an All-on-6 prosthesis with a 50 [μm] misfit in the normal direction applied on the second access hole.

A.3. All-on-4

A.3.1. First Access Hole

Tangent

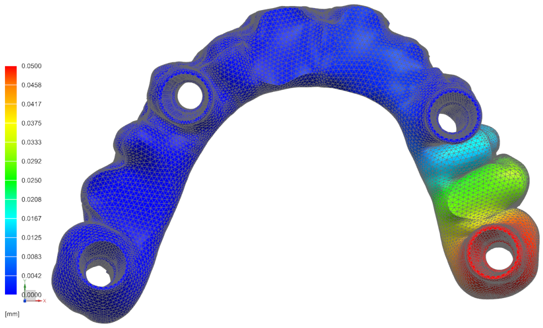

(a) Exaggerated displacement.

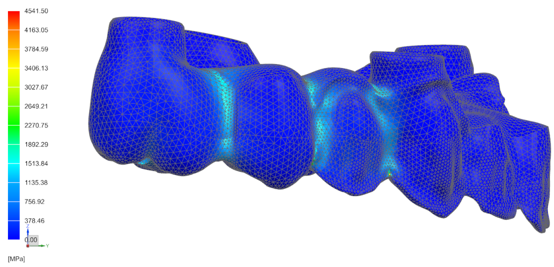

(b) Stress. Left view.

(c) Stress. Top view.

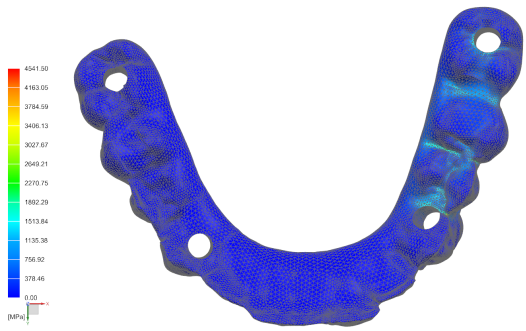

(d) Stress. Bottom view.

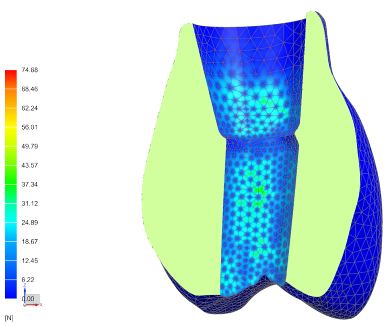

(e) Reaction forces. View inside the first access hole.

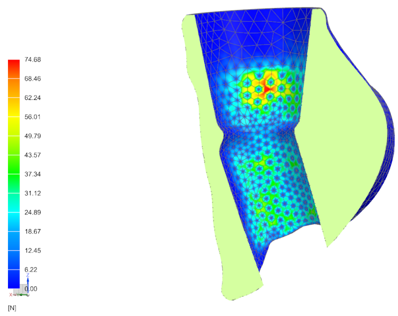

(f) Reaction forces. View inside the second access hole.

Figure A.36.: 50 [μm] misfit in the tangent direction applied on the first access hole of an All-on-4 prosthesis.

Binormal

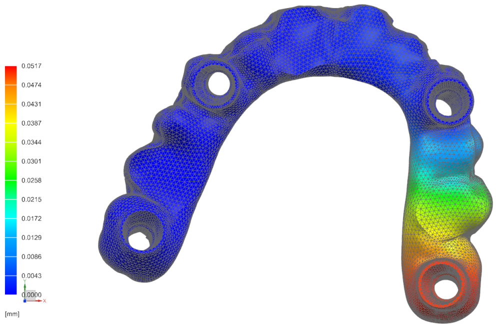

(a) Exaggerated displacement.

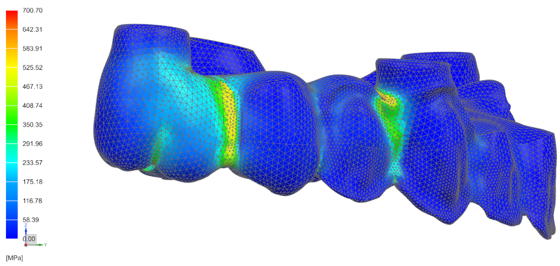

(b) Stress. Left view.

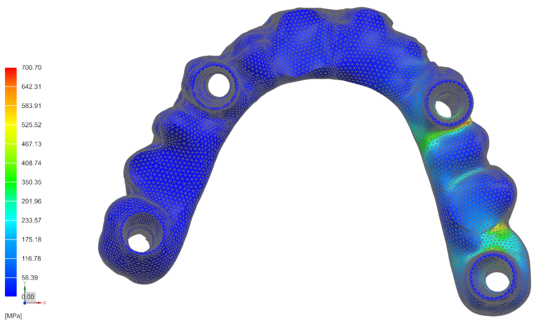

(c) Stress. Top view.

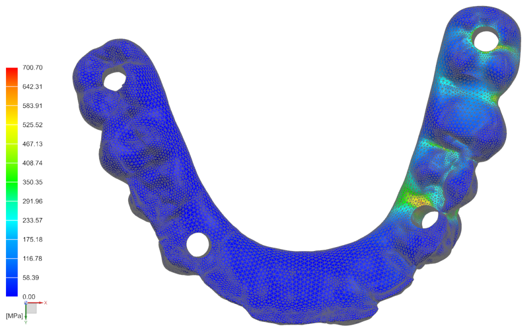

(d) Stress. Bottom view.

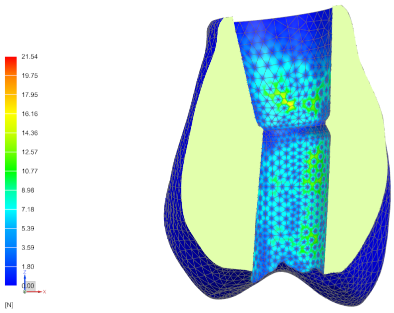

(e) Reaction forces. View inside the first access hole.

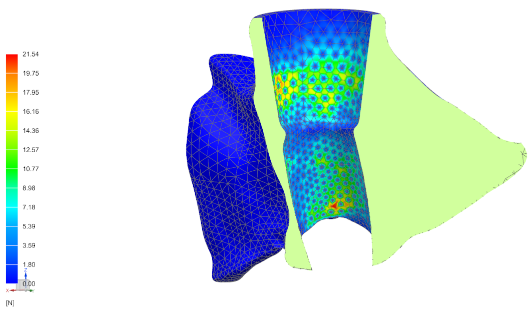

(f) Reaction forces. View inside the second access hole.

Figure A.37.: 50 [μm] misfit in the binormal direction applied on the first access hole of an All-on-4 prosthesis.

Normal

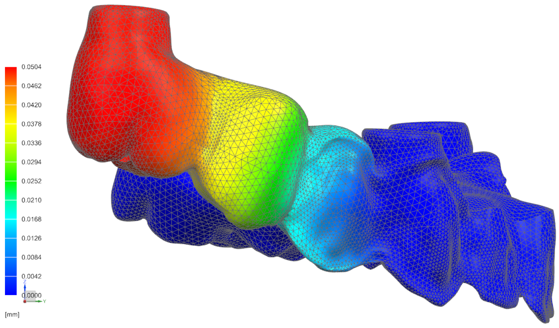

(a) Exaggerated displacement.

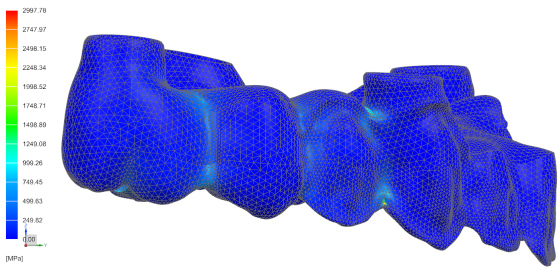

(b) Stress. Left view.

(c) Stress. Top view.

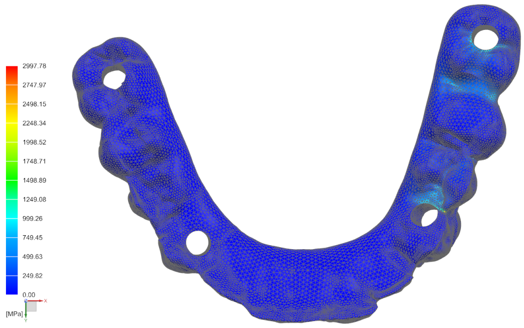

(d) Stress. Bottom view.

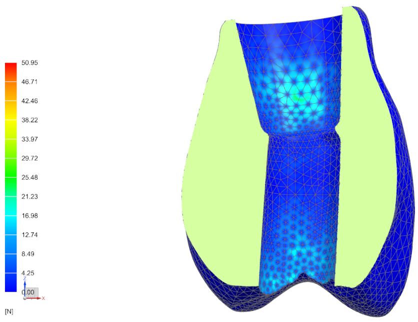

(e) Reaction forces. View inside the first access hole.

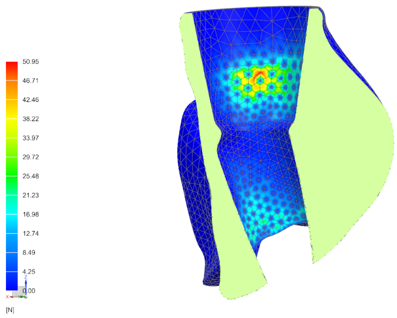

(f) Reaction forces. View inside the second access hole.

Figure A.38.: 50 [μm] misfit in the normal direction applied on the first access hole of an All-on-4 prosthesis.

A.3.2. Second Access Hole

Tangent

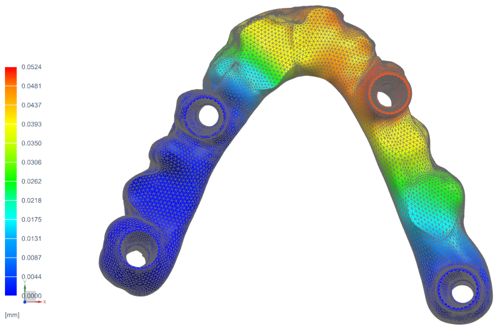

(a) Exaggerated displacement.

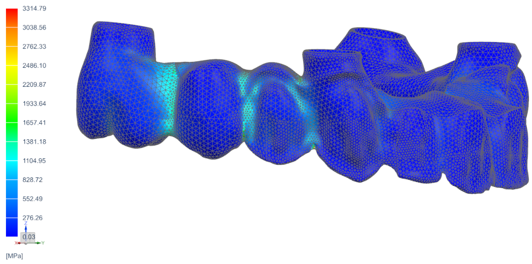

(b) Stress. Left view.

(c) Stress. Top view.

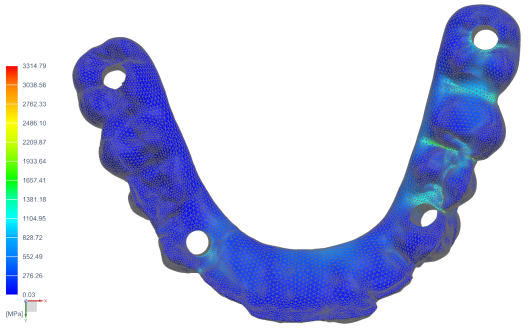

(d) Stress. Bottom view.

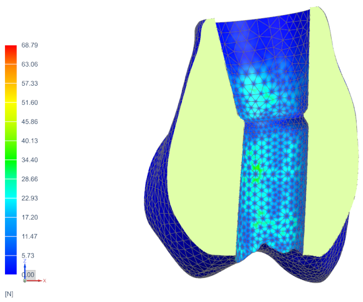

(e) Reaction forces. View inside the first access hole.

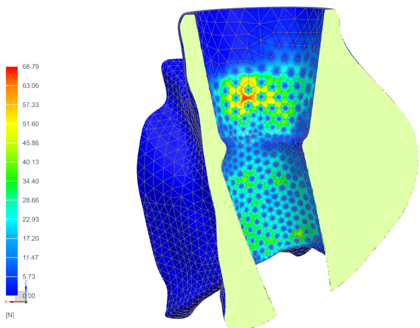

(f) Reaction forces. View inside the second access hole.

Figure A.39.: 50 [μm] misfit in the tangent direction applied on the second access hole of an All-on-4 prosthesis.

Binormal

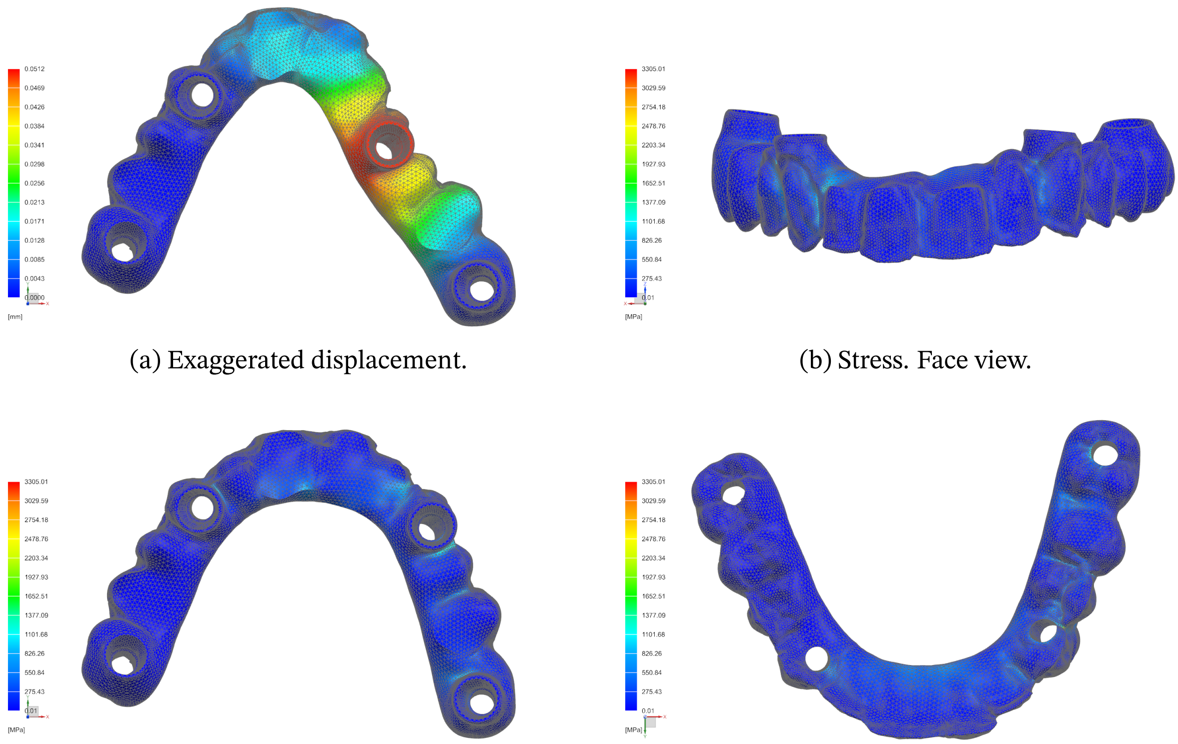

(a) Exaggerated displacement.

(b) Stress. Face view.

(c) Stress. Top view.

(d) Stress. Bottom view.

Figure A.40.: Displacement and stress caused by a 50 [μm] misfit in the binormal direction applied on the second access hole of an All-on-4 prosthesis.

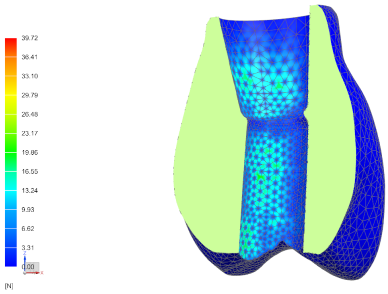

(a) Reaction forces on the first access hole.

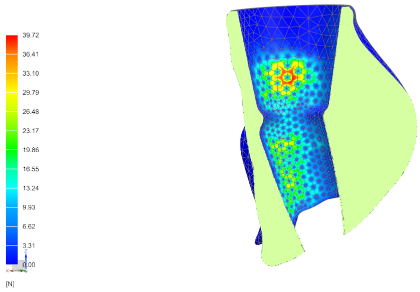

(b) Reaction forces on the second access hole.

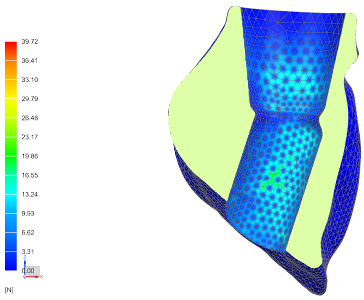

(c) Reaction forces on the second access hole.

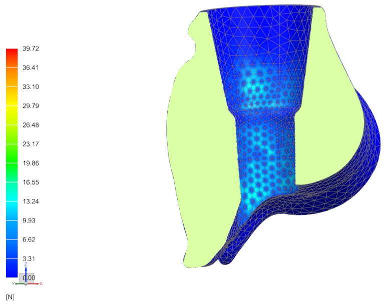

(d) Reaction forces on the third access hole.

Figure A.41.: Reaction forces for an All-on-4 prosthesis with a 50 [μm] misfit in the binormal direction applied on the second access hole.

Normal

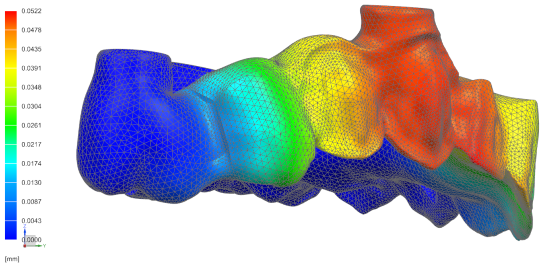

(a) Exaggerated displacement.

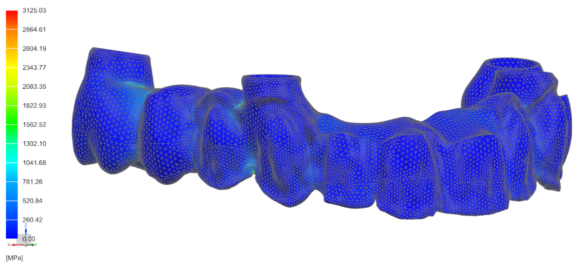

(b) Stress. Left view.

(c) Stress. Top view.

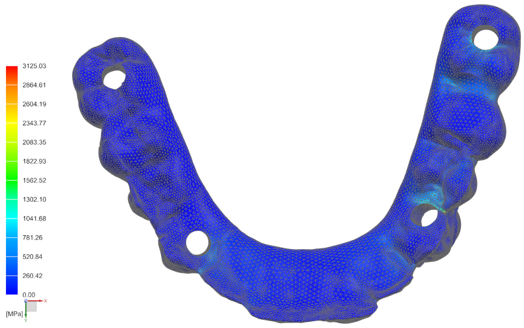

(d) Stress. Bottom view.

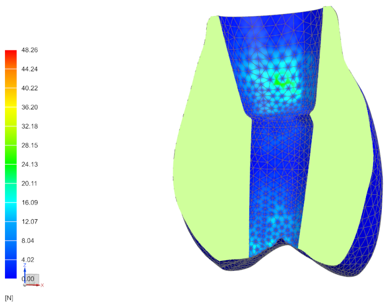

(e) Reaction forces. View inside the first access hole.

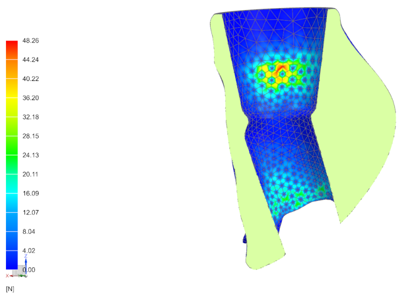

(f) Reaction forces. View inside the second access hole.

Figure A.42.: 50 [μm] misfit in the normal direction applied on the second access hole of an All-on-4 prosthesis.

Bibliography

[1] "Frontal sinus," May 2024.

[2] J. Katsoulis, T. Takeichi, A. Sol Gaviria, L. Peter, and K. Katsoulis, "Misfit of implant prostheses and its impact on clinical outcomes. Definition, assessment and a systematic review of the literature," *European Journal of Oral Implantology*, vol. 10 Suppl 1, pp. 121–138, 2017.

[3] T. Várady, R. R. Martin, and J. Cox, "Reverse engineering of geometric models—an introduction," *Computer-Aided Design*, vol. 29, pp. 255–268, Apr. 1997.

[4] "Continutity 1 : G0, G1, G2, G3."

[5] "Continuity of Curves and Surfaces."

[6] D. Lambade, "Implant Supported Mandibular Overdenture: A Viable Treatment Option for Edentulous Mandible," *Journal of Clinical and Diagnostic Research*, 2014.

[7] T. Flugge, W. J. van der Meer, B. G. Gonzalez, and others., "3Dcelo | Les techniques d'empreinte en implantologie."

[8] I. D. I. Sàrl, "Imetric iCam4D Photogrammetry System."

[9] A. Dayrell, C. Pimenta de Araújo, R. Rocha, C. Isolan, P. Noritomi, and M. Mesquita, "Biomechanics of internal connection in mandibular implant-supported prosthesis under effect of loadings and number of implants: A 3D finite element analysis," *Computers in Biology and Medicine*, vol. 148, Sept. 2022.

[10] R. Adell, U. Lekholm, B. Rockler, and P. I. Brånemark, "A 15-year study of osseointegrated implants in the treatment of the edentulous jaw," *International Journal of Oral Surgery*, vol. 10, pp. 387–416, Dec. 1981.

[11] P. I. Brånemark, B. Svensson, and D. van Steenberghe, "Ten-year survival rates of fixed prostheses on four or six implants ad modum Brånemark in full edentulism," *Clinical Oral Implants Research*, vol. 6, pp. 227–231, Dec. 1995.

[12] C. A. A. Lemos, F. R. Verri, E. A. Bonfante, J. F. Santiago Júnior, and E. P. Pellizzer, "Comparison of external and internal implant-abutment connections for implant supported prostheses. A systematic review and meta-analysis," *Journal of Dentistry*, vol. 70, pp. 14–22, Mar. 2018.

[13] R. Ghosh, S. Chanda, and D. Chakraborty, "The influence of macro-textural designs over implant surface on bone on-growth: A computational mechanobiology based study," *Computers in Biology and Medicine*, vol. 124, p. 103937, Sept. 2020.

[14] G. Heydecke, M. Zwahlen, A. Nicol, D. Nisand, M. Payer, F. Renouard, P. Grohmann, S. Mühlemann, and T. Joda, "What is the optimal number of implants for fixed reconstructions: a systematic review," *Clinical Oral Implants Research*, vol. 23 Suppl 6, pp. 217–228, Oct. 2012.

[15] M. Toia, M. Stocchero, Y. Jinno, A. Wennerberg, J. P. Becktor, R. Jimbo, and A. Halldin, "Effect of Misfit at Implant-Level Framework and Supporting Bone on Internal Connection Implants: Mechanical and Finite Element Analysis," *The International Journal of Oral & Maxillofacial Implants*, vol. 34, no. 2, pp. 320–328, 2019.

[16] T. Kapos and C. Evans, "CAD/CAM technology for implant abutments, crowns, and superstructures," *The International Journal of Oral & Maxillofacial Implants*, vol. 29 Suppl, pp. 117–136, 2014.

[17] J. Abduo and R. B. Judge, "Implications of implant framework misfit: a systematic review of biomechanical sequelae," in *Database of Abstracts of Reviews of Effects (DARE): Quality-assessed Reviews [Internet]*, Centre for Reviews and Dissemination (UK), 2014.

[18] T. Miyazaki, Y. Hotta, J. Kunii, S. Kuriyama, and Y. Tamaki, "A review of dental CAD/CAM: current status and future perspectives from 20 years of experience," *Dental Materials Journal*, vol. 28, pp. 44–56, Jan. 2009.

[19] T. Jemt and K. Book, "Prosthesis misfit and marginal bone loss in edentulous implant patients," *The International Journal of Oral & Maxillofacial Implants*, vol. 11, no. 5, pp. 620–625, 1996.

[20] A. Jokstad and B. Shokati, "New 3D technologies applied to assess the long-term clinical effects of misfit of the full jaw fixed prosthesis on dental implants," *Clinical Oral Implants Research*, vol. 26, pp. 1129–1134, Oct. 2015.

[21] O. Rauscher, "Impression-free implant restorations with Cerec InLab," *International Journal of Computerized Dentistry*, vol. 14, no. 2, pp. 139–146, 2011.

[22] F. Beuer, J. Groesser, J. Schweiger, J. Hey, J.-F. Güth, and M. Stimmelmayr, "The Digital One-Abutment/One-Time Concept. A Clinical Report," *Journal of Prosthodontics: Official Journal of the American College of Prosthodontists*, vol. 24, pp. 580–585, Oct. 2015.

[23] L. Hjalmarsson and J.-I. Smedberg, "A 3-year retrospective study of Cresco frameworks: preload and complications," *Clinical Implant Dentistry and Related Research*, vol. 7, no. 4, pp. 189–199, 2005.

[24] J. Katsoulis, R. Mericske-Stern, L. Rotkina, C. Zbären, N. Enkling, and M. B. Blatz, "Precision of fit of implant-supported screw-retained 10-unit computer-aided-designed and computer-aided-manufactured frameworks made from zirconium dioxide and titanium: an in vitro study," *Clinical Oral Implants Research*, vol. 25, pp. 165–174, Feb. 2014.

[25] M. Karl and T. D. Taylor, "Bone Adaptation Induced by Non-Passively Fitting Implant Superstructures: A Randomized Clinical Trial," *The International Journal of Oral & Maxillofacial Implants*, vol. 31, no. 2, pp. 369–375, 2016.

[26] E. A. Gomes, W. G. Assunção, L. F. Tabata, V. A. R. Barão, J. A. Delben, and E. A. C. de Sousa, "Effect of passive fit absence in the prosthesis/implant/retaining screw system: a two-dimensional finite element analysis," *The Journal of Craniofacial Surgery*, vol. 20, pp. 2000–2005, Nov. 2009.

[27] T. Ma, J. I. Nicholls, and J. E. Rubenstein, "Tolerance measurements of various implant components," *The International Journal of Oral & Maxillofacial Implants*, vol. 12, no. 3, pp. 371–375, 1997.

[28] T. Jemt and U. Lekholm, “Measurements of bone and frame-work deformations induced by misfit of implant superstructures. A pilot study in rabbits,” *Clinical Oral Implants Research*, vol. 9, pp. 272–280, Aug. 1998.

[29] B. Rangert, T. Jemt, and L. Jörneus, “Forces and moments on Branemark implants,” *The International Journal of Oral & Maxillofacial Implants*, vol. 4, no. 3, pp. 241–247, 1989.

[30] A. Lie and T. Jemt, “Photogrammetric measurements of implant positions. Description of a technique to determine the fit between implants and superstructures,” *Clinical Oral Implants Research*, vol. 5, pp. 30–36, Mar. 1994.

[31] P. P. Binon, “Evaluation of machining accuracy and consistency of selected implants, standard abutments, and laboratory analogs,” *The International Journal of Prosthodontics*, vol. 8, no. 2, pp. 162–178, 1995.

[32] T. Kallus and C. Bessing, “Loose gold screws frequently occur in full-arch fixed prostheses supported by osseointegrated implants after 5 years,” *The International Journal of Oral & Maxillofacial Implants*, vol. 9, no. 2, pp. 169–178, 1994.

[33] C. J. Goodacre, J. Y. Kan, and K. Rungcharassaeng, “Clinical complications of osseointegrated implants,” *The Journal of Prosthetic Dentistry*, vol. 81, pp. 537–552, May 1999.

[34] T. Jemt, U. Lekholm, and C. B. Johansson, “Bone response to implant-supported frameworks with differing degrees of misfit preload: in vivo study in rabbits,” *Clinical Implant Dentistry and Related Research*, vol. 2, no. 3, pp. 129–137, 2000.

[35] C. Kunavisarut, L. A. Lang, B. R. Stoner, and D. A. Felton, “Finite element analysis on dental implant-supported prostheses without passive fit,” *Journal of Prosthodontics: Official Journal of the American College of Prosthodontists*, vol. 11, no. 1, pp. 30–40, 2002.

[36] C. C. Mello, J. F. S. Junior, C. A. A. Lemos, G. A. Galhano, E. Evangelisti, R. Scotti, F. R. Verri, and E. P. Pellizzer, “Evaluation of the accuracy and stress distribution of 3-unit implant supported prostheses obtained by different manufacturing methods,” *Materials Science & Engineering. C, Materials for Biological Applications*, vol. 102, pp. 66–74, Sept. 2019.

[37] J. Abduo and K. Lyons, “Effect of vertical misfit on strain within screw-retained implant titanium and zirconia frameworks,” *Journal of Prosthodontic Research*, vol. 56, no. 2, pp. 102–109, 2012.

[38] M. S. Schwarz, “Mechanical complications of dental implants,” *Clinical Oral Implants Research*, vol. 11 Suppl 1, pp. 156–158, 2000.

[39] R. Skalak, “Biomechanical considerations in osseointegrated prostheses,” *The Journal of Prosthetic Dentistry*, vol. 49, pp. 843–848, June 1983.

[40] T. Jemt, J. E. Rubenstein, L. Carlsson, and B. R. Lang, “Measuring fit at the implant prosthodontic interface,” *The Journal of Prosthetic Dentistry*, vol. 75, pp. 314–325, Mar. 1996.

[41] K. B. Tan, J. E. Rubenstein, J. I. Nicholls, and R. A. Yuodelis, “Three-dimensional analysis of the casting accuracy of one-piece, osseointegrated implant-retained prostheses,” *The International Journal of Prosthodontics*, vol. 6, no. 4, pp. 346–363, 1993.

[42] T. Jemt and A. Lie, "Accuracy of implant-supported prostheses in the edentulous jaw: analysis of precision of fit between cast gold-alloy frameworks and master casts by means of a three-dimensional photogrammetric technique," *Clinical Oral Implants Research*, vol. 6, pp. 172–180, Sept. 1995.

[43] T. Jemt, "Three-dimensional distortion of gold alloy castings and welded titanium frameworks. Measurements of the precision of fit between completed implant prostheses and the master casts in routine edentulous situations," *Journal of Oral Rehabilitation*, vol. 22, pp. 557–564, Aug. 1995.

[44] H. M. Frost, "Perspectives: bone's mechanical usage windows," *Bone and Mineral*, vol. 19, pp. 257–271, Dec. 1992.

[45] H. M. Frost, "A 2003 update of bone physiology and Wolff's Law for clinicians," *The Angle Orthodontist*, vol. 74, pp. 3–15, Feb. 2004.

[46] A. Klinge, K. Becktor, C. Lindh, and J. P. Becktor, "Craniofacial height in relation to cross-sectional maxillary and mandibular morphology," *Progress in Orthodontics*, vol. 18, p. 32, Dec. 2017.

[47] D.-B. Alemayehu and Y.-R. Jeng, "Three-Dimensional Finite Element Investigation into Effects of Implant Thread Design and Loading Rate on Stress Distribution in Dental Implants and Anisotropic Bone," *Materials (Basel, Switzerland)*, vol. 14, p. 6974, Nov. 2021.

[48] A. Brune, M. Stiesch, M. Eisenburger, and A. Greuling, "The effect of different occlusal contact situations on peri-implant bone stress – A contact finite element analysis of indirect axial loading," *Materials Science and Engineering: C*, vol. 99, pp. 367–373, June 2019.

[49] O. Cantó-Navés, X. Marimon, M. Ferrer, and J. Cabratosa-Termes, "Comparison between experimental digital image processing and numerical methods for stress analysis in dental implants with different restorative materials," *Journal of the Mechanical Behavior of Biomedical Materials*, vol. 113, p. 104092, Jan. 2021.

[50] M. T. Borges Radaelli, H. T. Idogava, A. O. Spazzin, P. Y. Noritomi, and N. Boscato, "Parafunctional loading and occlusal device on stress distribution around implants: A 3D finite element analysis," *The Journal of Prosthetic Dentistry*, vol. 120, pp. 565–572, Oct. 2018.

[51] P. Marcián, J. Wolff, L. Horáčková, J. Kaiser, T. Zikmund, and L. Borák, "Micro finite element analysis of dental implants under different loading conditions," *Computers in Biology and Medicine*, vol. 96, pp. 157–165, May 2018.

[52] L.-j. Chen, H. He, Y.-m. Li, T. Li, X.-p. Guo, and R.-f. Wang, "Finite element analysis of stress at implant–bone interface of dental implants with different structures," *Transactions of Nonferrous Metals Society of China*, vol. 21, pp. 1602–1610, July 2011.

[53] I. Linetskiy, V. Demenko, L. Linetska, and O. Yefremov, "Impact of annual bone loss and different bone quality on dental implant success - A finite element study," *Computers in Biology and Medicine*, vol. 91, pp. 318–325, Dec. 2017.

[54] G. de la Rosa Castolo, S. V. Guevara Perez, P.-J. Arnoux, L. Badih, F. Bonnet, and M. Behr, "Implant-supported overdentures with different clinical configurations: Mechanical resistance using a numerical approach," *The Journal of Prosthetic Dentistry*, vol. 121, pp. 546.e1–546.e10, Mar. 2019.

[55] F. A. Hussein, K. N. Salloomi, B. Y. Abdulrahman, A. R. Al-Zahawi, and L. A. Sabri, "Effect of thread depth and implant shape on stress distribution in anterior and posterior regions of mandible bone: A finite element analysis," *Dental Research Journal*, vol. 16, no. 3, pp. 200–207, 2019.

[56] F. M. Dastenaei, A. Hajarian, O. Zargar, M. M. Zand, and S. Noorollahian, "Effects of thread shape on strength and stability of dental mini-screws against orthodontic forces," *Procedia Manufacturing*, vol. 35, pp. 1032–1038, Jan. 2019.

[57] A. Pozzi, P. Carosi, G. O. Gallucci, K. Nagy, A. Nardi, and L. Arcuri, "Accuracy of complete-arch digital implant impression with intraoral optical scanning and stereophotogrammetry: An in vivo prospective comparative study," *Clinical Oral Implants Research*, vol. 34, pp. 1106–1117, Oct. 2023.

[58] A. Schmidt, L. Klussmann, B. Wöstmann, and M. A. Schlenz, "Accuracy of Digital and Conventional Full-Arch Impressions in Patients: An Update," *Journal of Clinical Medicine*, vol. 9, p. 688, Mar. 2020.

[59] "What is Finite Element Analysis (FEA)? | Ansys."

[60] V. Bandela and S. Kanaparthi, "Finite Element Analysis and Its Applications in Dentistry," in *Finite Element Methods and Their Applications*, IntechOpen, Nov. 2020.

[61] J.-C. Bellefroid, "Reverse engineered modelling for structure stiffness analysis : application to automotive chassis," 2022.

[62] F. Buonamici, M. Carfagni, R. Furferi, L. Governi, A. Lapini, and Y. Volpe, "Reverse engineering of mechanical parts: A template-based approach," *Journal of Computational Design and Engineering*, vol. 5, pp. 145–159, Apr. 2018.

[63] N. Boutachdat, "Analyse par rétro-ingénierie de la modification d'un châssis de véhicule automobile," 2023.

[64] Siemens, "Siemens Documentation: Divide Facet Face."

[65] Siemens, "Siemens Documentation: Extract Geometry."

[66] Siemens, "Siemens Documentation: Deviation Gauge."

[67] J. Park and R. S. Lakes, *Biomaterials : An Introduction*. Springer Science and Business Media, 3rd ed., 2007.

[68] Siemens, "Simcenter 3D Pre/Post."

[69] J. Dias Corpa Tardelli, B. Monteiro de Barros Ciribelli Alves, M. Lima da Costa Valente, and A. Cândido dos Reis, "Influence of the modulus of elasticity of dental implants on the distribution of stresses in the alveolar bone by the finite element method: A systematic review," *Journal of Oral and Maxillofacial Surgery, Medicine, and Pathology*, vol. 35, pp. 383–389, Sept. 2023.

[70] Y. Gupta, R. Iyer, V. K. Dommeti, E. Nutu, M. Rana, A. Merdji, J. K. Biswas, and S. Roy, "Design of dental implant using design of experiment and topology optimization: A finite element analysis study," *Proceedings of the Institution of Mechanical Engineers, Part H: Journal of Engineering in Medicine*, vol. 235, pp. 157–166, Feb. 2021.

[71] R. Huang, L. Liu, B. Li, L. Qin, L. Huang, K. W. K. Yeung, and Y. Han, "Nanograins on Ti-25Nb-3Mo-2Sn-3Zr alloy facilitate fabricating biological surface through dual-ion implantation to concurrently modulate the osteogenic functions of mesenchymal stem cells and kill bacteria," *Journal of Materials Science & Technology*, vol. 73, pp. 31–44, May 2021.

[72] P. H. W. Tretto, M. B. F. d. Santos, A. O. Spazzin, G. K. R. Pereira, and A. Bacchi, "Assessment of stress/strain in dental implants and abutments of alternative materials compared to conventional titanium alloy—3D non-linear finite element analysis," *Computer Methods in Biomechanics and Biomedical Engineering*, June 2020.

[73] A. Robau-Porrua, Y. Pérez-Rodríguez, L. M. Soris-Rodríguez, O. Pérez-Acosta, and J. E. González, "The effect of diameter, length and elastic modulus of a dental implant on stress and strain levels in peri-implant bone: A 3D finite element analysis," *Bio-Medical Materials and Engineering*, vol. 30, pp. 541–558, Jan. 2020.

[74] J. Dias Corpa Tardelli, M. Lima da Costa Valente, T. Theodoro de Oliveira, and A. Cândido dos Reis, "Influence of chemical composition on cell viability on titanium surfaces: A systematic review," *The Journal of Prosthetic Dentistry*, vol. 125, pp. 421–425, Mar. 2021.

[75] J. Dias Corpa Tardelli, C. Bolfarini, and A. Cândido dos Reis, "Comparative analysis of corrosion resistance between beta titanium and Ti-6Al-4V alloys: A systematic review," *Journal of Trace Elements in Medicine and Biology*, vol. 62, p. 126618, Dec. 2020.

[76] B. Piotrowski, A. A. Baptista, E. Patoor, P. Bravetti, A. Eberhardt, and P. Laheurte, "Interaction of bone–dental implant with new ultra low modulus alloy using a numerical approach," *Materials Science and Engineering: C*, vol. 38, pp. 151–160, May 2014.

[77] J. Li, J. A. Jansen, X. F. Walboomers, and J. J. van den Beucken, "Mechanical aspects of dental implants and osseointegration: A narrative review," *Journal of the Mechanical Behavior of Biomedical Materials*, vol. 103, p. 103574, Mar. 2020.

[78] S. Sidhu, H. Singh, and M. A.-H. Gepreel, "A review on alloy design, biological response, and strengthening of beta-titanium alloys as biomaterials," *Materials Science and Engineering: C*, vol. 121, p. 111661, Feb. 2021.

[79] R. Batalha, W. Batalha, L. Deng, T. Gustmann, S. Pauly, C. S. Kiminami, and P. Gargarella, "Processing a biocompatible Ti–35Nb–7Zr–5Ta alloy by selective laser melting," *Journal of Materials Research*, vol. 35, pp. 1143–1153, May 2020.

[80] R. Batalha, V. Pinotti, O. O. S. Alnoaimy, W. Batalha, T. Gustmann, K. Kosiba, S. Pauly, C. Bolfarini, C. Kiminami, and P. Gargarella, "Microstructure and properties of TiB2-reinforced Ti–35Nb–7Zr–5Ta processed by laser-powder bed fusion," *Journal of Materials Research*, vol. 37, pp. 259–271, Jan. 2022.

[81] R. Batalha, S. Pauly, U. Kühn, K. Kosiba, C. Bolfarini, C. Kiminami, and P. Gargarella, "Oligocrystalline microstructure in an additively manufactured biocompatible Ti-Nb-Zr-Ta alloy," *Materials Letters*, vol. 262, p. 127149, Mar. 2020.

[82] P. Ausiello, J. Tribst, M. Ventre, E. Salvati, A. E. di Lauro, M. Martorelli, A. Lanzotti, and D. C. Watts, "The role of cortical zone level and prosthetic platform angle in dental implant mechanical response: A 3D finite element analysis," *Dental Materials*, vol. 37, pp. 1688–1697, Nov. 2021.

[83] S. H. Oh, I. K. Park, J. M. Kim, and J. H. Lee, "In vitro and in vivo characteristics of PCL scaffolds with pore size gradient fabricated by a centrifugation method," *Biomaterials*, vol. 28, pp. 1664–1671, Mar. 2007.

[84] S. Wu, X. Liu, K. W. K. Yeung, C. Liu, and X. Yang, "Biomimetic porous scaffolds for bone tissue engineering," *Materials Science and Engineering: R: Reports*, vol. 80, pp. 1–36, June 2014.

[85] D.-J. Yoo, "Advanced porous scaffold design using multi-void triply periodic minimal surface models with high surface area to volume ratios," *International Journal of Precision Engineering and Manufacturing*, vol. 15, pp. 1657–1666, Aug. 2014.

[86] M. da Costa Valente, T. de Oliveira, S. Kreve, R. Batalha, D. de Oliveira, S. Pauly, C. Bolfarini, L. Bachmann, and A. dos Reis, "Analysis of the mechanical and physicochemical properties of Ti-6Al-4 V discs obtained by selective laser melting and subtractive manufacturing method," *Journal of Biomedical Materials Research Part B: Applied Biomaterials*, vol. 109, no. 3, pp. 420–427, 2021.

[87] J. Fojt, M. Fousova, E. Jablonska, L. Joska, V. Hybasek, E. Pruchova, D. Vojtech, and T. Ruml, "Corrosion behaviour and cell interaction of Ti-6Al-4V alloy prepared by two techniques of 3D printing," *Materials Science and Engineering: C*, vol. 93, pp. 911–920, Dec. 2018.

[88] M. Dallago, V. Fontanari, E. Torresani, M. Leoni, C. Pederzolli, C. Potrich, and M. Benedetti, "Fatigue and biological properties of Ti-6Al-4V ELI cellular structures with variously arranged cubic cells made by selective laser melting," *Journal of the Mechanical Behavior of Biomedical Materials*, vol. 78, pp. 381–394, Feb. 2018.

[89] A. Lerebours, P. Vigneron, S. Bouvier, A. Rassineux, M. Bigerelle, and C. Egles, "Additive manufacturing process creates local surface roughness modifications leading to variation in cell adhesion on multifaceted TiAl6V4 samples," *Bioprinting*, vol. 16, p. e00054, Dec. 2019.

[90] Z. J. Wally, A. M. Haque, A. Feteira, F. Claeyssens, R. Goodall, and G. C. Reilly, "Selective laser melting processed Ti6Al4V lattices with graded porosities for dental applications," *Journal of the Mechanical Behavior of Biomedical Materials*, vol. 90, pp. 20–29, Feb. 2019.

[91] M. Wang, Y. Wu, S. Lu, T. Chen, Y. Zhao, H. Chen, and Z. Tang, "Fabrication and characterization of selective laser melting printed Ti–6Al–4V alloys subjected to heat treatment for customized implants design," *Progress in Natural Science: Materials International*, vol. 26, pp. 671–677, Dec. 2016.

[92] M. Shash, H. Nazha, and W. Abbas, "Influence of Different Abutment Designs on the Biomechanical Behavior of One-Piece Zirconia Dental Implants and Their Surrounding Bone: A 3D-FEA," *IRBM*, vol. 40, pp. 313–319, Dec. 2019.

[93] M. R. Rieger, W. K. Adams, G. L. Kinzel, and M. O. Brose, "Alternative materials for three endosseous implants," *The Journal of Prosthetic Dentistry*, vol. 61, pp. 717–722, June 1989.

[94] H. Hedia and N.-A. Mahmoud, "Design optimization of functionally graded dental implant," *Bio-Medical Materials and Engineering*, vol. 14, no. 2, pp. 133–143, 2004.

[95] A. Sadollah and A. Bahreininejad, "Optimum gradient material for a functionally graded dental implant using metaheuristic algorithms," *Journal of the Mechanical Behavior of Biomedical Materials*, vol. 4, pp. 1384–1395, Oct. 2011.

[96] H. Kondo, A. Yokoyama, M. Omori, A. Ohkubo, T. Hirai, F. Watari, M. Uo, and T. Kawasaki, "Fabrication of Titanium Nitride/Apatite Functionally Graded Implants by Spark Plasma Sintering."

[97] D. Lin, Q. Li, W. Li, S. Zhou, and M. V. Swain, "Design optimization of functionally graded dental implant for bone remodeling," *Composites Part B: Engineering*, vol. 40, pp. 668–675, Oct. 2009.

[98] T. Traini, C. Mangano, R. L. Sammons, F. Mangano, A. Macchi, and A. Piattelli, "Direct laser metal sintering as a new approach to fabrication of an isoelastic functionally graded material for manufacture of porous titanium dental implants," *Dental Materials*, vol. 24, pp. 1525–1533, Nov. 2008.